NTNU
Norwegian University of
Science and Technology

Preparation of $(La_{0.8}Sr_{0.2})_{0.995}CoO_3$-based Inks for Ink-Jet Printing of Thin Films in Solid Oxide Fuel Cells (SOFCs)

Daniel Tevik Rogstad

Chemical Engineering and Biotechnology
Submission date: July 2017
Supervisor: Hilde Lea Lein, IMA
Co-supervisor: Sophie Labonnote-Weber, CerPoTech AS

Norwegian University of Science and Technology
Department of Materials Science and Engineering

Preface

The work resulting in this Master's thesis has been conducted at the Norwegian University of Science and Technology (NTNU) as part of the Master's degree program *Chemical Engineering and Biotechnology,* with a specialisation in *Materials for Energy Technology.* The author performed the work at the Department of Materials Science and Engineering within the Inorganic Materials and Ceramics Research Group during the spring semester of 2017. Associate Professor Hilde Lea Lein supervised the work along with co-supervisor Sophie Labonnote-Weber. The project was carried out in cooperation with CerPoTech AS, which produced the ceramic powder that the research was conducted on. CerPoTech AS produces several advanced ceramic oxide powders and through this project they would like to investigate the possibility of using their powders to make stable ceramic suspensions for use in ink-jet printing. This thesis is a continuation of the specialisation project *«Preparation of $(La_{0,8}Sr_{0,2})_{0,995}CoO_3$-based inks for ink-jet printing of thin films in Solid Oxide Fuel Cells (SOFCs)»*, submitted by the author December 2016 [1]. The ceramic powder that was used in this work is from the same batch as that used in the specialisation project and the properties found through characterisation done in that work may be used, and referenced.

<div align="center">

Trondheim, 06-07-2017

Daniel Tevik Rogstad

</div>

Acknowledgements

I would like to thank my supervisor, Associate Professor Hilde Lea Lein at the Norwegian University of Science and Technology, and co-supervisor Dr. Sophie Labonnote-Weber at CerPoTech AS for their help and constructive feedback throughout the semester. I would also like to thank my fellow members of the Research Group on Batteries, Surfaces and Composites for their feedback on my presentations. My grateful thanks are also extended to the technical staff at the Department of Materials Science and Engineering for necessary equipment training. A big thanks is directed to my family for trying to understand what I have been doing this past year and supporting me nonetheless. Finally, I would like to thank my girlfriend, who has supported me well through all this work and has put up with the long periods of physical (and at times mental) absence caused by it.

D.T.R.

Abstract

Lanthanum Strontium Cobalt oxide (LSC) is a mixed ionic-electronic conductor (MIEC) ceramic suited for use as cathode material in Solid Oxide Fuel Cells (SOFCs). Extensive research is conducted on producing the cathode in the SOFC as a thin film to reduce operating temperatures and alleviate disadvantageous properties like high thermal expansion coefficient (TEC). One way of producing thin films is through ink-jet printing. Ink-jet printing is a cheap, simple and precise manufacturing method that produces less waste than other deposition methods. It is therefore of interest to explore the feasibility of producing LSC thin films this way. This thesis investigates the possibility of making a stable ceramic ink based on LSC. An LSC powder with the stoichiometry $(La_{0,8}Sr_{0,2})_{0,995}CoO_3$ was used, produced by CerPoTech AS through spray pyrolysis. The powder was suspended in ten different liquid systems, five based on α-Terpineol, Isopropanol and Polyvinylpyrrolidone and five based on Ethylene Glycol, Distilled Water and Dolapix CE 64. All inks were characterised to find their particle size distribution, density, viscosity and surface tension. Particle size distribution data gathered over two days were used to evaluate the stability of the inks. The fluid properties were used to evaluate the jettability of the inks by means of the Z-parameter (Ohnesorge reciprocal), the Ca–We parameter space defined by Nallan et al. [2], and the We–Re parameter space as defined by Derby [3, 4, 5, 6].

Five out of the ten inks were printed onto paper as black squares of different transparency in 1, 2, 3, 4, 5 and 10 layers using an Epson WorkForce® WF-2630 commercial office printer with piezoelectric drop on demand (DOD) ink-jet technology. The one- and ten-layered squares were examined using optical and scanning electron microscopy.

The α-Terpineol based suspensions showed good stability against agglomeration and sedimentation over a two day period and an accurate deposition of a locally coherent film of LSC-powder was achieved through printing of a 50 wt% isopropanol suspension with a solid content of 19.3 wt%.

Sammendrag

Lantan-Strontium-Koboltoksid (LSC) er en kombinert ionisk-elektronisk leder (MIEC), og egner seg som keramisk forbindelse til bruk som katodemateriale i faststoff brenselceller (SOFCs). Det utføres omfattende forskning som går ut på å produsere katoden i en faststoff brenselcelle som en tynnfilm for å redusere driftstemperaturen og for å minimere effecten av ugunstige egenskaper som høy termisk ekspansjonskoeffisient (TEC). En måte å produsere tynnfilmer på er gjennom blekkprinting. Blekkprinting er en billig, enkel og presis produksjonsmetode som fører til mindre overforbruk av råmateriale enn andre metoder. Det er derfor av interesse å utforske muligheten for å produsere tynnfilmer av LSC på denne måten. Denne masteroppgaven undersøker muligheten for å lage stabile keramiske blekk basert på LSC. Et LSC-pulver med støkiometrien $(La_{0,8}Sr_{0,2})_{0,995}CoO_3$ ble brukt. Pulveret ble produsert av CerPoTech AS gjennom spraypyrolyse. Pulveret ble dispergert i ti ulike fluidsystemer, fem basert på blandinger av α-Terpinol, isopropanol og polyvinylpyrrolidon og fem basert på blandinger av etylenglykol, destillert vann og Dolapix CE 64. Alle de tillagede blekkene ble karakterisert for å finne partikkelstørrelsesdistribusjonen, tettheten, viskositeten og overflatespenningen deres. Partikkelstørrelsesdistribusjonen ble målt over to dager for å kunne evaluere stabiliteten til blekkene. Fluidegenskapene ble brukt til å evaluere printbarheten til blekkene gjennom Z-parameteren (resiprokt tall til *Oh*-tallet), Kapillær-Weber-parameterrommet definert av Nallan et al. [2], samt Weber-Reynolds-parameterrommet definert av Derby [3, 4, 5, 6].

Fem av de ti blekkene ble skrevet ut på papir i form av sorte firkanter med ulik gjennomsiktighet i ett, to, tre, fire, fem og ti lag ved bruk av en Epson WorkForce® WF-2630, en kommersiell kontorskriver med piezoelektrisk dråpe-ved-etterspørsel (DOD) teknologi. De énlags og tilags utskrevede firkantene ble undersøkt ved hjelp av både optisk- og sveipelektronmikroskopi.

De α-Terpinolbaserte suspensjonene viste god stabilitet mot agglomerering og sedimentering over en todagsperiode og en presis avsetning av en lokalt sammenhengende film av LSC-pulver ble oppnådd ved printing av en suspensjon med 50 vektprosent isopropanol og en faststoffmengde på 19.3 vektprosent.

Contents

List of Figures

List of Tables

Acronyms and nomenclature

Acronyms

AIP	α-Terpineol, Isopropanol and PVP based suspension
BET	Brunauer-Emmett-Teller, theory for physical gas adsorption
CIJ	Continuous Ink-Jet printing
DLVO	Theory of electrostatic stability of colloids named after B.Derjaguin, L. D. Landau, E. J. W. Verwey and J. Th. G. Overbeek
DOD	Drop On Demand
EDL	Electrical Double Layer
EWD	Ethylene glycol, distilled Water and Dolapix CE 64 based suspension
HT-SOFC	High Temperature Solid Oxide Fuel Cell
IT-SOFC	Intermediate Temperature Solid Oxide Fuel Cell
LHV	Lower Heating Value
LSC	$(La_{0,8}Sr_{0,2})_{0,995}CoO_3$
MIEC	Mixed Ionic-Electronic Conductor
PSD	Particle Size Distribution
PVP	Polyvinylpyrrolidone
SEM	Scanning Electron Microscopy
SOFC	Solid Oxide Fuel Cell
TEC	Thermal Expansion Coefficient
TPB	Triple Phase Boundary
XRD	X-Ray Diffraction
YSZ	Yttria-Stabilised Zirconia

Nomenclature

τ	Shear stress in viscosity measurements
η	Coefficient of viscosity
$\dot{\gamma}$	Shear rate in viscosity measurements
J	Diffusion flux in *Fick's first law*
D	Diffusion coefficient in *Fick's first law*
ζ	Zeta potential
Oh	Ohnesorge number
Z	Z parameter, the inverse of the Ohnesorge number
d_{Oh}	Characteristic length (nozzle diameter) in the formula of the Ohnesorge number
β	Bond number, a dimensionless quantity describing the shape of a pendant drop
Ca	Capillary number, a dimensionless quantity relating the viscous force and surface tension across a liquid-gas or liquid-liquid interface
We	Weber number, a dimensionless quantity relating a fluid's inertia and surface tension
Re	Reynolds number, a dimensionless quantity relating a fluid's inertial and viscous forces
$\bar{d}_s$	Surface average diameter of a spherical particle
ρ	The density of a given material or system
σ	Surface tension
ρ_d	Density of the drop phase in pendant drop tensiometry
ρ_c	Density of the continuous phase in pendant drop tensiometry
$\mathbf{D}_{n,10}$	Limit where 10% of the particles are smaller in size
$\mathbf{D}_{n,50}$	Limit where 50% of the particles are smaller in size
$\mathbf{D}_{n,90}$	Limit where 90% of the particles are smaller in size
d_{XRD}	Crystallite size calculated from the tallest single peak of an X-ray diffractogram
$\bar{d}_n$	Number based average particle size

Chapter 1

Background

1.1 Motivation

The world is experiencing a steady increase in power demand and at the same time environmental changes due to our current way of power generation. As the negative impacts of our continued use of and dependence on fossil fuels become increasingly evident, the world is looking for alternative ways of generating the energy that we so very much do and will continue to depend on.

A transition towards more efficient devices that can run on renewable energy sources is part of this unavoidable journey. The Solid Oxide Fuel Cell is such a device, capable of directly converting chemical energy from a range of fuels into electrical energy and achieve a higher energy-conversion efficiency than the existing, Carnot cycle limited, thermal power generation systems. Multi stage SOFC systems with regeneration of exhaust gases have recently reached a power generation efficiency as high as 77.8% (DC, LHV)[7].

There is a desire to lower the operational temperature of SOFCs and there are several reasons for this, some of which are: avoiding problems with long-term stability, increasing reliability, lowering cost of materials and operation, increasing portability, and increasing the efficiency of the cell further. As an example, the theoretical efficiency of a CO-fueled Solid Oxide Fuel Cell increases from 63% at 900 °C to 81% at 350 °C [8].

A way of lowering the temperature is by making the components of the SOFC thinner, to lower the bulk resistance and transport distances of the charge carriers. Effective ways

of manufacturing the thin film components are needed. Traditional ways like sputtering and vapour deposition techniques have long been used to deposit films thinner than a few microns, but the scalability of the techniques remains an issue [8].

Ink-jet printing is a proposed solution to this problem. Along with scalability it brings with it advantages like low material wastage, high precision and the fact that the technology is cheap and easy to operate. However, to be able to use ink-jet technology for the production of Solid Oxide Fuel Cell components, suspensions ("inks") of the component material have to be made. These suspensions must fulfil certain demands when it comes to particle size, stability, and jettability.

1.2   Aim of the work

The aim of this study is to find a combination of liquid media and stabilisers that will keep a $(La_{0,8}Sr_{0,2})_{0,995}CoO_3$-powder dispersed and stable in suspension. That is, the suspension should not be prone to agglomeration and sedimentation of the solid particles. The suspension is intended to be used with ink-jet technology to produce thin film cathodes for Solid Oxide Fuel Cells and must therefore also fulfil certain criteria when it comes to particle size and properties related to its jettability. The former is examined with laser diffraction measurements while the latter will be evaluated through the use of the Ohnesorge number via its reciprocal, Z, as well as two experimentally determined criteria for jettability found in the literature. Printing tests of the suspensions will be performed to validate or question these criteria and evaluate the practical performance of the suspensions as inks for use with ink-jet technology.

Chapter 2

Introduction

2.1 Solid Oxide Fuel Cells

2.1.1 Working principles

The Solid Oxide Fuel Cell is a solid state device that converts chemically bound energy into electrical energy (and heat) through electrochemically combining fuel and oxidant gases across an electrolyte (oxide) that is ionically conducting [9]. The main feature of a fuel cell is its high energy conversion efficiency. Contrary to the combustion-driven devices, a SOFC converts chemical energy directly to electrical energy without the intermediate thermal energy step, and this means that the SOFC conversion efficiency is not limited by the Carnot cycle [9]. Figure 2.1 shows a schematic diagram of how a Solid Oxide Fuel Cell operates. Fuel is fed to the anode, an oxidant is fed to the cathode, and through the electrochemical reactions happening inside the cell, direct current, exhaust gases and heat are produced.
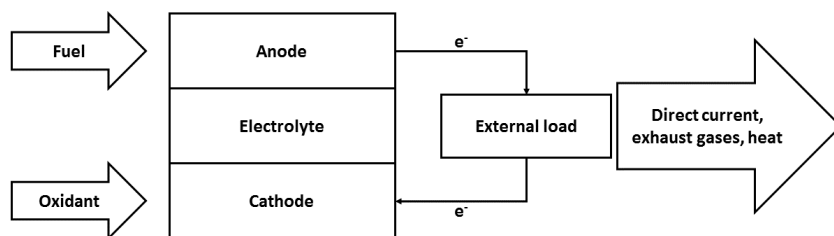
Figure 2.1: Schematic diagram of fuel cell operation. Redrawn from Minh [9].

In the simple case were the fuel is pure hydrogen and the oxidant is oxygen from the air, the following electrochemical reactions occur at the electrodes:

At the cathode, oxygen from the air is reduced,

$$\frac{1}{2}\,O_2(g) + 2\,e^- \longrightarrow O^{2-} \tag{2.1}$$
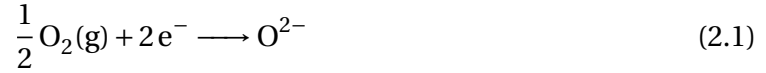
the oxygen ions travel through the solid electrolyte and reduces the hydrogen to form water and release electrons.

$$H_2(g) + O^{2-} \longrightarrow H_2O + 2\,e^- \tag{2.2}$$

The electrons are transferred from the anode to the cathode by an outer circuit, and can be used to do work by connecting an external load, as shown in Figure 2.1.

2.1.2 Fuel cell design

Solid Oxide Fuel Cells have many advantages over other types of fuel cells, from the use of non-precious materials (platinum is used as a catalyst e.g. in Proton Exchange Membrane (PEM) Fuel Cells [10]) to the invariant electrolyte and a structure with no liquid phases. The fact that all components are solid means means that it is possible to fabricate them in very thin layers and configure them into unique shapes that would not be possible with liquid parts [9]. Figure 2.2 shows two different types of SOFC design.

(a) Planar SOFC   **(b)** Tubular SOFC
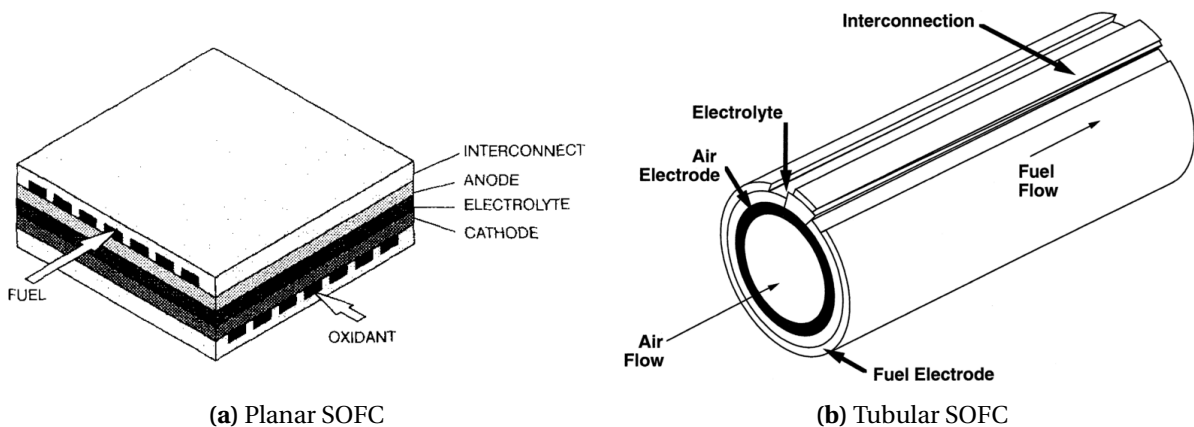
Figure 2.2: Schematics of Solid Oxide Fuel Cell designs. (a) Planar, from Minh [9], (b) Tubular, from Singhal [11].

The principle components are, as shown, the electrolyte, the anode, the cathode and the interconnect. Each component is required to have proper stability (chemical, phase, morphological and dimensional) in oxidising and/or reducing environments, good conductivity and chemical compatibility with the other components. In addition, for SOFCs, it is important that the components have a similar coefficient of expansion to avoid delamination or cracking during fabrication and operation [9]. The electrolyte and interconnect must be dense to prevent gas mixing, while the anode and cathode should be porous so that gas can be transported to the reaction sites, the triple phase boundaries (TPB), where electronic and ionic conducting phases co-exist [12]. Figure 2.3 (a) displays the cross-section of a SOFC, showing the dense electrolyte and porous electrodes, and (b) shows the two different triple phase boundaries at the anode.
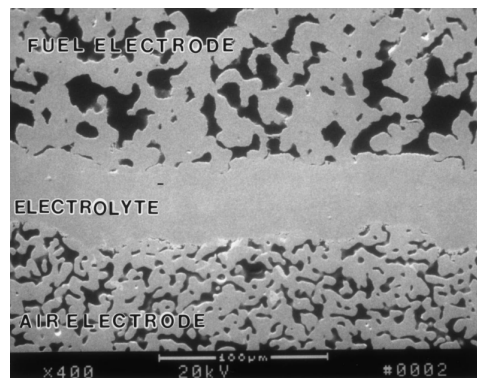
(a) Cross section of a SOFC
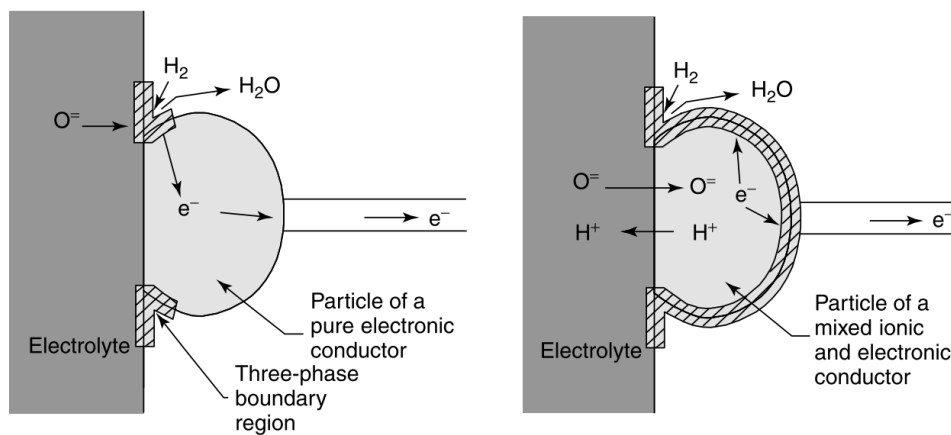
(b) Triple phase boundaries

Figure 2.3: (a) SEM micrograph of a cross section of a Siemens Westinghouse Solid Oxide Fuel Cell. From Singhal [11]. (b) Slightly exaggerated triple phase boundary for a pure electronic conductor (left) and a mixed ionic and electronic conductor (right) in the case of an anode, similar for a cathode. From Larminie [13].

Solid Oxide Fuel Cells are often divided into groups depending on the temperature at which they operate. SOFCs that operate in the temperature region between 850-1000 °C are called High Temperature Solid Oxide Fuel Cells (HT-SOFC) [12], and those that operate between 500-750 °C are called Intermediate Temperature Solid Oxide Fuel Cells (IT-SOFC) [10]. A comparison between the two is presented in Table 2.1.

Table 2.1: Advantages and disadvantages of HT-SOFCs and IT-SOFCs
Reprinted from Høyem [14]

Cell type	Advantages and Disadvantages
HT-SOFC	+ No external reformer needed. + High conductivities in already established materials. + Compatible materials with matching thermal coefficients exist. + Faster reaction kinetics. + Lower ohmic resistances. - Material degradation. - Issues regarding stability of the cell. - Longer start-up time.
IT-SOFC	+ Reduced system cost. + Expands choice of materials. + Reduced corrosion rates. + Possibilities to use metal interconnects for increased conductivity. + More rapid start-up and shut-down. + Improved durability. + Unlocks wider range of potential applications. + Less dependent on matching thermal expansion coefficient. - Lower conductivity. - Deactivation of catalysts. - External fuel processor needed to use hydrocarbons as fuel.

Even lower operating temperatures can be reached by making the components as thin films, with a thickness in the range of a couple of microns [15]. An exiting area of research is using Mixed Ionic-Electronic Conductors (MIECs) as electrodes. These can be made both as porous "thick" (>10 µm) and dense thin (<5 µm) films, or even as double layered porous/dense or dense/porous films (Endo, Wada, Wen, Komiyama & Yamada (1998) as cited in [15]).

2.1.3 Material selection in fuel cells

Table 2.2 presents a range of different materials used in IT-SOFCs from different developers.

Table 2.2: A summary of different IT-SOFCs materials from different developers
Modified from [12]

Developer	Temperature [°C]	Anode	Electrolyte	Cathode	Interconnect
Ceres Power	500-650	CGO	Ni-CGO	LSCF-CGO	Ferritic steel
CFCL	750	YSZ	Ni-YSZ	LSM	Coated ferritic steel
Delphi	750	YSZ	Ni-YSZ	LSCF	Coated ferritic steel
Mitsubishi materials	600-800	LSGMC	Ni-SDC	SSC	*
Topsoe Fuel cells	750-850	YSZ	Ni-YSZ	Ni-LSM	Coated ferritic steel
Versa power	750	YSZ	Ni-YSZ	LSM-YSZ	Uncoated ferritic steel

*Unknown, YSZ-yttria stabilised zirconia; LSM-strontium doped lanthanum manganite;
LSCF-strontium cobalt doped lanthanum ferrite; LSGMC-lanthanum gallate;
SSC-samaria strontium cobalt oxide; SDC-samaria doped ceria

LSC as a cathode material

$La_{1-x}Sr_xCoO_{3-\delta}$ with different compositions (x) have received extensive research as a cathode material in SOFCs [16, 17, 18, 19, 20]. This applies mostly to intermediate temperature ranges as LSC has some reactivity problems with YSZ, a very common fuel cell electrolyte, as well as a large mismatch in thermal expansion coefficient ($TEC_{LSC} = 23\,\text{ppmK}^{-1}; TEC_{YSZ} = 11\,\text{ppmK}^{-1}$)[16]. A proposed solution to this problem is to implement LSC as a porous thin film, and this has shown promising results in intermediate temperature ranges ($T < 700\,°C$)[17, 19, 20].

The reason for the large interest in the perovskite structured LSC as a cathode material is that it has high oxidation catalytic activity and excellent oxygen electrode performance. This is due to high oxygen diffusivity and high dissociation ability of oxygen molecules. The cobalt increases the ionic and electronic conductivity of the material (LSC is a Mixed Ionic-Electronic Conductor (MIEC)) and leads to a decrease in the cathode polarisation resistance [18].

2.2 Ink-jet printing

Ink-jet printing as a concept can be traced all the way back to William Thompson (later Lord Kelvin) who in 1867 was granted a patent for his proposal to

> 'use electrostatic forces to control the release of ink onto paper.'[21]

It was not before 1951 that Siemens produced their first commercial "continuous" ink-jet (CIJ) printer, and the technology for "Drop-on-Demand" (DOD) printing was invented in 1973. The first DOD-printers used heating elements to eject ink, they were therefore called "thermal" ink-jets. Piezoelectric printing technology entered the marked in 1993 in an Epson printer and the year after both Canon, Epson and HP introduced colour ink-jets to the market [21]. Today, advanced yet easy to operate ink-jet printers are available for almost everyone at affordable prices.

2.2.1 Classifications

As mentioned in the paragraph above, several different technologies exist within the field of ink-jet printing. They will be further described below.

Continuous ink-jet printing

In CIJ printing, a stream of drops is produced through the Rayleigh instability of a liquid column that is ejected through a small nozzle under high pressure. The drops are directed through imparting a small charge on them from the nozzle, which is held at a potential relative to ground. The individual drops are controlled by applying a potential to deflector plates [4]. A schematic diagram of the working principles is shown in Figure 2.4.
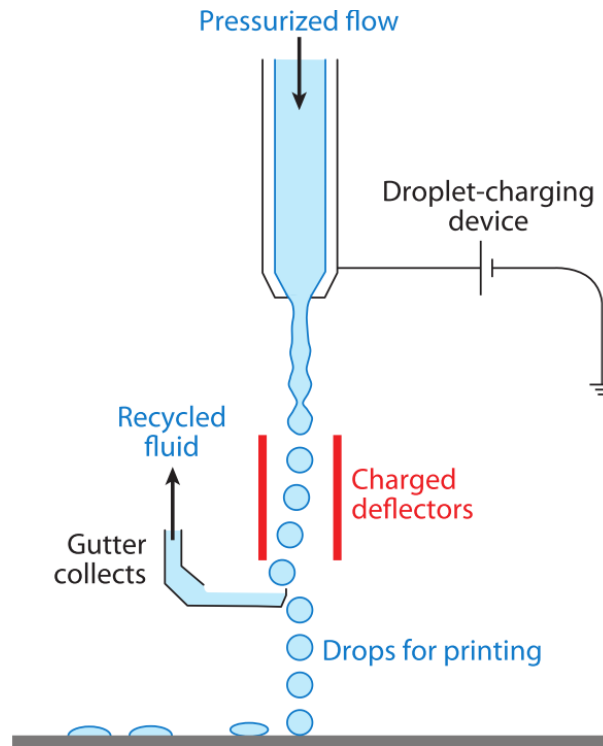
Figure 2.4: Schematic illustration of the working principles of a continuous ink-jet (CIJ) printer. From Derby [4].

The drops that are produced are generally a bit larger than the nozzle diameter, and can range from 10-150 µm, but are typically ~100 µm in diameter. Since the drop formation is continuous, unwanted drops must be deflected into a gutter to create blank spaces in a pattern. This leads to a quite substantial amount of ink not being used. In most CIJ applications, like product marking and graphics, the unused ink can be recycled. For applications in materials science, the possible contamination risk involved with the recycling makes CIJ printing technology unfavourable, or in the case of no recycling; wasteful [4].

DOD ink-jet printing

In DOD printing, individual drops are generated, and it is therefore a more economical technology than CIJ-printing and without the contamination risks. It is thus the favoured technology within the field of materials science. The generated drops are generally approximately equal to the nozzle size but can, along with the ejection speed, be controlled through variations in the pressure pulse used to eject the drop. DOD printing is dominant in graphics and text printing that require high precision printing, with typical drop diame-

ters of 20-50 μm [4].

Since the drops are generated individually, drop placement can be accomplished with high precision, placing the nozzle above the desired location and creating a pressure pulse within the chamber behind the nozzle to eject a drop. There are two methods that are used to generate this pressure pulse, thermal and piezoelectric. The operating principles of both are illustrated in Figure 2.5 (a) and (b), respectively.
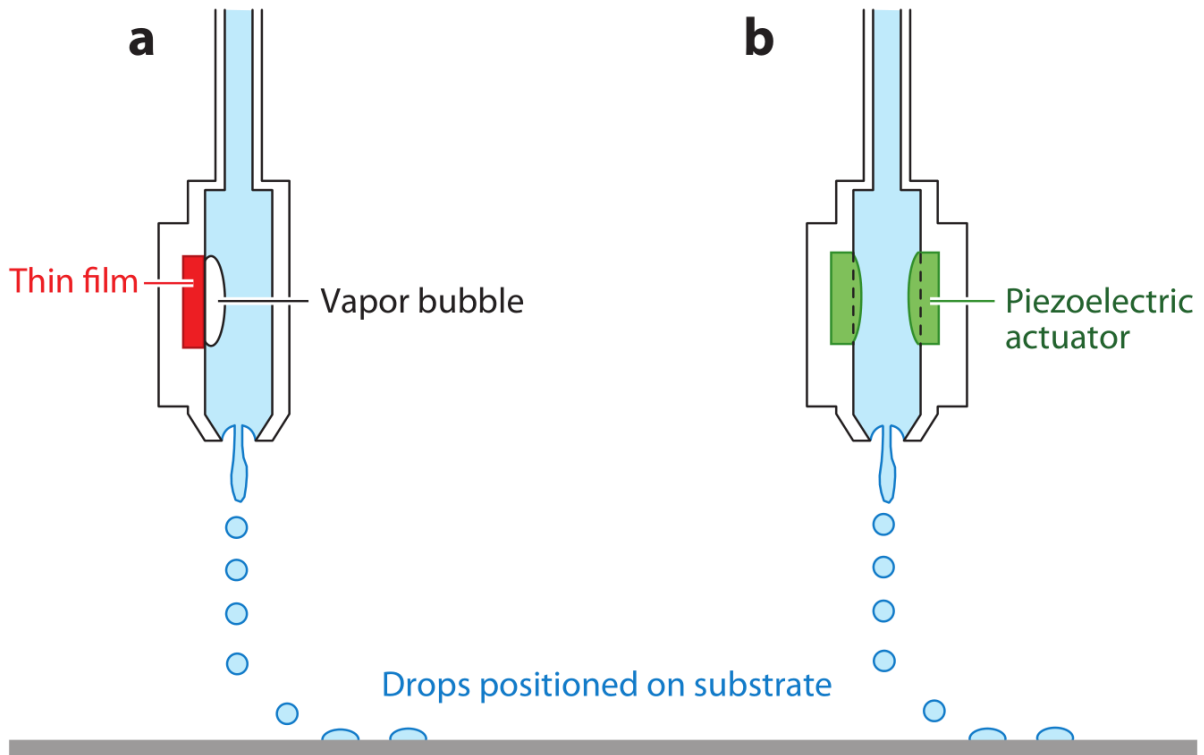
Figure 2.5: Schematic illustration of both **(a)** thermal and **(b)** piezoelectric drop on demand (DOD) printing. From [4].

Thermal DOD printing   uses a small thin-film heater in the fluid chamber to promote drop ejection. By passing a current through the heater, temperatures higher then the fluids boiling point are reached and a small vapour pocket is formed. The bubble collapses due to heat transfer when the current is turned off, and the rapid expansion and collapse generates the pressure pulse required to eject a drop [4].

Piezoelectric DOD printing   utilises a piezoelectric thin-film transducer (energy signal converter) that generates a pressure pulse through direct mechanical actuation caused by

an applied electric field to the film (the converse piezoelectric effect). Piezoelectric ink-jet technology is favoured over thermal ink-jet technology for two reasons [4]:

- Due to the ejection mechanism being non-heating, a larger amount of fluids can be used, not only those of high ambient vapour pressure.

- Because the actuation mechanism is controlled by applying an electric field, it is relatively easy to control drop size and velocity for any fluid.

2.2.2 Previous work on ink-jet printing of SOFC components

Much research has been done in creating components for SOFCs using ink-jet printing technology. Tomov, Krauz, Jewulski et al. used ink-jet printing with suspensions of 5 and 15 wt% YSZ in α-terpineol/methanol with bis(2-ethylhexyl)phthalate as plasticiser and ethyl cellulose as a binder to fabricate gas-tight electrolyte films ~6 μm thick on a porous Ni-YSZ anode support [22]. They also investigated the effect of droplet overlapping on the surface quality of the film and found that

> 'moderate overlapping and repeated coatings can produce a smooth feature-less surface without cracking or delamination.'

Wang, Hopkins, Tomov et al. demonstrated that stable and jettable suspensions of 5 wt% CGO in a 50:50 to 60:40 vol% mix of terpineol and methanol (respectively) with ethyl cellulose as a dispersant (stabiliser) could be successfully produced and used to create dense electrolyte films through ink-jet printing [23]. They also found

> 'the composition of the solvent mixture [...] to be the most critical part of the ink formulation as it influences both the rheological properties and the stability.'

Han, Neoh, Bae et al. successfully fabricated a porous thin-film cathode of LSCF, using a commercial HP ink-jet printer, from aqueous suspensions with 20 wt% 1,5-pentanediol as a stabiliser [24]. They found that

> 'the amount of ink ejection is a critical factor determining not only the deposition rate but also the pore structure in ceramic printing.'

Yashiro, Usui & Kikuta were able to print a thin (~2 μm) intermediate LSCF/GDC cathode
layer onto a GDC electrolyte using an aqueous suspension of 5 wt% LSCF/GDC with a car-
boxylic acid ammonium salt copolymer as a stabiliser [25]. The authors noted that due to
small particle sizes (sub ~0.4 μm)

> 'the cathode layer ha[d] a graded size distribution with respect to depth due to
> the effect of gravity.'

Young, Sukeshini, Cummins et al. used ink-jet printing to fabricate the electrolyte and an-
ode functional layers of a complete SOFC. YSZ was used for both electrolyte and anode
interlayer ink, and two NiO powders of different particle size were added to the interlayer
ink. Both inks had a solid content of 5.6 wt% in α-terpineol with a 5 wt% (of solids) com-
bination of equal amounts of polyvinyl butyral, butyl benzyl phthalate, and polyalkalyne
glycol as binder and plasticiser constituents [26]. The electrolyte and anode interlayer both
had thicknesses of ~6 μm but the authors state that

> 'There is no evidence that this paper demonstrates the minimum electrolyte
> thickness possible by ink-jet printing. [...] future ink-jet printing work might
> even demonstrate the successful fabrication of large-area electrolyte layers with
> thicknesses approaching sub-micron dimensions.'

Ceramic materials for other uses than SOFCs have also been printed into thin films. Özkol,
Ebert, Uibel, Wätjen & Telle developed an aqueous suspension of 65 wt% 3Y-TZP with 10
wt% ethylene glycol as an additive and 1 wt% (of solids) of Dolapix CE 64, that was printed
with a HP desktop printer and sintered to form a ~12 μm film of high density [27]. In their
effort to create the suspension with the right composition, they found

> 'extreme clogging of the nozzles [...] when suspensions with ethanol content
> >7.5 wt% were printed. Ethanol content <7.5 wt% also did not favour the print-
> ing behaviour at all.'

Bakari, Mali & Kuscer successfully fabricated several porous PZTNb films with thicknesses
varying from 4-20 μm by printing an aqueous suspension of 8 vol% PZTNb with 6 wt% (of
solids) polyethyleneimine as dispersant [28]. 20 vol% glycerol and 0.1 wt% phenyl ethoxy-
late were added to adjust the viscosity and surface tension, respectively.

The materials and film thicknesses mentioned above are summarised in Table 2.3

Table 2.3: A summary of some ceramic components that have been fabricated using ink-jet technology

Component	Full name	Thickness [μm]	Source
Anode interlayer			
NiO/YSZ	Nickel Oxide/Yttria-Stabilised Zirconia	~6	[26]
Electrolyte			
YSZ	Yttria-Stabilised Zirconia	~6	[22][26]
CGO	Gadolinium doped Cerium Oxide	~9	[23]
Cathode/ Cathode interlayer			
LSCF	Lanthanum Strontium Cobalt Ferrite	<6	[24]
LSCF/GDC	Lanthanum Strontium Cobalt Ferrite/ Gadolinium doped Cerium Oxide	~2	[25]
Other ceramics			
3Y-TZP	Tetragonal Polycrystalline Zirconia with 3mol% Yttria	~12	[27]
PZTNb	Niobium-modified Lead Zirconate Titanate	3-20	[28]

2.3   Suspensions

The most familiar inks used in ink-jet technology are the graphic printer inks, used to convey a written or pictural message in black, white and/or colour. Graphic inks have two different types of colourants; pigments and dyes. Whereas dyes are organic compounds that are dissolved in a system of liquid carrier media and are present in molecular form, pigments are organic or inorganic white, black or coloured substances that are insoluble in the ink's carrier media. These pigments are solid particles and/or molecular agglomerates in the form of crystals of particle sizes in the range of 0.1 μm to 2 μm, and these must be held stable in the carrier media to form a stable suspension [29, pp.130-131].

"Suspension" is a descriptive name used to designate the two-phase colloidal system consisting of a liquid continuous phase and a solid dispersed phase [30, p. 10]. The word "dispersion" is also often used when referring to dispersed particles of colloidal nature.

Throughout this text the words suspension and ink will be used. A colloidal system can be defined as one where the linear dimensions of the particles involved ranges from 10^{-9}-10^{-6} m (1 nm to 1 µm) [30, p. 1].

To distinguish colloidal particles based on their affinity to the carrier medium they are dispersed in, the two terms *lyophilic* and *lyophobic* are used. Lyophilic means "solvent loving" and lyophobic means "solvent fearing". Better known is the case where water is the medium or solvent, when the terms *hydrofilic* and *hydrophobic* are used. These terms are helpful in describing surface activities such as the wettability of a surface. The surfaces of colloidal particles are seldom uniformly lyophilic or lyophobic, but the terms can still be used to indicate whether the particles behave the one way or the other (attracting or repelling). Lyophilic colloids are said to form true solutions, and true solutions form spontaneously when a solute and a solvent are brought in contact with each other. With no change in temperature or chemical composition, a solution is stable indefinitely. However, when two phases in the colloidal size range are brought together, a finely subdivided suspension does not form spontaneously. The reverse process would actually spontaneously occur, the phases would separate, given the time. It is known from thermodynamics that a decrease in Gibbs free energy defines spontaneous processes [30, p. 14]. The separation of the two phases of a suspension is therefore a process reducing Gibbs free energy. As the two phases separate and form coarser subdivisions, the surface area of the phases reduces, and with it the surface energy [30, p. 15]. This implies that there is a correlation between the surface thermodynamics and the stability of a finely dispersed lyophobic system. Lyophobic systems "dislike" their surroundings and want to separate out whereas lyophilic systems are "happy" in a solution or suspension.

2.3.1   Stabilisation of suspensions

In a suspension that is intended to be used with ink-jet printing technology it is imperative that it is stable. With stable it is meant that the particles in the suspension remain uniformly distributed for a longer period of time. There are many processes occurring in a suspension that might disturb its stability, not only of thermodynamic nature as mentioned above, but also of kinetic nature. These will be examined in detail below.

Processes affecting the stability of a colloidal suspension

The stability of a colloidal suspension is affected by sedimentation and diffusion processes. Sedimentation is caused by the gravitational force acting on the colloidal particles, due to them having a higher density than the surrounding liquid they are pulled to the bottom of the suspension causing a separation of the solid and liquid phase. Diffusion is fundamentally connected to the second law of thermodynamics, wanting to maximise the entropy of a system, distributing molecules evenly throughout the suspension in this case, to even out the concentration gradients [30, p. 79]. *Fick's first law* relates the flux of material through an area to the concentration gradient at the specific location, in one dimension the law is:

$$J = -D\frac{\partial c}{\partial x} \qquad (2.3)$$

where J is the diffusion flux, D is the diffusion coefficient of the solute and $\frac{\partial c}{\partial x}$ is the concentration gradient. The diffusion coefficient is inversely related to the size of a particle. In liquids with small molecules the self-diffusion coefficient of the molecules will typically be in the order of $10^{-9} \, \mathrm{m^2 \, s^{-1}}$ while for colloids it is typically in the order of $10^{-11} \, \mathrm{m^2 \, s^{-1}}$ [30, p. 80].

The molecules in a liquid continually fluctuate in compliance with *Fick's first law*, causing varying pressures on the surface of any particles that are submerged in it. This pressure is very small, but large enough to affect particles in the colloidal size range, displacing them. This displacement will be totally random, reflecting the fluctuations of the molecules, and this kind of movement is called *Brownian motion* [30, pp. 85-86]. Colloidal particles in a suspension can, and often will, crash into each other. Both *Brownian motion*, gravitational forces and other forces causing velocity gradients in the suspension might lead to these particle-particle interactions. These interactions can either lead to a transfer of kinetic energy between the particles, or it can cause them to adhere to each other, forming a larger particle where the initial particles have lost their kinetic independence. This is the coarsening process mentioned in the previous section, that is a cause of segregation. If the particles fuse together, losing their identity and forming a larger particle with a lower surface area, they are said to coalesce. If the particles stick together, but retain their identity and the surface area is not reduced (although some sites are blocked where the particles

touch) the process is called aggregation. In a suspension of solid particles, aggregation is expected to dominate. Whether two colloidal particles in a suspension will form an aggregate or not is mainly governed by the relative magnitude of attractive and repulsive forces between them. Figure 2.6 shows schematically how the net interaction between two particles depends on these relative magnitudes, and the situations where two colloidal particles approaching each other would be thermodynamically unstable, metastable or stable.
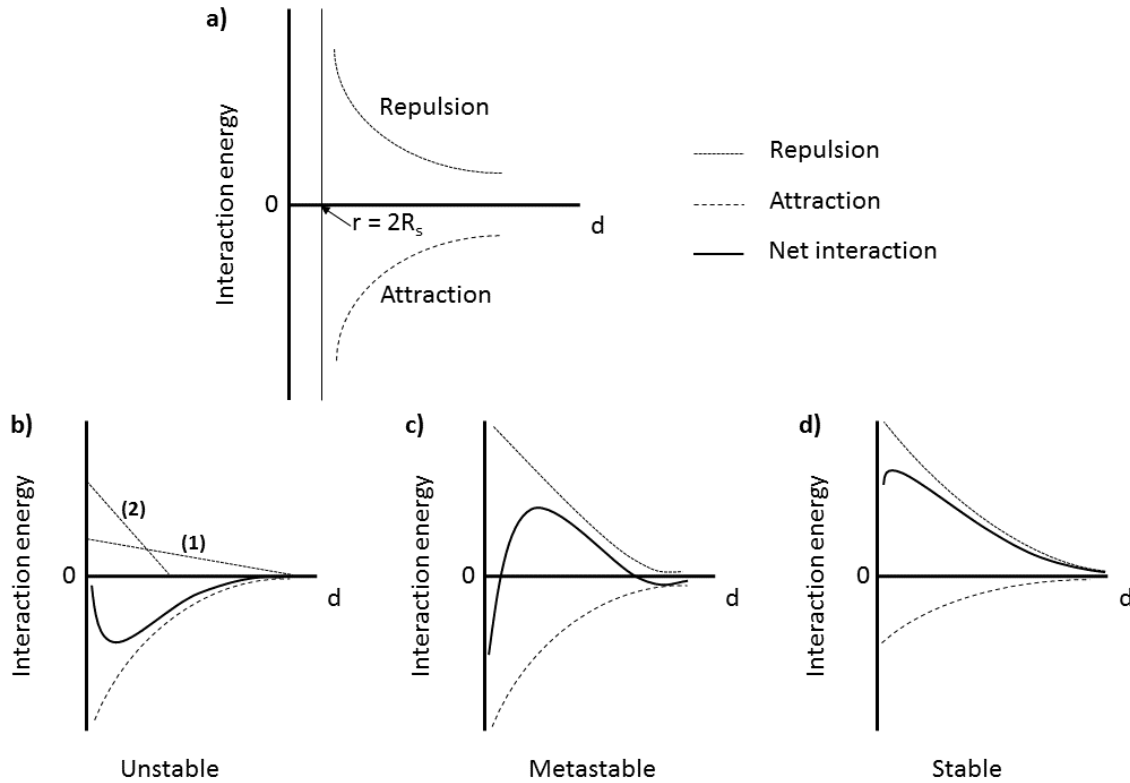
Figure 2.6: Schematic graphs showing potential energy curves for the interaction of two colloidal particles, both of radius **R_s** and a distance **d** apart, and whether or not they will remain stable in a suspension or form an aggregate in the given situation. a) shows the different variables; b) shows a situation where repulsion is smaller than attraction in (1) magnitude and/or (2) range; c) shows the situation where repulsion and atttraction are of comparable magnitude and range; and d) shows a situation where attraction is smaller than repulsion. Redrawn from P. C. Hiemenz and R. Rajagopalan [30, p. 466].

The attractive forces working on the particles are called *van der Waals Forces*. These forces originate from dipole or induced-dipole interactions on an atomic level, and increase with the size of the interacting particles as the particles contain a large number of atoms or molecules [30, p. 462]. The repulsive forces working on the particles are of

electrostatic nature. As a particle is submerged into a liquid, surface charges will generally build up, and this can happen in multiple ways. Some of these are: preferential adsorption of ions already in the liquid, dissociation of surface groups from the particle, adsorption of polyelectrolytes (polymer particles with charges [30, p. 499]) and isomorphic substitution (replacement of ions in a crystalline mineral with other ions of different valency [30, p. 502]. The first is more common than the latter ones. In that case, positively or negatively charged ions will "fight" to cover the particle and hence determine its surface charge. In the case where one species dominates the other, a distinct positive or negative potential will arise. Beyond this first layer of charge, a second layer of ions of opposite charge will be attracted and become loosely bound to the particle. This *electrical double layer* (EDL) is shown schematically in Figure 2.7. In the case that both positively and negatively charged species are adsorbed equally (stoichiometrically), the particle would have zero net charge. This is called the *point of zero charge* [30, p. 503].
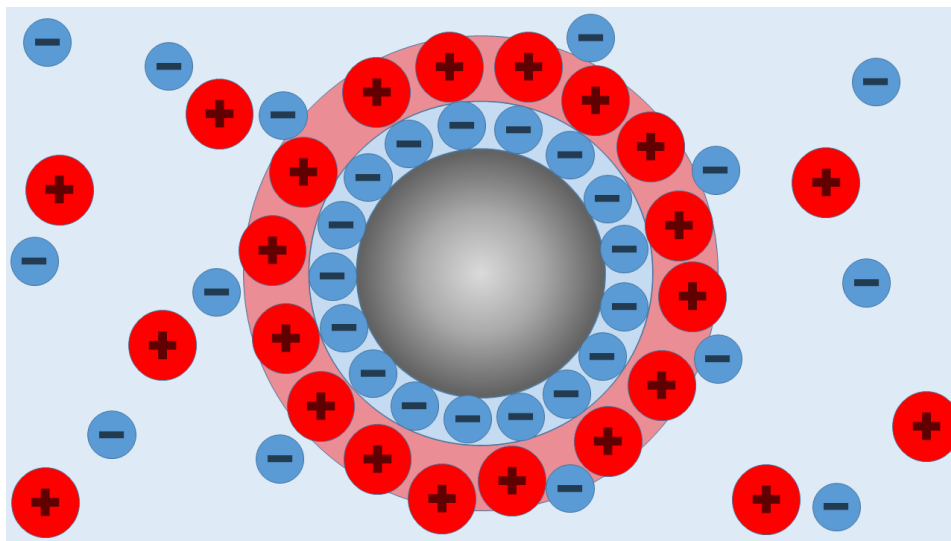
Figure 2.7: Schematic figure showing the buildup of charges around a suspended particle and the formation of the characteristic double layer, indicated in blue and red for negative and positive charges, respectively.

Suspended particles of the same species with electrical double layers that are not at the point of zero charge will act repulsively on one another. This potential energy of repulsion may extend far from the surface of the particle, competing with van der Waals attraction in both magnitude and range to determine how the particles will interact. This fact can be used to affect aggregation phenomena, and a quantitative theory for this electrostatic

stabilisation of suspensions was developed from work done by B. Derjaguin, L. D. Landau, E. J. W. Verwey and J. Th. G. Overbeek, it is generally called *DLVO theory* after their initials [30, p. 524]. P. C. Hiemenz and R. Rajagopalan [30, p. 588] summarises the DLVO theory in these three statements:

1. The higher the potential at the surface of a particle – and therefore throughout the double layer – the larger the repulsion between the particles will be.

2. The lower the concentration of indifferent electrolyte, the longer is the distance from the surface before the repulsion drops significantly.

3. The larger the Hamaker constant, the larger is the attraction between macroscopic bodies.

An indifferent electrolyte is an electrolyte where the constituents are not electroactive, meaning that they do not affect the surface potential of the particle. The Hamaker constant is, in the case of a colloidal suspension, a measure of the relative strength of the van der Waals forces between two particle surfaces. The liquid that the particles interact through will reduce the attraction between the particles [31].

The potential caused by the net electrical charge contained within the electrical double layer up to the surface of shear, indicated in Figure 2.7 by the outer circumference of the weak red circular band, is called the *zeta potential*, ζ. The zeta potential of a suspension can be calculated using theoretical models and experimentally determined data on electrophoretic mobility or dynamic electrophoretic mobility of the colloids. This will however not be discussed in this text. What is important to note is that it is possible to determine the zeta potential of a suspension, and that the zeta potential says something about the electrostatic repulsion between two colloidal particles of equal charge (sign), in accordance with the first statement of the DLVO theory. It can therefore be used as a measure of suspension stability.

Ways to achieve stability

It is important to remember that equilibrium thermodynamics does not give information about the rate at which processes occur. A thermodynamically unstable system, for in-

stance the one shown in Figure 2.6 b) for the case of two colloidal particles in a suspension, can appear stable because of slow kinetics. This can be exemplified analogously by the case of diamonds' thermodynamic instability with respect to graphite. Because of the long time-scale of this transition reaction, it has little practical consequence. The same fact can to a certain extent be used to stabilise lyophobic colloids in a medium. In the previous paragraph different processes that cause instability in a suspension were explained, and a way of counteracting attractive van der Waal-forces through electrostatic means were mentioned. Here, some specific ways of stabilising suspensions will be explained in short:

Electrostatic stabilisation, as explained in the Section 2.3.1, involves building up a double layer around the colloidal particles to keep them apart by electrostatic repulsion, as shown in Figure 2.8 (B.1 and B.2). This can be done by adding an electrolyte to the suspension. The valency of the electroactive species have a major impact on the repulsive forces caused by the build-up of charge on the surface of the particles, in accordance with DLVO-theory. In processing of ceramic materials it is important to be aware of possible contaminants that may end up in the final product when choosing materials and methods. If electrostatic repulsion is of interest, an electrolyte should be chosen that does not leave traces of detrimental character or amount in the end product.

Steric stabilisation involves adding polymers to the suspension. Depending on the type of polymer, colloidal particle and carrier medium, several things may happen. Depending on the affinity of the polymer to the surface of the particles, it may adsorb to the surface. At the correct concentrations this adsorption can lead to polymer chains forming brushlike layers on the particles, as shown in Figure 2.8 (A.1). The spacial extension of the polymer chains from the surface of the particle can be enough to mask out the influence of the van der Waals attraction between two particles, causing them to stay apart and hence stabilise the suspension. This effect of polymer addition is the one called *steric stabilisation* [30, p. 605]. A short comparison of electrostatic and steric stabilisation is given in Table 2.4. Also worth mentioning is the case of a higher polymer concentration, where another stabilising effect may occur. Free flowing polymer chains in large numbers may block the path of particles and hinder them from crashing. This is called depletion stabilisation and is shown

in Figure 2.8 (A.2).

Electrosteric stabilisation   Electrosteric stabilisation is a special case of steric stabilisation where the polymers are polyelectrolytes. It leads to a combination of the electrostatic effects as well as the steric hindrance [30, p. 604]. The charges on the polyelectrolytes can help stabilise their extension into the carrier medium if they repel each other but have an affinity towards the medium, as shown in Figure 2.8 (C.1 and C.2).

Table 2.4: A comparison of electrostatic and steric stabilisation

Edited version of the one found in Hiemenz [30, p. 604]

Electrostatic stabilisation	Steric stabilisation
Addition of electrolyte causes aggregation at a certain concentration.	Insensitive to electrolytes in the case of nonionic polymers.
Usually effective in aqueous systems.	Equally effective for both aqueous an nonaqueous suspensions.
More effective at low concentrations of the suspension.	Effective at both low and high concentrations.
Freezing of the suspension induces irreversible aggregation.	Good freeze-thaw stability.
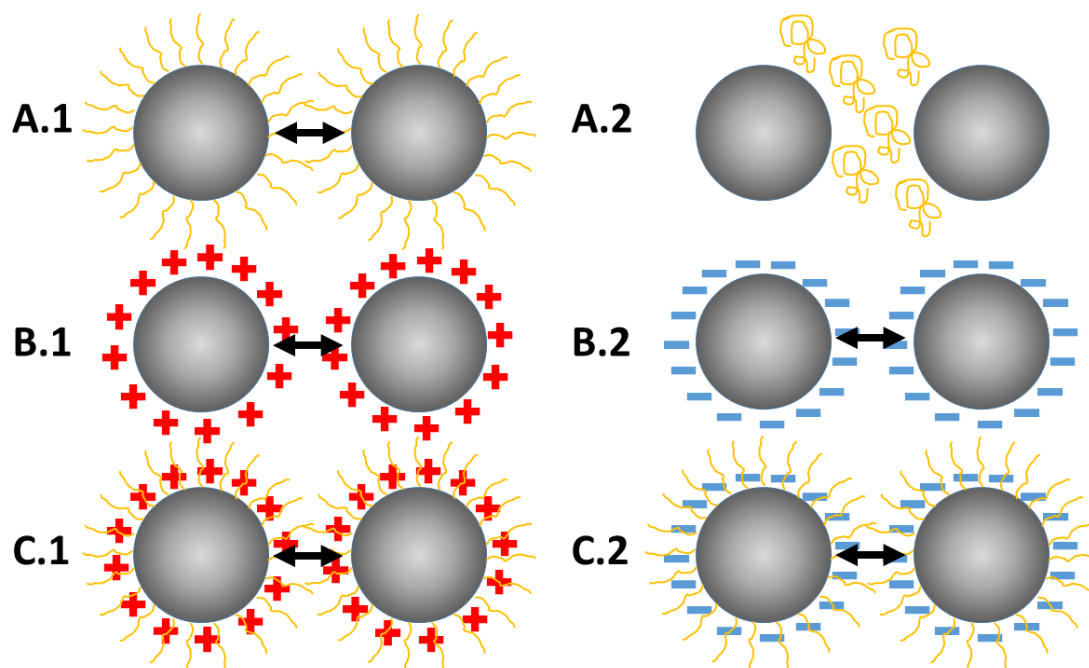
Figure 2.8: Schematic drawing showing different methods of colloidal stabilisation. A.1) Steric stabilisation, A.2) Depletion stabilisation, B.1) Electrostatic stabilisation of net positive EDLs, B.2) Electrostatic stabilisation of net negative EDLs, C.1) Electrosteric stabilisation with positive charges, C.2) Electrosteric stabilisation with negative charges.

2.3.2 Jettability of suspensions

The jettability of a suspension is its ability to form stable droplets that remain stable for a long enough time to reach its target when ejected from the nozzle of an ink-jet print head [2]. Along with stability it is of the most important properties for a suspension which is to be used with ink-jet technology.

Viscosity of suspensions

The viscosity of a substance is its property to flow and be irreversibly deformed when influenced by mechanical stress [29, p. 1124]. For suspensions meant for ink-jet printing it is a key standalone measure of jettability, as jettability is primarily dictated by the viscous and inertial forces [2]. It is therefore an important parameter to consider when the aim is to make a printable suspension. Many parameters influence the viscosity of a suspension, from its constituents to the temperature and shear rate ($\dot{\gamma}$) it is subjected to. The viscosity of the carrier medium/media has the greatest influence on the viscosity of the suspension, but the amount of solids also plays a large role. The viscosity increases with increased solid content [2], and it has been shown for high nanoparticle latex spheres loadings >50 wt% that suspensions can behave in a non-Newtonian manner [32]. Newtonian behaviour will be explained shortly. As explained in 2.2.1, thermal ink-jets increases the temperature of the suspension to eject droplets, and thus it also changes the viscosity of the suspension. This can make it difficult to predict the behaviour of a suspension in the printer, and therefore piezoelectric ink-jet technology is preferable, as it operates at room temperature. In ink-jet printing, the shear rate is quite high and lies in the range of 10^3-$10^5\,\mathrm{s}^{-1}$ [30, p. 151][2]. Knowing how a given suspension behaves up to and within this range is therefore of importance in designing it and for being able to predict its behaviour. There are many models to describe the different behaviours that can be encountered. The simplest of the models is known as *Newtons law of viscosity*,

$$\tau = \eta \times \dot{\gamma} \tag{2.4}$$

where τ is the shear stress, η is the coefficient of viscosity and $\dot{\gamma}$ is the shear rate. Equation 2.4 hypothesises that the shear stress and shear rate are linearly related, and fluids that behave as predicted by Equation 2.4 are said to be *Newtonian* [30, p. 148]. Another way to explain the hypothesis is that the viscosity is independent of applied shear stress or shear rate [32]. Figure 2.9 shows a comparison of the characteristic linear behaviour of Newtonian fluids with several forms of non-Newtonian behaviour.
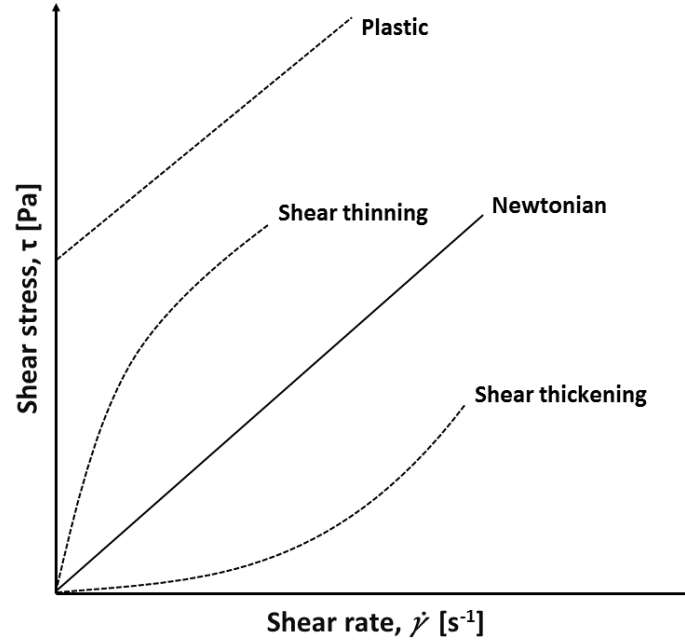
Figure 2.9: Plot showing Newtonian and Non-Newtonian behaviour of fluids. Redrawn from Hiemenz [30, p. 149].

Ohnesorge number

The *Ohnesorge number* (*Oh*) is a dimensionless number relating the shear viscosity (η), density (ρ) and surface tension (σ) of a fluid to the diameter of the orifice from which it is ejected (d_{Oh}), as shown in Equation 2.5. It is named after the Prussian-born Dr. Wolfgang von Ohnesorge, who defined it in his doctoral thesis carried out in the early 1930's at what is now known as the Technische Universität Berlin. Ohnesorge worked with dripping and jetting phenomena of different fluids through a nozzle and after showing four distinct operating regimes for jet breakup he concluded his thesis with defining a dimensionless group that traced the outline of the boundaries between the regimes. This is the definition

that is now commonly referred to as the Ohnesorge number [33].

$$Oh = \frac{\eta}{\sqrt{\rho \sigma d_{Oh}}} \tag{2.5}$$

Several studies related to drop on demand ink-jet printing has used this relation or its inverse, $Z = 1/Oh$, to define regions of stable jetting. Fromm (as cited in Derby [5]) was the first to

> 'identify the Ohnesorge number, Oh, as the appropriate grouping of physical constants to characterise drop generation in an ink-jet printer.'

He defined the parameter Z and proposed that $Z > 2$ ($Oh < 0.5$) for stable drop generation [5]. Other researchers have also tried to define a range of jettability using the Ohnesorge or Z number. Reis and Derby (as cited in [2, 4, 5, 6, 23, 27, 34, 35, 36, 37]) determined the stable range to be $1 \leq Z \leq 10$ ($0.1 \leq Oh \leq 1$), Jang, Kim & Moon defined the range to be $2 \leq Z \leq 14$ ($0.07 \leq Oh \leq 0.5$) [36], Tai, Gan, Liang & Lok found the range to be $0.02 \leq Oh \leq 1.5$ ($0.67 \leq Z \leq 50$). Özkol, Ebert, Uibel, Wätjen & Telle reports creating an aqueous 3Y-TZP suspension with excellent printing properties and $Oh = 0.19$ [27]. These ranges are presented in Table 2.5 for clarity.

Table 2.5: Prevously defined ranges of jettability of a fluid, expressed through the Ohnesorge number, Oh and its inverse, Z

Source	Range of stability [Oh]	Range of stability [Z]
Reis and Derby	0.1-1	1-10
Jang et al.	0.07-0.5	2-14
Tai et al.	0.02-1.5	0.67-50

The inconsistencies in these values suggest that the Ohnesorge number (or Z) cannot define jettability alone. Because it encompasses both the inertial force, viscous force and surface tension, suspensions with very different combinations of surface tension, viscosity and density could have the same Oh number, even though all might not be jettable. Many of these ranges do however overlap, and jettable suspensions are, as shown above, seen in the range of $0.1 \leq Oh \leq 1$ in several cases. Also, the Oh number is independent of ejection velocity and includes the nozzle diameter in its formula, as can be seen in Equation 2.5.

When the nozzle diameter of the printer to be used is known, the Ohnesorge number appears to be a useful guide for selecting fluid properties. Vice versa; when the specifications of the printer to be used is unknown, but the fluid's properties are known, the Ohnesorge number can be a good parameter to use to initially indicate for which range of nozzle diameters a suspension is jettable.

Capillary-Weber parameter space

In their work to develop a way of systematically designing nanoparticle-based ink-jet inks, Nallan, Sadie, Kitsomboonloha et al. developed a jettability window within the Capillary number – Weber number parameter space for Newtonian fluids [2]. The advantage of this criterion for jettability over the Ohnesorge number alone is that it also gives information about the velocity range that a suspension is printable within.
The *Capillary number, Ca,* is defined as;

$$Ca = \frac{\eta v d}{\sigma d} = \frac{\eta v}{\sigma}$$ (2.6)

where η is the shear viscosity and σ is the surface tension of the ink, v is the droplet velocity and d is the diameter of the nozzle orifice. It relates the effects of viscous forces and surface tension acting across an interface between a liquid and a gas, in the case of ink-jet printing.
The *Weber number, We,* is defined as;

$$We = \frac{\rho v^2 d^2}{\sigma d} = \frac{\rho v^2 d}{\sigma}$$ (2.7)

where ρ is the density of the ink and the other parameters are the same as described for the *Ca* number. The Weber number relates the effects of the inertia and surface tension of a fluid.
Nallan et al. employed the *Ca–We* space because it allowed them to

> '...normalise the minimal effect of the surface tension force, highlight the impact of the viscous and inertial forces, and compare the jettability across ink systems.'

They argued that since d is constant and ρ and σ do not vary significantly between the ink

systems they compared, the Ca and We numbers are primarily determined by v and η. By plotting experimental data of multiple solvent systems that were known to be jettable, they defined the area within the Ca–We space marked as grey in Figure 2.10.
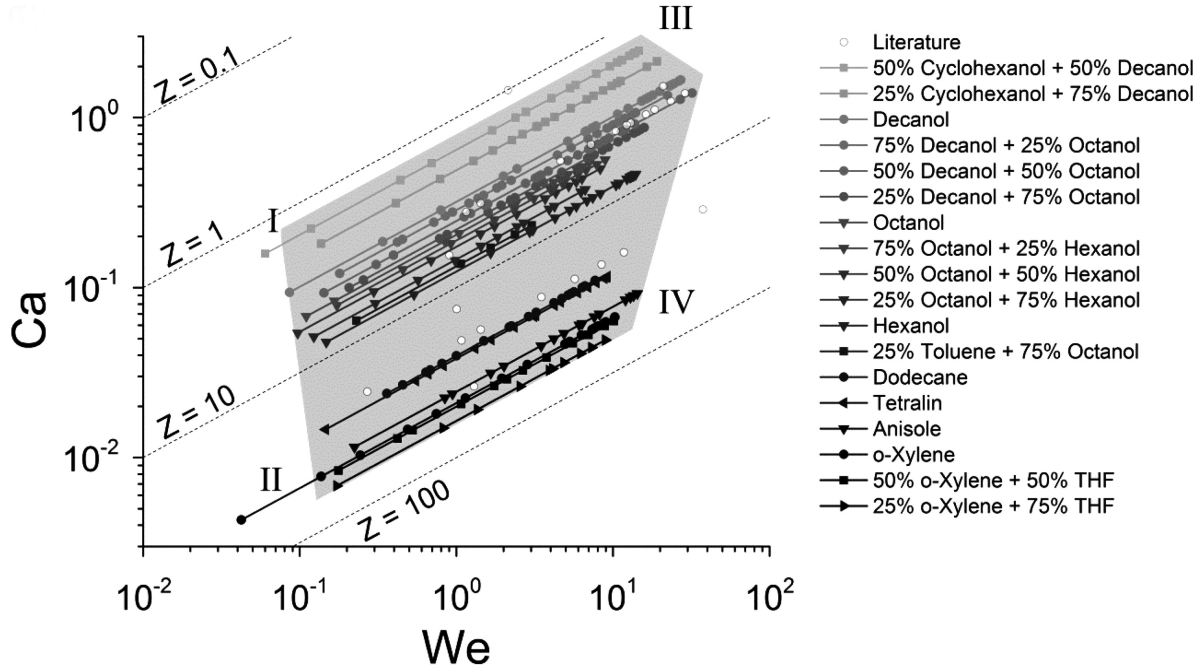
Figure 2.10: Jettability window in Ca–We parameter space as defined by Nallan et al. [2]. Z is the inverse of the Ohnesorge number, as expained in Section 2.3.2 under "Ohnesorge number". Enumerated areas I, II, III and IV indicate regions of different characteristic jetting stability breakdown mechanisms.

As can be seen, each ink is plotted on a log-log scale, resulting in data that lies along a line with a slope equal to ½. This is due to the fact that $Ca \propto v$ and $We \propto v^2$, and because η in fluids that behave Newtonian is constant across all shear rates (see Section 2.3.2 on viscosity), and therefore also ejection velocities. As the data is normalised by surface tension, each line visually represents an individual ink ejected at different velocities. The length of the lines are determined by the range of velocities where the given ink is jettable. Higher Ca values indicates more viscous inks and the lines for the different inks lie parallell to each other with the most viscous inks at the top and the least viscous at the bottom. A result of the sloped nature of a given ink system is that an ink lying above or below the jettability window will be unjettable for all velocities.

Areas marked I, II, III and IV in Figure 2.10 indicate regions of different characteristic jetting stability breakdown mechanisms. To understand them it is necessary to know that

the velocity of a fluid out of a nozzle is directly related to the amplitude and waveform of the voltage applied to the piezoelectric transducer causing the pressure that pushes the fluid out of the nozzle [2, 38, 39]. In region I and II, with low We numbers, the amplitude of the voltage pulse applied to the piezoelectric transducer is too low to eject a drop. In region III, with both high Ca and We numbers, the pillar of fluid that is ejected becomes too long before it is released from the nozzle, leading to the formation of satellite drops due to Rayleigh instability along the tail of the droplet (similar to what happens in CIJ inkjet printing, see Section 2.2). In region IV, with low Ca and high We numbers, fluids with low viscosity are ejected at high speeds. A wavelike instability in the ejected column of ink causes multiple breakups and a spraying behaviour. All four stability breakdowns are illustrated in Figure 2.11.

The local maximum in Weber number between region III and IV indicates the condition where a fluid is viscous enough to withstand instabilities due to higher velocities but not so viscous that the ejected pillar of ink becomes excessively long and results in satellite droplets. Nallan et al. makes a note of the interesting fact that the jettability window spans Z values from approximately 1 to 60, which encompasses the ranges of Z-values/Ohnesorge numbers that are suggested in literature for jettable suspensions (see Section 2.3.2 under "Ohnesorge number") [2].
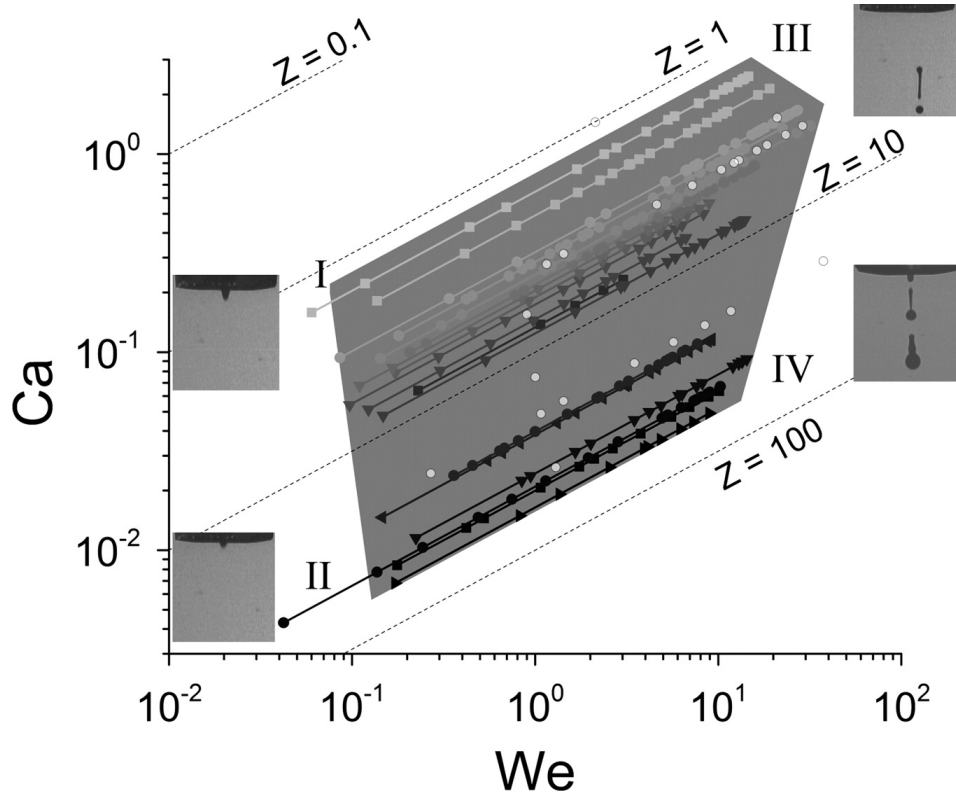
Figure 2.11: Jettability window in Ca–We parameter space as defined by Nallan et al. [2]. Z is the inverse Ohnesorge number, as expained in Section 2.3.2 under "Ohnesorge number". Enumerated areas I, II, III and IV indicate regions of different characteristic jetting stability breakdown mechanisms and images of the different stability breakdowns are shown.

Weber-Reynolds parameter space

Derby defined and refined an area in the Weber number – Reynolds number parameter space that indicates fluid jettability for Newtonian fluids [3, 5, 6]. This jettability criterion also contains more information than the Ohnesorge number alone, and does not normalise by the surface tension as is done in the Ca–We space. The *Reynolds number*, *Re*, is defined as

$$Re = \frac{\rho v d}{\eta} \tag{2.8}$$

where ρ is the density of the ink, v is the droplet velocity, d is the diameter of the nozzle orifice and η is the shear viscosity. The *Re* number relates the inertial and viscous forces of a fluid.

The jettable area is shown in Figure 2.12. It is bound by several criteria for stable and acceptable drop ejection. From the bottom it is limited by the lowest *We* number required

for drop ejection to overcome the surface tension, meaning the lowest velocity and there-
fore required applied voltage amplitude to the piezoelectric transducer. This is according
to Derby [6] when:

$$We_{min} = v_{min}\left(\frac{\rho d}{\sigma}\right)^{1/2} = 4 \tag{2.9}$$

From the top, the area is limited by the highest drop velocity that it is possible to eject the
droplet at without the droplet splashing when it impacts the substrate. Derby references
the work of Stow and Hadfield [40] as well as Bhola and Chandra [41] that found this to be
when:

$$We^{1/2}Re^{1/4} = f(R) \approx 50 \tag{2.10}$$

On the left hand side the area is limited by when the fluid is too viscous to be ejected,
which Derby has chosen to define as when the Z parameter is equal to 1, and on the right
hand side the area is confined by when the fluid has such a low viscosity that ejection leads
to satellite drop formation, defined as when Z equals 10. This is in accordance with the
findings explained in Section 2.3.2 on the Ohnesorge number.
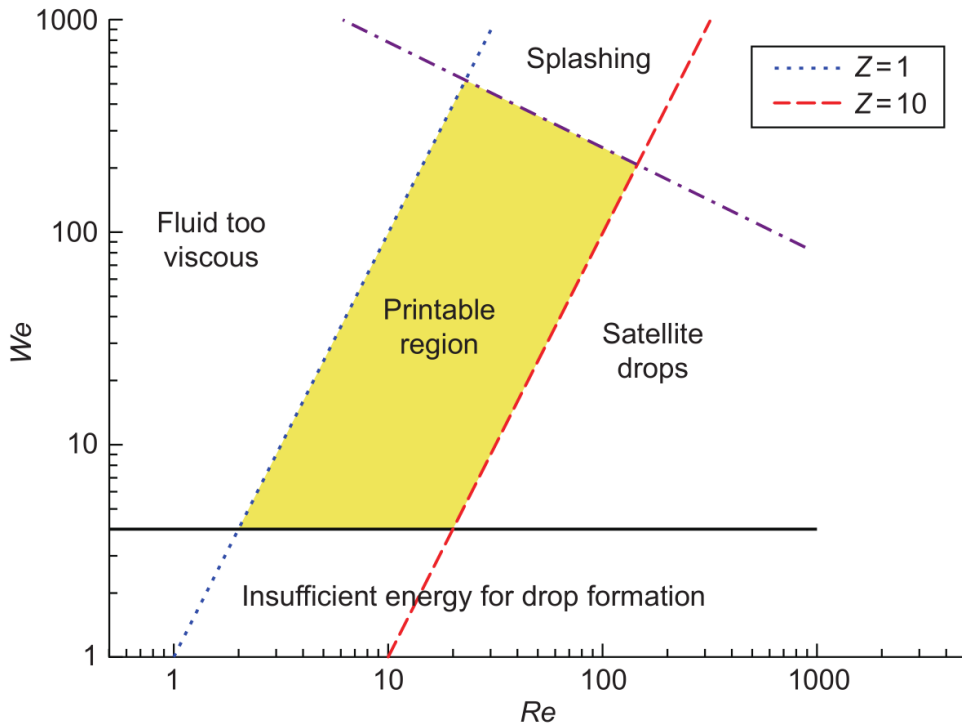
Figure 2.12: Jettability window in We–Re parameter space as defined by Derby [6]. Z is the
inverse Ohnesorge number, as expained in Section 2.3.2 under "Ohnesorge number".

Chapter 3

Experimental

The experimental part of this work is divided into four parts, suspension manufacturing, suspension characterisation, printing of suspensions and printout evaluation. All experiments were conducted using $(La_{0,8}Sr_{0,2})_{0,995}CoO_3$-powder received from CerPoTech AS. The powder was produced through spray pyrolysis, and it was subsequently calcined at $600\,°C$ for 6 hours, dry milled for 1 hour, wet milled for 48 hours, dried, sieved and fired at $400\,°C$ for 6 hours [42].

3.1 Suspension manufacturing

Ten suspensions of LSC were made with their compositions based on the results from the work done by Rogstad [1]. In the cited work, a large number of different suspensions were made in an effort to find a combination of liquids and dispersants that would keep the LSC-powder stable in suspension, as well as have favourable properties for printing. The suspensions in this work are divided into two distinctly different series of five. One of the series is based on the most stable suspension using organic media and the other on the most stable water based suspension from Rogstad's work.

3.1.1 Materials

Table 3.1 shows the different chemicals used in the making of the suspensions, as well as some of their properties and the supplier. The different substances were originally chosen

by Rogstad [1] based on availability and information found in literature about ink-jet print-ing of ceramics. This especially applies to Dolapix CE64 which has been shown to work well with high solid content ceramic suspensions [27, 43].

Table 3.1: List of materials, materials' properties and suppliers

Substance	Density [g/cm^3 (25 °C)]	Molecular weight [g/mol]	Supplier
Powder			
$(La_{0,8}Sr_{0,2})_{0,995}CoO_3$	6.974*	235.58	CerPoTech AS
Carrier media			
α-Terpineol	0.93	154.25	Sigma-Aldrich Co. LLC.
Isopropanol	0.79	60.10	VWR Chemicals
Distilled water	0.998	18.016	From an EMD Millipore Elix Essential
Ethylene Glycol	1.11	62.07	VWR Chemicals
Dispersant			
Polyvinylpyrrolidone (PVP)	-	58000**	Alfa Aesar (now Thermo Fisher (Kandel) GmbH)
Dolapix CE 64	1.20	-	Zschimmer & Schwarz GmbH & Co

*Value from PDF card 04-014-5178

**Average molecular weight

3.1.2   Methods

Table 3.2 shows all the planned suspensions and their compositions. All amounts are given in weight percent out of the total weight of the suspension, unless otherwise stated. There are two distinctly different series of five suspensions hereby called the AIP series and the EWD series. The name of each suspension is an acronym that indicates the suspension's composition from the initials of the carrier medium, additive, dispersant and wt% of ad-ditive in the final suspension. For example, **AIP1** stands for **A**lpha-Terpineol, **I**sopropanol, **P**olyvinylpyrrolidone and **1**0 wt% isopropanol. The suspensions are referred to by these names throughout the document and the reader can use this system to remember their composition without returning to Table 3.2. The five suspensions within both the AIP and the EWD series are similarly composed with the only varying factor being the relation be-tween the amount of carrier medium and additive. Indeed the additive content surpasses the carrier medium content in the 40 and 50 wt% additive suspensions, but for consistency it is still referred to as the additive.

Table 3.2: List of suspensions that were planned and their composition
PVP is the abbreviation of Polyvinylpyrrolidone

Sample	wt% LSC	Carrier medium	Additive	wt% Additive	Stabiliser	wt% Stabiliser (of wt of solids)
AIP series						
AIP1	20	α-Terpineol	Isopropanol	10	PVP	2
AIP2	20	α-Terpineol	Isopropanol	20	PVP	2
AIP3	20	α-Terpineol	Isopropanol	30	PVP	2
AIP4	20	α-Terpineol	Isopropanol	40	PVP	2
AIP5	20	α-Terpineol	Isopropanol	50	PVP	2
EWD series						
EWD1	20	Ethylene glycol	Distilled water	10	Dolapix CE 64	2
EWD2	20	Ethylene glycol	Distilled water	20	Dolapix CE 64	2
EWD3	20	Ethylene glycol	Distilled water	30	Dolapix CE 64	2
EWD4	20	Ethylene glycol	Distilled water	40	Dolapix CE 64	2
EWD5	20	Ethylene glycol	Distilled water	50	Dolapix CE 64	2

The suspensions were made using a Mettler Toledo AG204 DeltaRange analytical balance (1 mg readability), in the following way:

Predetermined amounts of the dispersant (PVP, Dolapix CE 64), the additive (isopropanol, distilled water) and the carrier medium (α-terpineol, ethylene glycol) were weighed directly into a plastic bottle with screw top (100 ml) for each of the ten suspensions. LSC-powder was weighed in a disposable weighing boat and added to the bottles. This process demands greater care than individually weighing every component in weighing boats, but removes the inaccuracy due to transfer of the materials from a weighing boat or beaker to the bottle. Table 3.3 shows the measured weight of every component of every suspension and the resulting weight percent of the component.

Yttria Stabilised Zirconia (YSZ) grinding media with a diameter of 5 mm was added to the bottles so that the total amount of suspension and grinding media filled roughly 40% of the bottle. The suspensions were then milled on a U.S. Stoneware 700 series jar mill at approximately 190 rounds per minute (rpm) for 24 hours. After the milling process the suspensions were removed from the bottles by syringe and subsequently filtered through 2 µm borosilicate glassfiber syringe filters and into glass vials. The ten resulting suspensions are the ones used in all the following work. To prevent sedimentation the vials were stored on a CAT roller of the type RM10W-30V at a slow speed between characterisation and printing tests.

Table 3.3: Measured weights of each component in each suspension and the resulting wt% of that component in the final suspension, rounded to two decimal points. Total weight of the suspension is also given.

Sample	Carrier medium [g]	Additive [g]	LSC [g]	Stabiliser [g]	Total Wt [g]
AIP series					
AIP1	16.9010	2.4280 (10.00 wt%)	4.8537 (19.99 wt%)	0.0980 (2.02 wt% of solids)	24.2807
AIP2	14.0297	4.7050 (19.99 wt%)	4.7041 (19.99 wt%)	0.0936 (1.99 wt% of solids)	23.5324
AIP3	11.3230	6.8470 (30.00 wt%)	4.5625 (19.99 wt%)	0.0920 (2.02 wt% of solids)	22.8245
AIP4	8.7701	8.8578 (40.00 wt%)	4.4293 (20.00 wt%)	0.0892 (2.01 wt% of solids)	22.1464
AIP5	6.3692	10.7578 (50.00 wt%)	4.3034 (20.00 wt%)	0.0862 (2.00 wt% of solids)	21.5166
EWD series					
EWD1	19.1635	2.7607 (10.02 wt%)	5.5053 (19.99 wt%)	0.1101 (2.00 wt% of solids)	27.5396
EWD2	16.1788	5.4287 (20.00 wt%)	5.4284 (20.00 wt%)	0.1088 (2.00 wt% of solids)	27.1447
EWD3	13.2788	8.0310 (30.00 wt%)	5.3546 (20.00 wt%)	0.1073 (2.00 wt% of solids)	26.7717
EWD4	10.4590	10.5648 (40.00 wt%)	5.2823 (20.00 wt%)	0.1055 (2.00 wt% of solids)	26.4116
EWD5	7.7145	13.0305 (50.00 wt%)	5.2124 (20.00 wt%)	0.1043 (2.00 wt% of solids)	26.0617

3.2   Suspension characterisation

3.2.1   Solid loading

To determine how much of the initial powder content of 20 wt% that remained in the final suspensions after the milling and filtering steps, burn-off tests were performed. Alsint crucibles with enough kaowool to cover the opening were heated to ~200 °C in an oven for several hours to remove any moisture. Each set of crucible and kaowool were then weighed. A small amount of each suspension (~0.5 ml) was put into separate crucibles and covered with the kaowool, which was then weighed again. The crucibles were then heated to 600 °C and held there for two hours to ensure evaporation of moisture and burn-off of all organic species. The heat-treated crucibles were taken out of the oven at ~100 °C to prevent any adsorption of moisture and immediately weighed.

3.2.2   Density

The densities of all suspensions were measured by placing a vial containing a sample on a Mettler Toledo AG204 DeltaRange analytical balance (1 mg readability) and using a Finnpipette F2 [5000 ± 40.0 µl [44]] with a disposable tip to remove 5.00 ml of suspension. The measurements were repeated between 5-13 times for each suspension. The absolute value of

the weight removed from the vial and the removed volume were then used to calculate the density of the given suspension. Tests on distilled water were run prior to the measurements of the suspensions to ensure that the pipette was correctly calibrated. The room temperature was measured to be approximately 23 °C at the time of the experiment. The distilled water and suspensions had been in the room for a long enough time to be assumed to be at room temperature.

3.2.3 Particle size distribution

A Horiba Partica LA-960 Laser Diffraction Particle Size Distribution Analyser was used to measure the particle size distribution (PSD) in the suspensions. Before analysis the suspensions were sonicated using an ultrasonic rod transducer for one minute at 30 % intensity to break soft agglomerates. A small number of drops from the topmost part of the suspensions were then dispersed in isopropanol within the apparatus' chamber and circulation was turned on. A refractive index of 1.700 - 1.000i was used for the dispersed solids, and 1.378 for the continuous medium, isopropanol. The ensuing analysis employed the following procedure to ensure consistent and reliable measurements:

1. Two measurements, five minutes after initial ultrasonication
2. Wait three minutes
3. One measurement
4. In-situ ultrasonication for one minute at full intensity (setting "7")
5. Two measurements
6. Wait three minutes
7. One measurement

This resulted in six sets of data for each suspension which were used to analyse the particle size distribution of the given suspension.

Particle stability

To get a better understanding of the sedimentation and agglomeration processes occuring in the suspensions over time, the suspensions were left standing still on a flat countertop for two days after the initial round of particle size distribution measurements. This allowed

the natural sedimentation and agglomeration processes to occur as they would in a storage room environment. Four to eight drops of the topmost part of the suspensions were subjected to the same measuring procedure as the one above, except for the initial ultrasonication which was left out.

Determination of PSD from laser diffraction techniques [45]

The idea behind laser diffraction as a technique for determining the particle size distribution is that particles will scatter light at different angles depending on their size. Large particles will scatter at smaller angles and smaller particles at wider angles. When a collection of particles is subjected to illumination a pattern of scattered light will be produced that is defined by intensity and angle, and this pattern can be transformed into a PSD result.

The resulting distribution can be calculated based on the number, surface area or volume of particles of a certain diameter. The number and volume based distributions are the most commonly used. *Number based distributions* assigns a size value to each inspected particle, and all particles have an equal weighting in the final distribution as a percentage of the total amount of particles. *Volume based distributions* displays the particle sizes as a percentage of the total volume of particles. As an example of this, consider nine spherical particles where three have a diameter of 1 μm, three of 2 μm and three of 3 μm. A number based distribution of these particles will generate the result seen in plot **(a)** in Figure 3.1, while a volume based distribution would result in **(b)**. From a number based perspective each particle in **(a)** accounts for one third of the total amount of particles, while in a volume based distribution 75 % of the total volume comes from the 3 μm particles, ~22.2 % from the 2 μm particles and ~2.8 % from the 1 μm particles.

(a) Number based distribution

(b) Volume based distribution
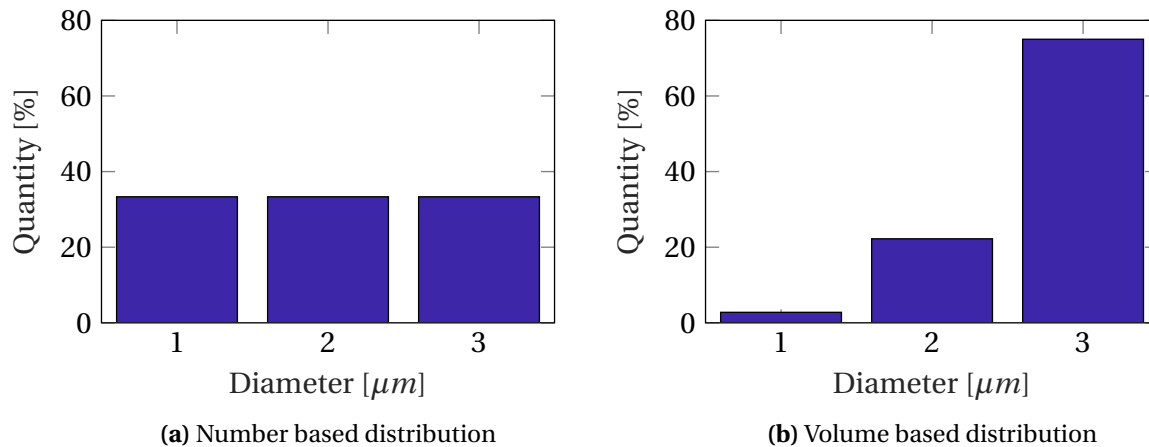
Figure 3.1: Number based **(a)** vs volume based **(b)** distributions for nine particles where three sets of three have diameters of 1, 2 and 3 μm respectively.
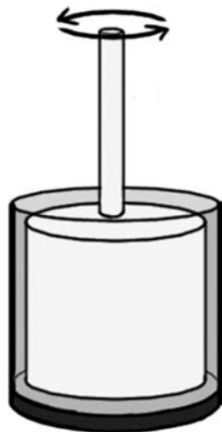
3.2.4 Viscosity

Viscosity measurements were done using a Haake Mars III Rheometer from Thermo Fisher Scientific with a concentric cylinder setup, as shown in Figure 3.2. All suspensions were measured in a range of shear rates from 0 to $1000 \, \text{s}^{-1}$. The measurements were done at a constant temperature of $25.0 \, °C$ and followed the program presented in Table 3.4. The α-terpineol, isopropanol and ethylene glycol used as the liquid components of each suspension were also measured in pure form using the same equipment and procedure.

Table 3.4: Program used to measure the viscosity of the ten manufactured suspensions

Step	Data points	Shear rate $[\dot{\gamma}]$
1	250	0-1000
2	15*	1000
3	250	1000-0

*30 data points for EWD3-5 and for the pure liquids

Figure 3.2: Illustration of the concentric cylinder experimental setup for determination of viscosity [46]. The rotating cylinder is hollow on the inside and surrounds a metal rod, creating a double gap.

3.2.5 Surface tension

Surface tension was measured using a Krüss DSA100 Drop Shape Analyser in the pendant drop setup. A small amount of each suspension was sucked into a 3 ml BD Luer-Lok tip syringe with a blunt headed needle with an outer diameter ranging from 1.827-1.844 mm, as measured by a digital calliper. The syringe was then placed as shown in Figure 3.3 with air surrounding it. The measuring procedure was as follows: The density of the suspension was entered into the apparatus' software and air was chosen as the continuous phase surrounding the needle. Video recording at 120 frames per second was started in the software and 20-30 drops were manually ejected from the syringe. Upon frame-by-frame playback of the film, the frames that captured the drop right before filament breakup were analysed using the ADVANCE software provided by the manufacturer. A brief description of how the surface tension is calculated from these still images will follow.
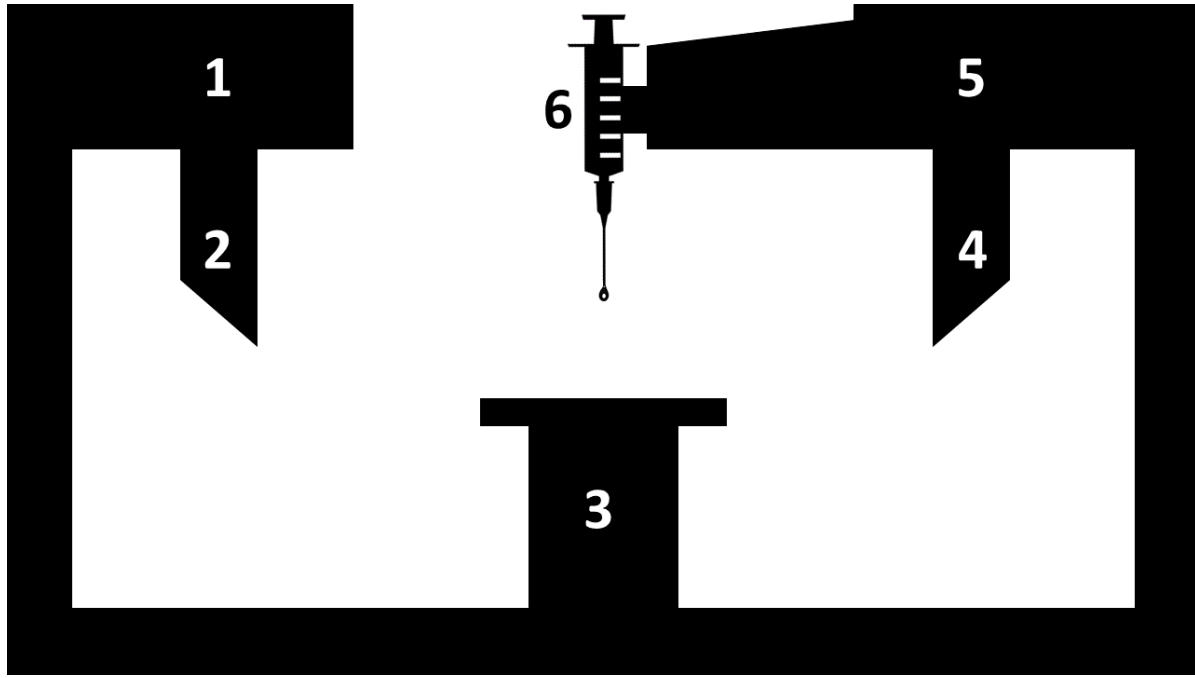
Figure 3.3: Schematic of the experimental setup in a Krüss DSA100. 1) High resolution digital camera, 2) Prism, 3) Adjustable table, 4) Mirror, 5) Lamp, 6) Manual syringe. Redrawn from Rogstad [1].

Calculation of surface tension from still images [47, 48]

Greyscale analysis is first used to find the shape of the drop in each image. A shape parameter, the *Bond* number β, is then numerically calculated from a set of dimensionless differential equations (Eqs. 3.2, 3.3 and 3.4) derived from the Young-Laplace equation (Eq. 3.1). The Young-Laplace equation relates the Laplace pressure across an interface with the curvature of the interface and the interfacial tension (called surface tension in the case of a gas-liquid interface), σ:

$$\Delta P = \Delta P_0 - \Delta \rho g z = \sigma \times \left(\frac{1}{r_1} + \frac{1}{r_2} \right) \tag{3.1}$$

where $\Delta P \equiv P_{in} - P_{out}$ is the Laplace pressure across the interface; $\Delta \rho = \rho_d - \rho_c$ is the density difference between the drop phase, ρ_d, and the continuous phase, ρ_c, respectively; and r_1 and r_2 are the principal radii of curvature. The pressure difference is written in terms of a reference pressure ΔP_0 at $z = 0$ and a hydrostatic pressure $\Delta \rho g z$. Equation 3.1 can be expressed in the cylindrical coordinates r, z and φ, as shown in Figure 3.4. It can then be formulated as the set of dimensionless differential equations defined by the arc length, s,

measured from the apex of the drop:

$$\frac{d\varphi}{d\bar{s}} = 2 - \beta\bar{z} - \frac{\sin\varphi}{\bar{r}} \tag{3.2}$$

$$\frac{d\bar{r}}{d\bar{s}} = \cos\varphi \tag{3.3}$$

$$\frac{d\bar{z}}{d\bar{s}} = \sin\varphi \tag{3.4}$$

where $\bar{r}$, $\bar{s}$ and $\bar{z}$ are dimensionless quantities scaled by R_0, the radius of curvature at the apex of the drop.

When the shape parameter β has been determined from these differential equations and the drop radius R_0 at the apex is found, the surface tension can be calculated from the definition of the Bond number:

$$\beta \equiv \frac{\Delta\rho g R_0^2}{\sigma} \tag{3.5}$$

where $\Delta\rho$ still is the density difference between the drop phase and the continuous phase, g is the acceleration due to gravity and the remaining factors are as earlier explained.
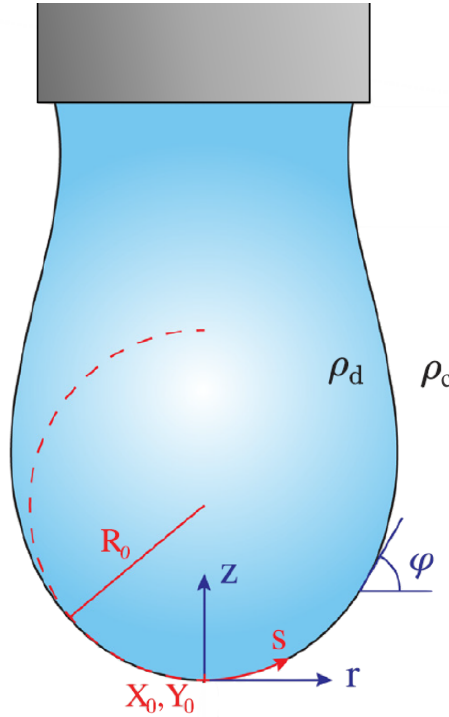
Figure 3.4: Schematic of a pendant drop below a needle. Cylindrical coordinates r, z and φ are indicated along with the arc length s, the apex drop radius R_0 and the drop and continuous phase densities ρ_d and ρ_c. Modified from Berry, Neeson, Dagastine et al. [47].

3.3 Printing of suspensions

An Epson WorkForce® WF-2630 was used as the printing unit. It uses piezoelectric MicroPiezo® ink-jet technology with a resolution of 5760 x 1440 dpi (drops per inch) and is capable of producing droplets of three sizes, as small as 3 pL [49]. The nozzle diameter was found to be 21.8 µm with a sample standard deviation of 0.7 µm, as determined by scanning electron microscopy of twelve different nozzles. Figure 3.5 shows an SEM micrograph of several nozzles on the printhead, while detailed micrographs of all twelve nozzles are given in Appendix C. The printer was chosen primarily because of the piezoelectric jetting technology which is compatible with a larger amount of fluids than thermal ink-jets (see Section 2.2.1), and because there were empty cartridges available for the model.
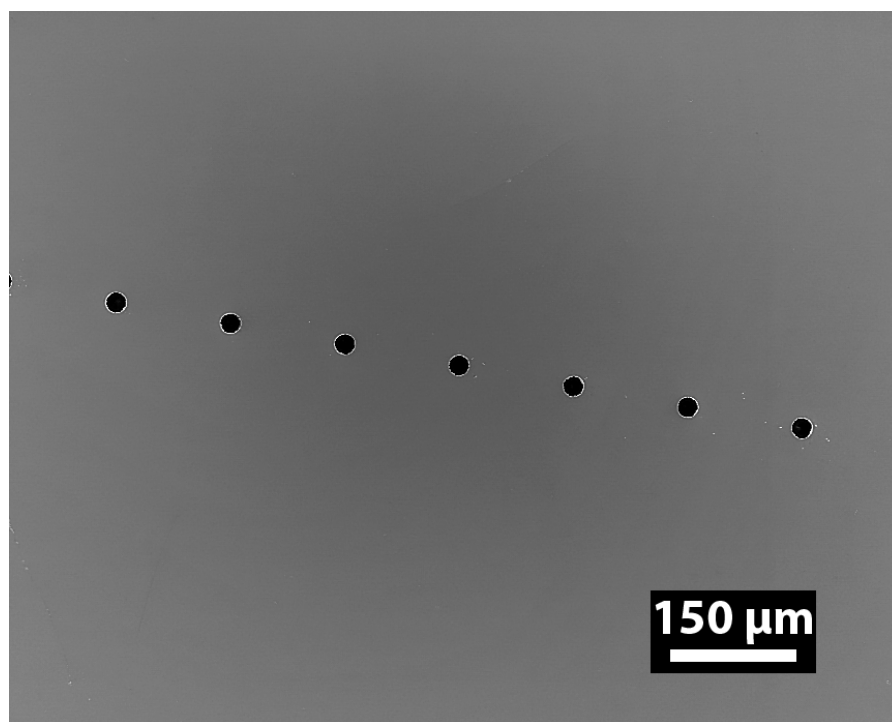
Figure 3.5: SEM micrograph of the Epson WorkForce® WF-2630 printhead.

The printing procedure was done as follows:

Each suspension was ultrasonicated for one minute at 30 % intensity before being loaded into an empty 16XL compatible ink cartridge by syringe and installed in the printer as the black ink cartridge. The commercial black ink coming with the printer was placed in the cyan cartridge slot of the printer and two dummy cartridges were installed as yellow and

magenta. Uncoated 4CC® 160 g premium A4 paper was used as the printing substrate. Each suspension was printed on an individual paper sheet in 1, 2, 3, 4, 5, and 10 layers, letting each layer dry before printing the next. The printhead was flushed with ethanol between the printing of each suspension. Pdf templates for the printed layers can be seen in Appendix D. The templates were made in MS Word®. In the first template, black squares with sides of 1 cm were spaced out across six rows of five squares each. The transparency of the black squares was then varied from 0 to 80 % within each row, denominated T-0, T-20, T-40, T-60 and T-80 in the template. This was done to create different greylevels that causes the printer to vary the drive frequency, amplitude and waveform of the voltage it applies to the piezoelectric film to eject droplets, which in turn affects the size and speed of the drop out of the nozzle [2, 38, 39]. These are parameters that ideally would be directly controlled, but this was not possible with the printers available in the frame of this work. The parameters are therefore indirectly controlled as described with the goal of drop ejection for at least some of the levels of transparency.

3.4   Printout evaluation

The printed sheets were left to dry for several hours and were then scanned on a regular office scanner before further analysis. Complete page scans of the five printed suspensions: AIP3, AIP4, AIP5, EWD1 and EWD4, are given in Appendix E.

A Wild Heerbrugg Photomakroskop M400 optical microscope fitted with a Leica DFC450 camera and a volpi intralux 5000 light source was applied to obtain more detailed overviews of the individual printed squares than was possible using the office scanner. Bright field images were captured and used to determine which squares to study further. The ten-layered square of 20 % transparency (T-20) was chosen for the AIP3, AIP4, EWD1 and EWD4 suspensions and the ten-layered T-0, T-20 and T-40 squares for the AIP5 suspension. The three transparency levels of the AIP5 was chosen to better see the trend for an individual suspension. The squares were coated in gold using an Edwards Sputter Coater S150B at 15 mA for 30 s and subjected to further analysis in a Zeiss Supra 55VP low vacuum field emission scanning electron microscope. The secondary electron (SE) detector was employed at an accelerating voltage of 15 kV and an aperture of 20 μm.

Chapter 4

Results

4.1 Suspension manufacturing

This section presents data related to the method of manufacture of the suspensions.

4.1.1 Suspension retrieved after ball milling

The amount of each suspension that was retrieved from the plastic bottle by syringe after the milling procedure is presented in Table 4.1. Except for AIP5, all suspensions had a retrieval rate well above 90 % with a median of 94.79 % for the AIP suspensions and 94.87 % for the EWD suspensions.

Table 4.1: The amount of suspension retrieved from the milling bottle after the milling process, by weight (g) and as a percentage of the weight of the initially made suspension An expanded version can be seen in Table B.1 in the Appendix

Sample	Suspension made	Suspension retrieved	
AIP series	[g]	[g]	[%]
AIP1	24.2807	22.479	**92.58**
AIP2	23.5324	22.413	**95.24**
AIP3	22.8245	21.716	**95.14**
AIP4	22.1464	20.993	**94.79**
AIP5	21.5166	17.306	**80.43**
EWD series			
EWD1	27.5396	25.631	**93.07**
EWD2	27.1447	25.714	**94.73**
EWD3	26.7717	25.667	**95.87**
EWD4	26.4116	25.196	**95.40**
EWD5	26.0617	24.724	**94.87**

4.2 Suspension characterisation

The results that are reported in this section are related to characteristics and fluid properties of the suspensions.

4.2.1 Solid loading

Table 4.2 shows the amount of solids (LSC) remaining in the suspensions after filtration through a 2 μm borosilicate glass syringe filter. On average, 96.18 % of the solids remained in the AIP suspensions after the filtering step, while 95.32 % remained in the EWD suspensions.

Table 4.2: Solid content of each suspension after filtration through a 2 μm borosilicate glass syringe filter. Determined by evaporation and burnoff of volatile species at 600 °C for two hours. An expanded version can be seen in Table B.2 in the Appendix

Sample	Solid content
AIP series	**[wt%]**
AIP1	**18.61**
AIP2	**18.93**
AIP3	**19.05**
AIP4	**19.42**
AIP5	**19.30**
EWD series	
EWD1	**18.96**
EWD2	**19.33**
EWD3	**18.65**
EWD4	**19.53**
EWD5	**19.69**

4.2.2   Particle size distribution

Plots of the number based particle size distributions (see Section 3.2.3) in the AIP suspensions are given in Figure 4.1, 4.2, 4.3, 4.4 and 4.5. The percentage of particles of a given size (diameter) as well as the cumulative particle size are plotted for both the initial measurement and for the measurement after two days. Six measurements were made in both cases, three before ultrasonication (Pre US) and three after (Post US), see Section 3.2.3 for details.
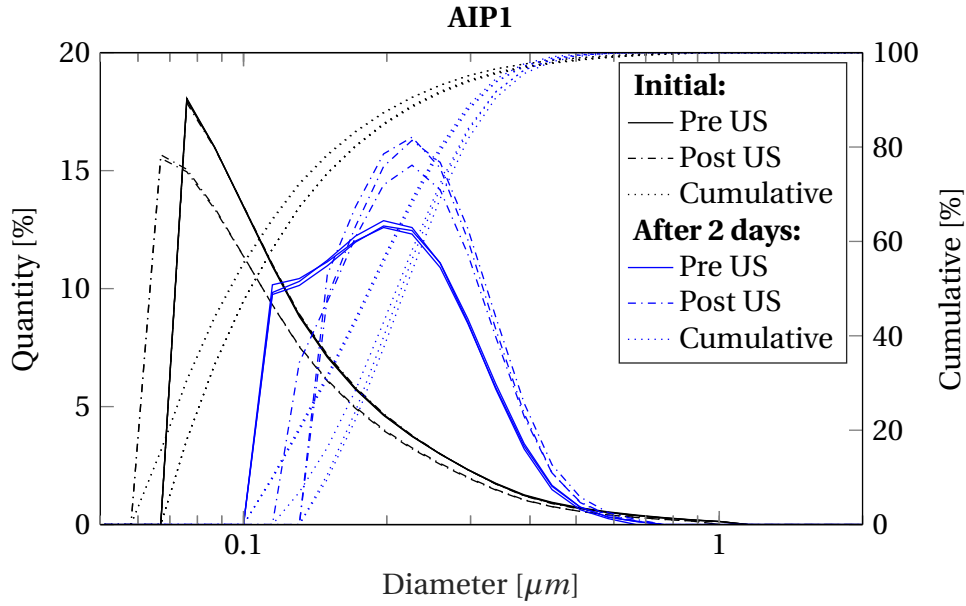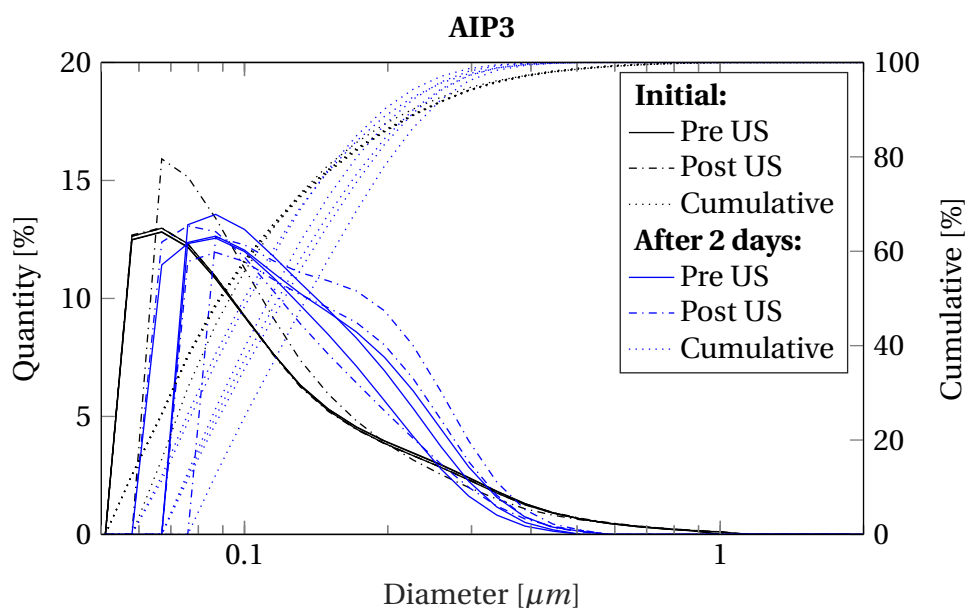

Figure 4.1: Number based particle size distribution (see Sec. 3.2.3) of the AIP1 suspension before and after in-situ ultrasonication (US) in the instrument (Pre US and Post US, respectively) for both the initial measurement and after two days where the suspensions had stood still to allow agglomeration and sedimentation. Solid and dashdotted lines on the primary y-axis, dotted on the secondary y-axis.
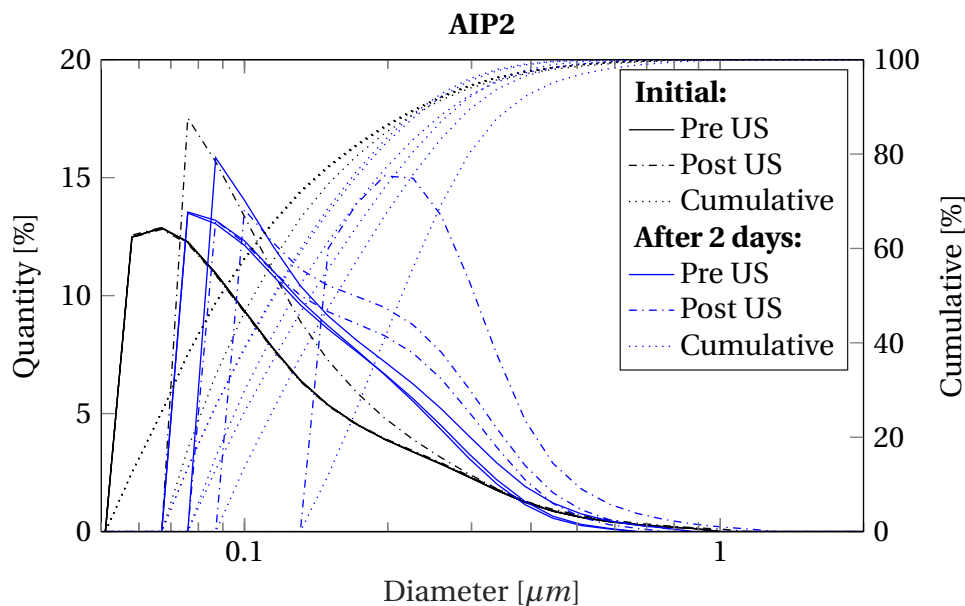
Figure 4.2: Number based particle size distribution (see Sec. 3.2.3) of the AIP2 suspension before and after in-situ ultrasonication (US) in the instrument (Pre US and Post US, respectively) for both the initial measurement and after two days where the suspensions had stood still to allow agglomeration and sedimentation. Solid and dashdotted lines on the primary y-axis, dotted on the secondary y-axis.
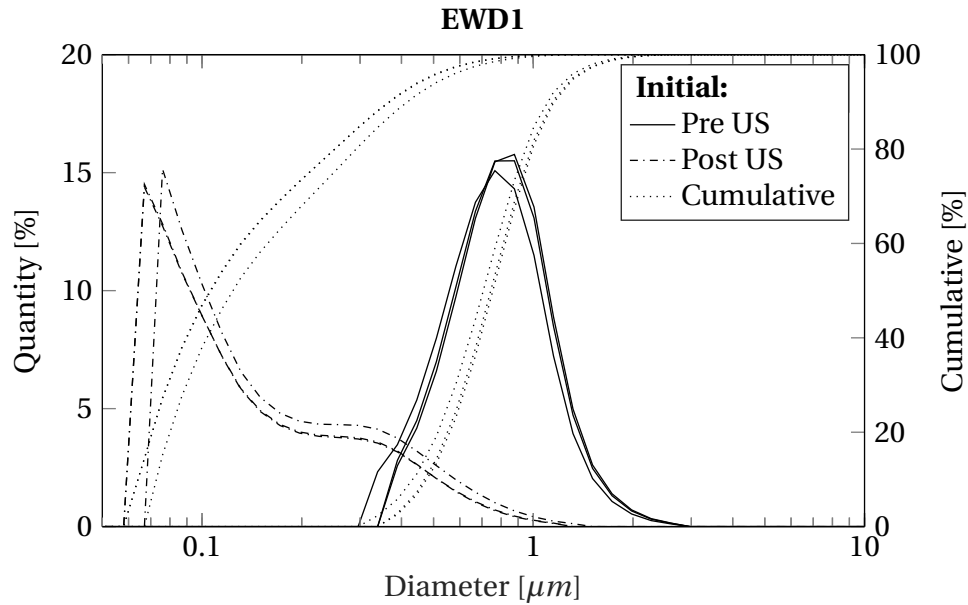

Figure 4.3: Number based particle size distribution (see Sec. 3.2.3) of the AIP3 suspension before and after in-situ ultrasonication (US) in the instrument (Pre US and Post US, respectively) for both the initial measurement and after two days where the suspensions had stood still to allow agglomeration and sedimentation. Solid and dashdotted lines on the primary y-axis, dotted on the secondary y-axis.
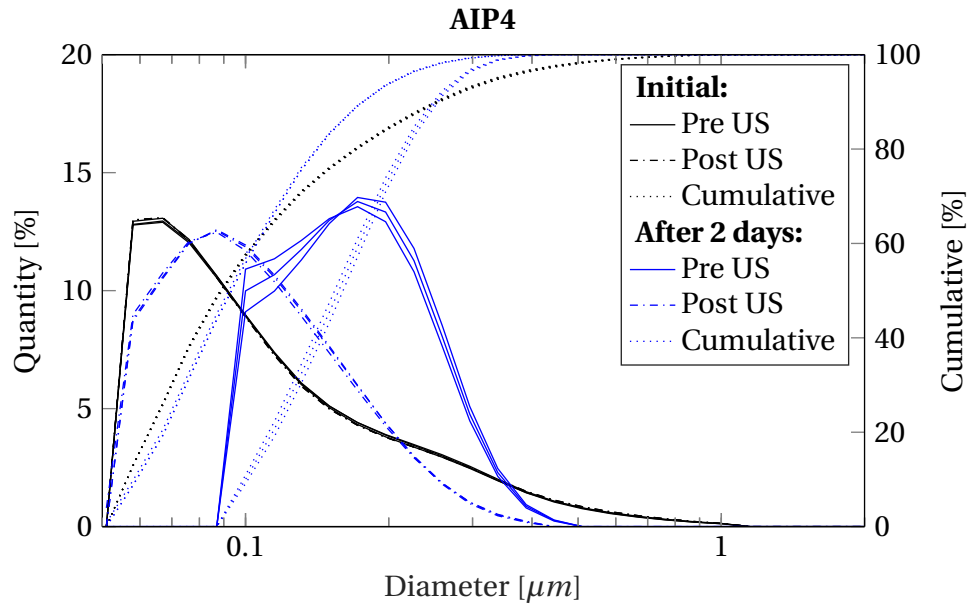
Figure 4.4: Number based particle size distribution (see Sec. 3.2.3) of the AIP4 suspension before and after in-situ ultrasonication (US) in the instrument (Pre US and Post US, respectively) for both the initial measurement and after two days where the suspensions had stood still to allow agglomeration and sedimentation. Solid and dashdotted lines on the primary y-axis, dotted on the secondary y-axis.
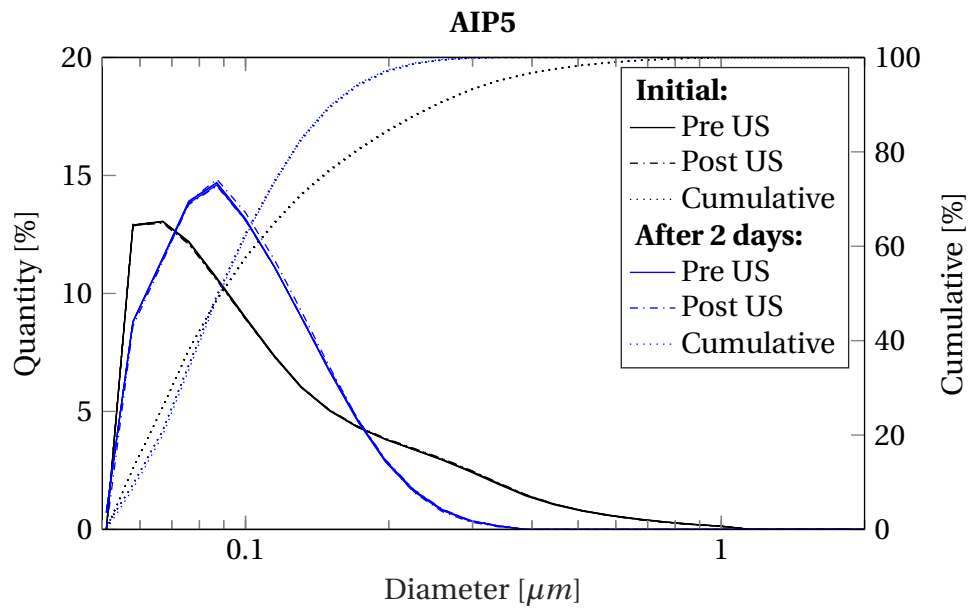
Figure 4.5: Number based particle size distribution (see Sec. 3.2.3) of the AIP5 suspension before and after in-situ ultrasonication (US) in the instrument (Pre US and Post US, respectively) for both the initial measurement and after two days where the suspensions had stood still to allow agglomeration and sedimentation. Solid and dashdotted lines on the primary y-axis, dotted on the secondary y-axis.

Table 4.3 lists three values describing the distribution, the $D_{n,10}$, $D_{n,50}$ and $D_{n,90}$. They describe the size limit that 10, 50 and 90 % of the sampled particles lie below. $D_{n,50}$ is the median particle size. The listed value for a given suspension at a given time (Initial/after two days, Pre/post US) is the value from the suspension with the median $D_{n,50}$ value of the three measurements performed at that stage, rounded to two decimals.
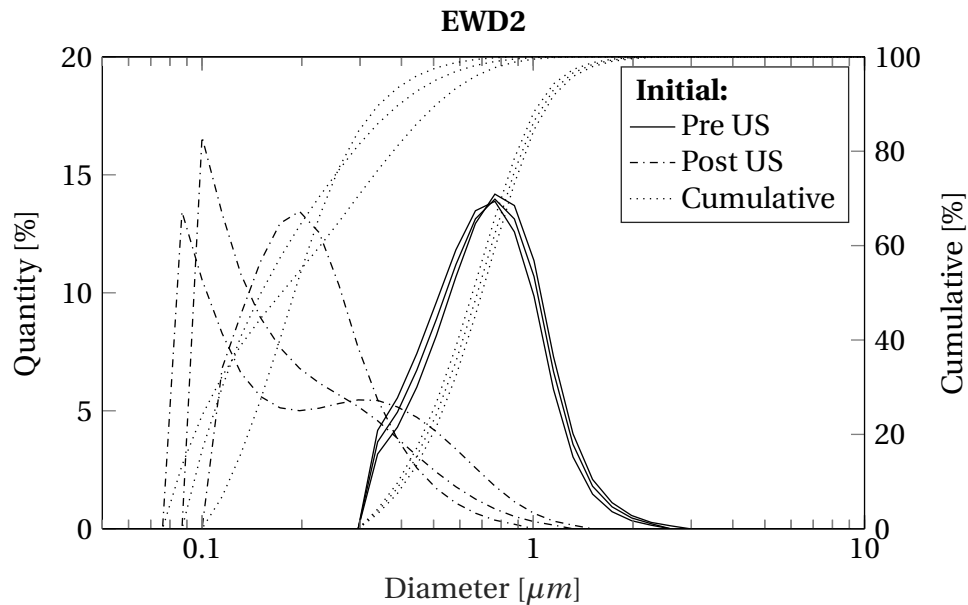
Table 4.3: Particle size distribution of the AIP suspensions before and after in-situ ultrasonication (US) in the instrument (Pre US and Post US, respectively) for both the initial measurement and after two days where the suspensions had stood still to allow agglomeration and sedimentation. $D_{n,50}$ is the median particle size, while $D_{n,10}$ and $D_{n,90}$ describe the size which 10 % and 90 % of the sampled particles lies below, respectively. D_n means that the distribution is number based, see Section 3.2.3.

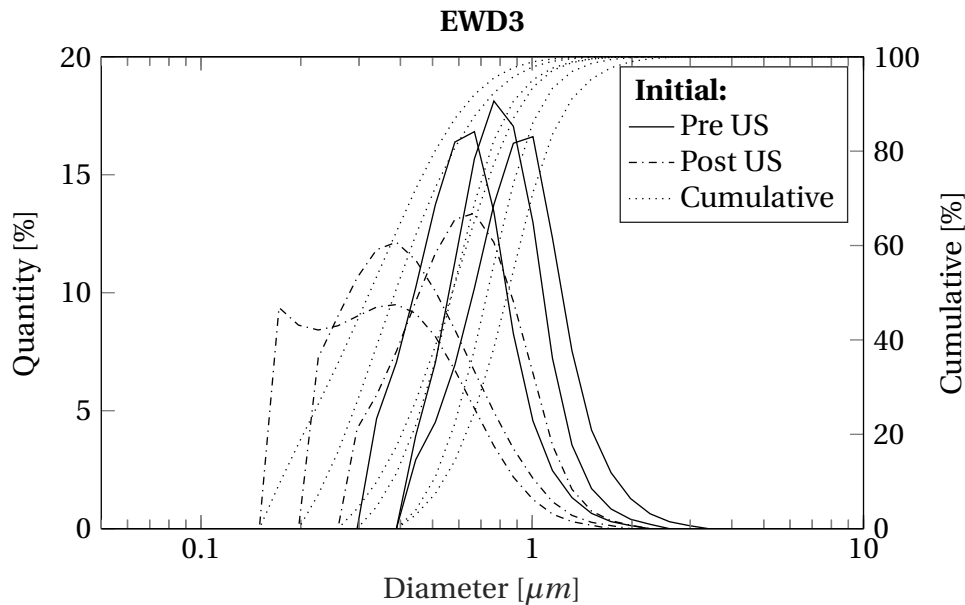| Particle size distribution data						
AIP series	**Pre US**			**Post US**		
Initial	$D_{n,10}$ [µm]	$D_{n,50}$ [µm]	$D_{n,90}$ [µm]	$D_{n,10}$ [µm]	$D_{n,50}$ [µm]	$D_{n,90}$ [µm]
AIP1	0.07	0.10	0.24	0.06	0.09	0.22
AIP2	0.06	0.09	0.23	0.06	0.09	0.24
AIP3	0.06	0.09	0.24	0.06	0.09	0.24
AIP4	0.06	0.09	0.25	0.06	0.09	0.25
AIP5	0.06	0.09	0.25	0.06	0.09	0.25
After two days						
AIP1	0.11	0.18	0.31	0.15	0.21	0.33
AIP2	0.07	0.12	0.24	0.10	0.16	0.30
AIP3	0.07	0.11	0.21	0.07	0.12	0.23
AIP4	0.10	0.16	0.25	0.06	0.09	0.18
AIP5	0.06	0.09	0.15	0.06	0.09	0.15

Figures 4.6, 4.7, 4.8, 4.9 and 4.10 show the particle size distributions from the initial measurement of the EWD suspensions. After two days the powder in the suspensions had almost completely sedimented out and hence no second PSD measurements where done.
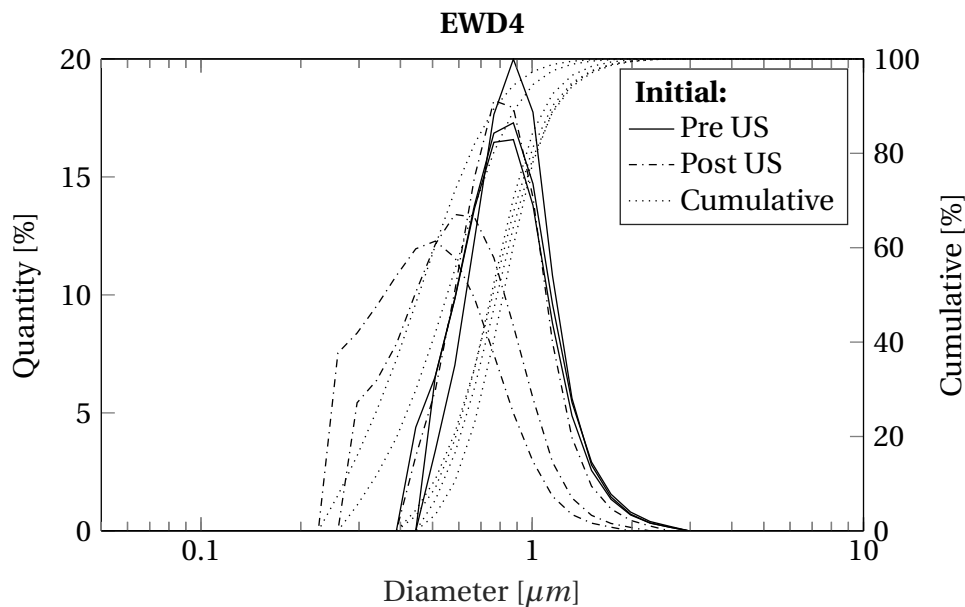
Figure 4.6: Number based particle size distribution (see Sec. 3.2.3) of the EWD1 suspension before and after in-situ ultrasonication (US) in the instrument (Pre US and Post US, respectively) for the initial measurement. Solid and dashdotted lines on the primary y-axis, dotted on the secondary y-axis.
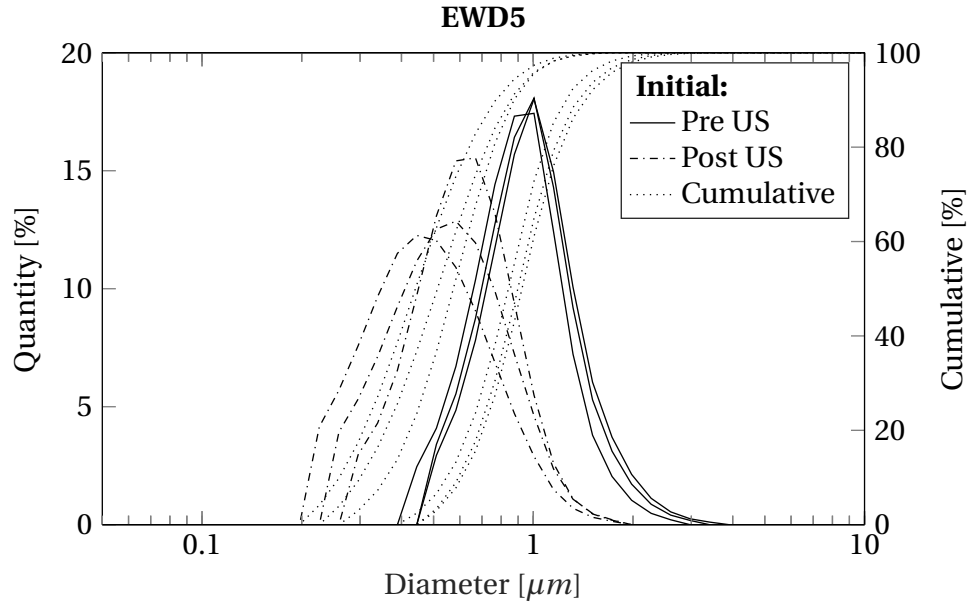

Figure 4.7: Number based particle size distribution (see Sec. 3.2.3) of the EWD2 suspension before and after in-situ ultrasonication (US) in the instrument (Pre US and Post US, respectively) for the initial measurement. Solid and dashdotted lines on the primary y-axis, dotted on the secondary y-axis.

Figure 4.8: Number based particle size distribution (see Sec. 3.2.3) of the EWD3 suspension before and after in-situ ultrasonication (US) in the instrument (Pre US and Post US, respectively) for the initial measurement. Solid and dashdotted lines on the primary y-axis, dotted on the secondary y-axis.

Figure 4.9: Number based particle size distribution (see Sec. 3.2.3) of the EWD4 suspension before and after in-situ ultrasonication (US) in the instrument (Pre US and Post US, respectively) for the initial measurement. Solid and dashdotted lines on the primary y-axis, dotted on the secondary y-axis.

Figure 4.10: Number based particle size distribution (see Sec. 3.2.3) of the EWD5 suspension before and after in-situ ultrasonication (US) in the instrument (Pre US and Post US, respectively) for the initial measurement. Solid and dashdotted lines on the primary y-axis, dotted on the secondary y-axis.

Table 4.4 lists the $\mathbf{D}_{n,10}$, $\mathbf{D}_{n,50}$ and $\mathbf{D}_{n,90}$ from the initial PSD measurement of the EWD suspensions. The values where determined in the same manner as with the AIP suspensions. No representative post ultrasonication PSD data could be collected as the particles agglomerated heavily within the timeframe of the measurements themselves.

Table 4.4: Particle size distribution of the EWD suspensions after one minute of ultrasonication (US) from an ultrasonic tip, prior to in-situ ultrasonication in the instrument (Pre US). $\mathbf{D}_{n,50}$ is the median particle size, while $\mathbf{D}_{n,10}$ and $\mathbf{D}_{n,90}$ describe the size which 10 % and 90 % of the sampled particles lies below, respectively. $\mathbf{D}_n$ means that the distribution is number based, see Section 3.2.3.

Particle size distribution data		
EWD series	**Pre US**	
Initial	$\mathbf{D}_{n,10}$ [μm]	$\mathbf{D}_{n,50}$ [μm]	$\mathbf{D}_{n,90}$ [μm]
EWD1	0.47	0.74	1.12
EWD2	0.40	0.68	1.08
EWD3	0.50	0.73	1.08
EWD4	0.53	0.78	1.19
EWD5	0.59	0.90	1.37

4.2.3 Density

The densities of the suspensions were calculated from the weights and volume obtained using the method explained in Section 3.2.2. The arithmetic mean values for the AIP suspensions are plotted in Figure 4.11 **(a)** and the values for the EWD suspensions in **(b)**, both against additive content to better visualise the uncertainty related to a specific mean and the trend between the suspensions in the series. The values for all suspensions in both series are summarised in Table 4.7.

Prior to the measurements of the suspensions, the calibration of the pipette was investigated through measurements on water. Six measurements were done at 23 °C, resulting in an average density of 0.997 ± 0.001 g/ml. Tabled values for the density of water at 23 °C lists 0.9975 g/ml [50]. Details can be seen in Appendix B.1.3.

(a) AIP series

(b) EWD series
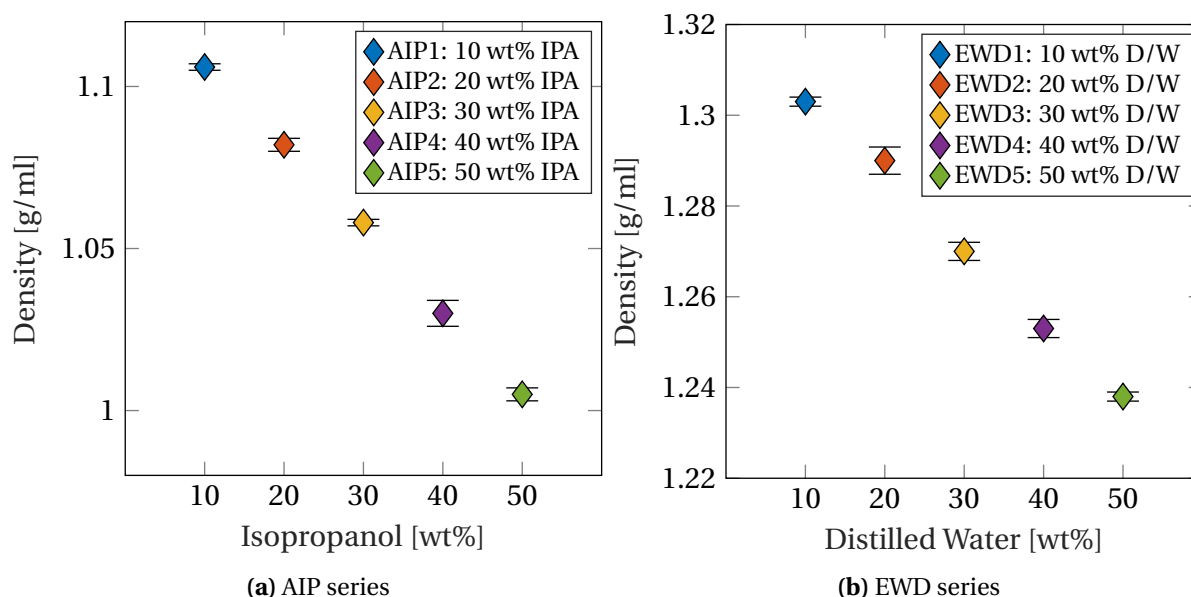
Figure 4.11: (a) Density plotted as a function of isopropanol (IPA) content in the AIP suspensions. **(b)** Density plotted as a function of distilled water (D/W) content in the EWD suspensions. Values are the arithmetic mean of 5-13 measurements per sample at 23 °C and the error bars show ± 1 sample standard deviation.

4.2.4   Viscosity

As can be seen in Figure 4.12 **(a)** and **(b)**, the relationship between the shear stress, τ, and the shear rate, $\dot{\gamma}$, is linear for all suspensions in both the AIP and EWD series. This means that all the measured suspensions behave as Newtonian fluids for the given range of shear rates, as explained in Section 2.3.2.

(a) AIP series   **(b)** EWD series
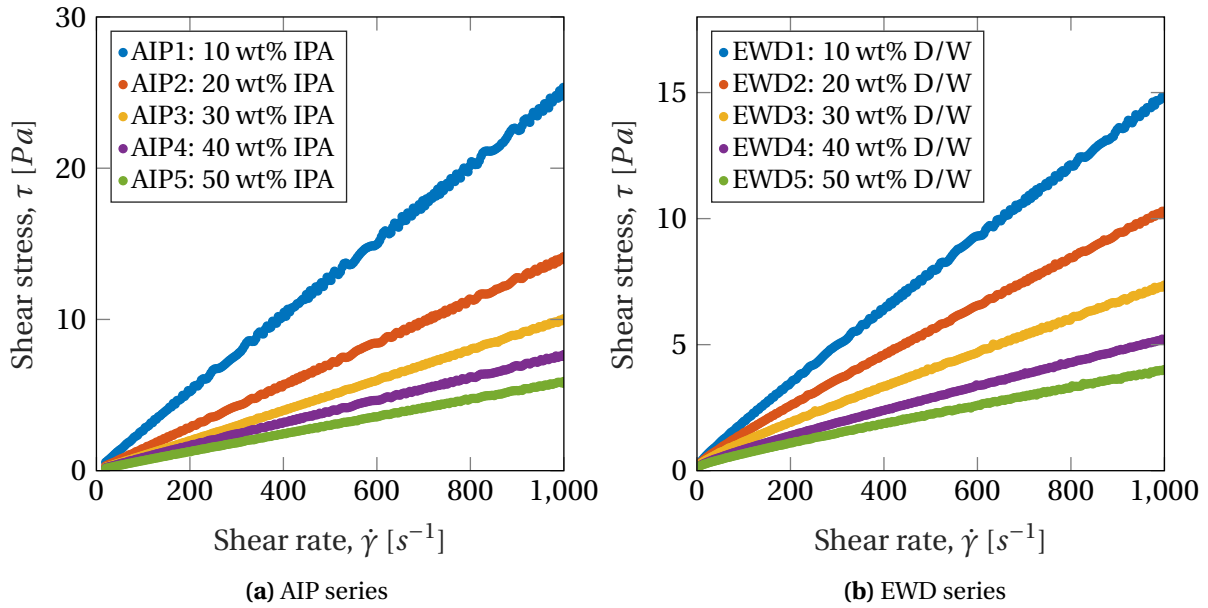
Figure 4.12: Plot showing the shear stress, τ, as a function of the shear rate, $\dot{\gamma}$, for the AIP series **(a)** and the EWD series **(b)**. Measured at 25 °C. A linear relation between τ and $\dot{\gamma}$ implies Newtonian fluid behaviour, see Section 2.3.2.

Figure 4.13 **(a)** and **(b)** presents the viscosity of each suspension of the AIP and EWD series. The values are calculated as arithmetic means from the 15-30 data points collected at a shear rate of $\dot{\gamma} = 1000\,\text{s}^{-1}$, as described in Section 3.2.4, and are plotted as a function of additive content in the suspensions to better show the uncertainties and the trend between the suspensions. Table 4.7 contains a summary of the values. The viscosity of the pure liquid components used in the suspensions are presented in Table 4.5. Both values measured in this work and from literature are given. The viscosity values determined in this work seems to overshoot the literature values by a small amount.

Table 4.5: Viscosity of the liquid components of the suspensions at 25 °C

Sample	Viscosity [mPa*s]	
	Measured	Literature
α-Terpineol	36.77 ± 0.09	-
Isopropanol	2.19 ± 0.01	2.04 [50, p. 6-246]
Ethylene Glycol	17.87 ± 0.08	14.78 [51], 20.9* [52, p. 9]
Water	-	0.890 [50, p. 6-247], 0.8902 [53]

*20 °C

(a) AIP series   **(b)** EWD series
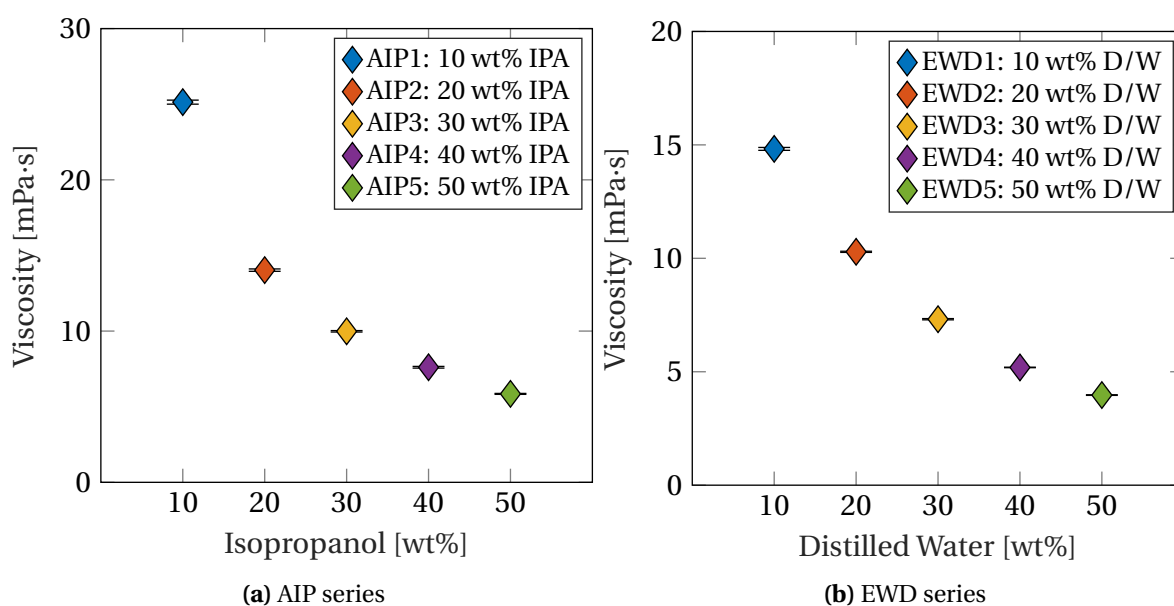
Figure 4.13: (a) Viscosity plotted as a function of isopropanol (IPA) content in the AIP suspensions. **(b)** Viscosity plotted as a function of distilled water (D/W) content in the EWD suspensions. Values are the arithmetic mean of 15-30 measurements per sample at a shear rate of $1000\,\text{s}^{-1}$ at 25 °C and the error bars show ± 1 sample standard deviation.

4.2.5   Surface tension

Figure 4.14 **(a)** and **(b)** contains plots of the surface tension of the AIP and EWD suspensions plotted against the additive content, respectively. The surface tension of the pure liquid components used in the suspensions are presented in Table 4.6. Both values measured in this work and from literature are given. The surface tension values determined in this work seem to agree fairly well with literature values.

Table 4.6: Surface tension of the liquid components of the suspensions

Sample	Surface tension [mN/m]	
	Measured*	Literature**
α-Terpineol	31.45 ± 0.16	-
Isopropanol	21.21 ± 0.12	20.92 [50, p. 6-193]
Ethylene Glycol	45.98 ± 0.56	48.02 [50, p. 6-191]
Distilled Water	71.26 ± 0.27	72.06 [50, p. 6-194], 71.99 [53]

*23 °C **25 °C

(a) AIP series

(b) EWD series
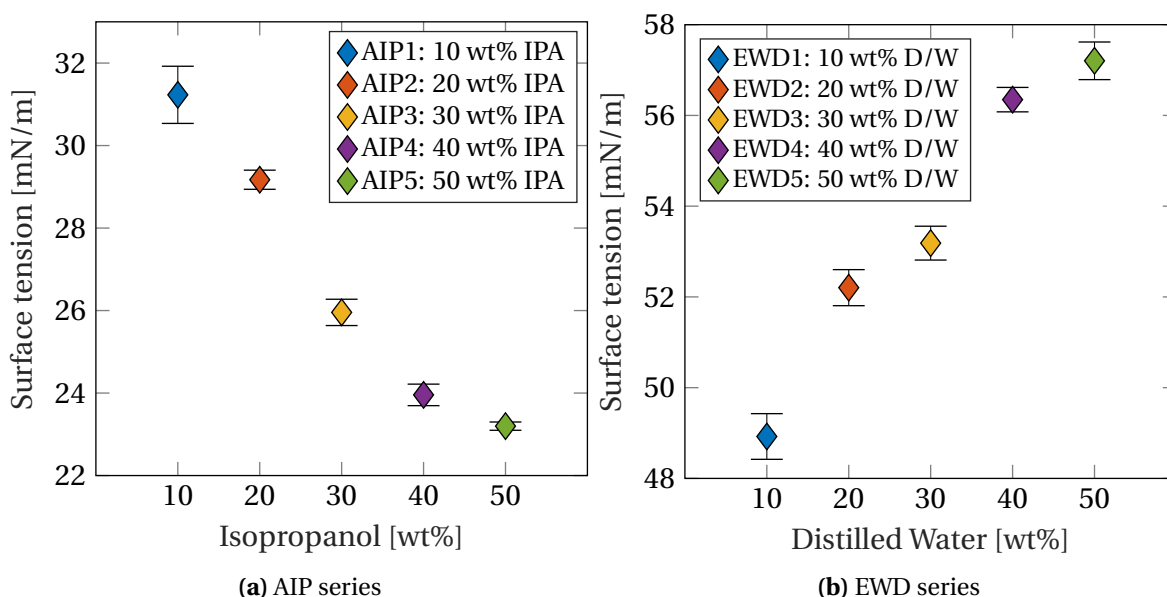
Figure 4.14: **(a)** Surface tension plotted as a function of isopropanol (IPA) content in the AIP suspensions. **(b)** Surface tension plotted as a function of distilled water (D/W) content in the EWD suspensions. Values are the arithmetic mean of >20 measurements per sample at ~23 °C and the error bars show ± 1 sample standard deviation.

4.2.6 Summary of fluid properties

A summary of the fluid properties of each suspension is given in Table 4.7, including uncertainties given as one sample standard deviation.

Table 4.7: Summary of the measured density, viscosity and surface tension of all the suspensions that were made. Uncertainties are given as ± 1 sample standard deviation. Density and surface tension measured at 23 °C, viscosity at 25 °C.

Sample	Density [g/ml]	Viscosity [mPa*s]	Surface tension [mN/m]
AIP series			
AIP1	1.106 ± 0.001	25.14 ± 0.13	31.23 ± 0.69
AIP2	1.082 ± 0.002	14.03 ± 0.08	29.17 ± 0.23
AIP3	1.058 ± 0.001	9.98 ± 0.05	25.96 ± 0.32
AIP4	1.030 ± 0.004	7.61 ± 0.06	23.96 ± 0.26
AIP5	1.005 ± 0.002	5.85 ± 0.03	23.20 ± 0.10
EWD series			
EWD1	1.303 ± 0.001	14.82 ± 0.06	48.92 ± 0.50
EWD2	1.290 ± 0.003	10.29 ± 0.03	52.20 ± 0.40
EWD3	1.270 ± 0.002	7.32 ± 0.03	53.19 ± 0.37
EWD4	1.253 ± 0.002	5.19 ± 0,01	56.35 ± 0.27
EWD5	1.238 ± 0.001	3.97 ± 0.01	57.20 ± 0.41

4.3   Jettability

4.3.1 Z parameter

The Z parameter (reciprocal of the Ohnesorge number) was calculated for each suspension using Equation 2.5, with a nozzle diameter, d, of 21.8 μm and fluid properties as presented in Table 4.7. The results for the AIP suspensions are plotted as a function of isopropanol content in Figure 4.15 **(a)** and for the EWD suspensions as a function of distilled water content in **(b)**. All suspensions lie within the range of $1 \leq Z \leq 10$ that is regarded as a good indication of jettability, see Section 2.3.2.

(a) AIP series   **(b)** EWD series
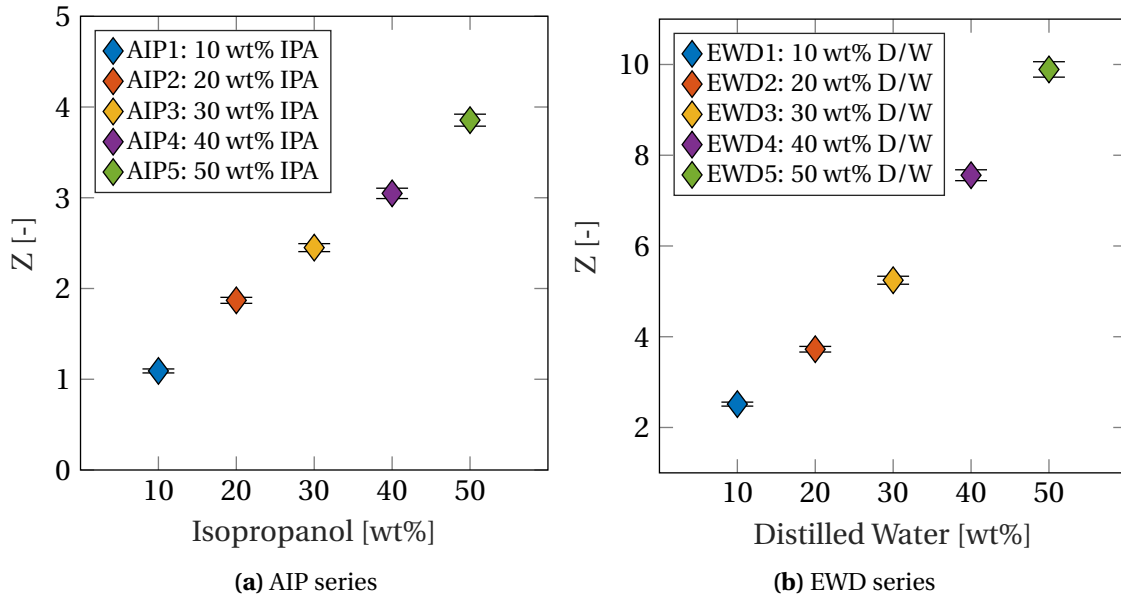
Figure 4.15: (a) The Z parameter (reciprocal of the Ohnesorge number) plotted as a function of isopropanol (IPA) content in the AIP suspensions. **(b)** The Z parameter plotted as a function of distilled water (D/W) content in the EWD suspensions. The error bars show the propagated uncertainty due to the variables' standard deviations, calculated following the rules of the Gaussian error propagation.

4.3.2 Capillary – Weber parameter space

The Capillary and Weber numbers were calculated using Equations 2.6 and 2.7 with the fluid property data summarised in Table 4.7, nozzle diameter, d, of 21.8 µm and different ranges of velocities that was determined by trial and error to make the suspension fit within the jettable area in Capillary–Weber parameter space, as defined by Nallan et al. [2], and explained in Section 2.3.2. The determined velocity ranges are given in Table 4.8. The resulting Ca–We-plot for the AIP suspensions can be seen in Figure 4.16 **(a)**, and for the EWD suspensions in **(b)**.

Table 4.8: Velocity ranges for which the AIP and EWD suspensions fit withing the experimentally determined jettability area of the Capillary–Weber parameter space, defined by Nallan et al. [2]

Sample	Velocity range
AIP series	[m/s]
AIP1	-
AIP2	0.32–4.79
AIP3	0.31–4.99
AIP4	0.31–5.31
AIP5	0.31–5.82
EWD series	
EWD1	0.39–6.28
EWD2	0.41–7.64
EWD3	0.43–7.67
EWD4	0.45–7.56
EWD5	0.46–7.40

(a) AIP series

(b) EWD series
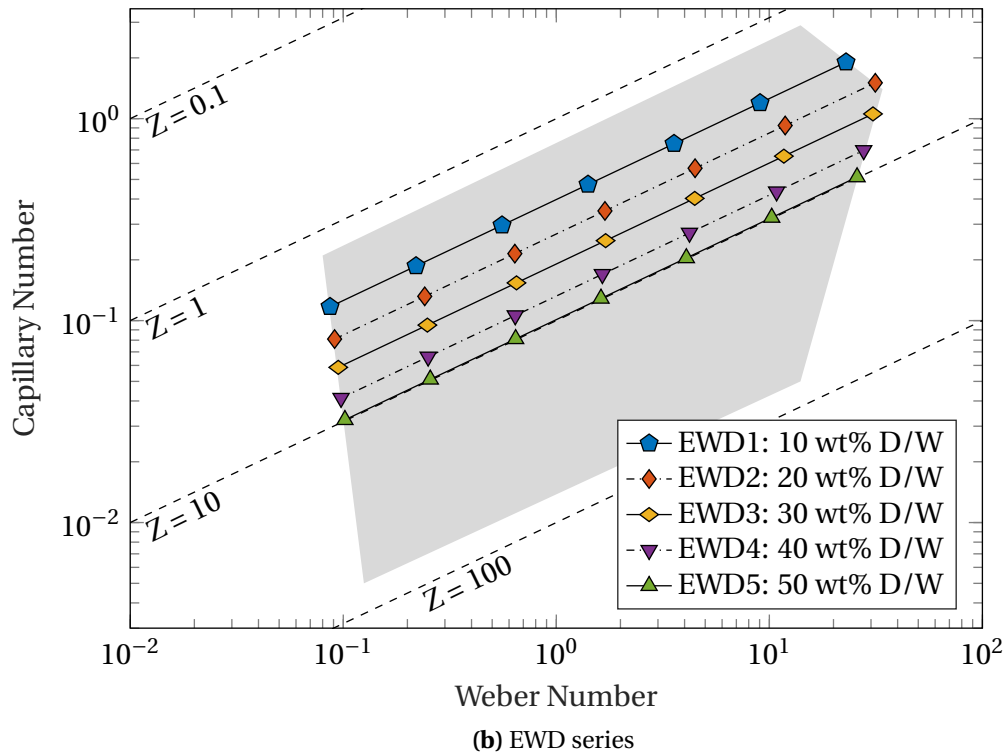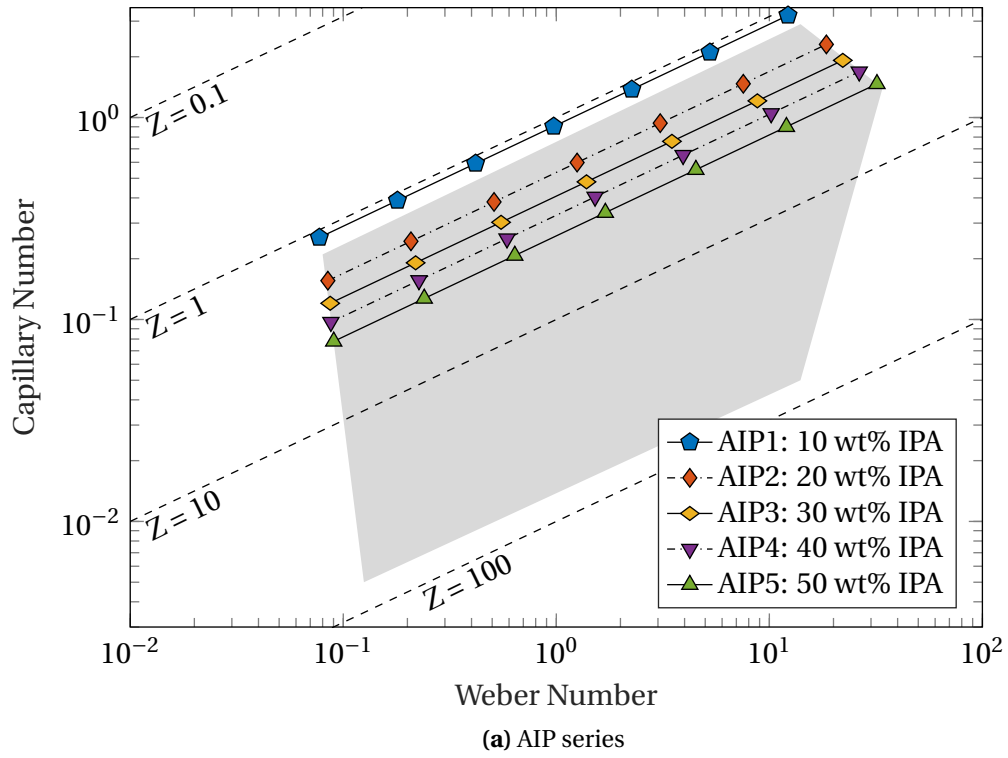
Figure 4.16: AIP **(a)** and EWD **(b)** suspensions plotted inside the jettability window of the Capillary – Weber parameter space, as defined by Nallan et al. [2]. Calculated using Equations 2.6 and 2.7 with the fluid property data summarised in Table 4.7, nozzle diameter, d=21.8 µm and the velocity ranges given in Table 4.8.

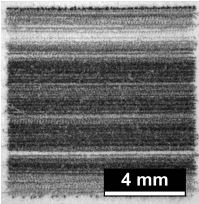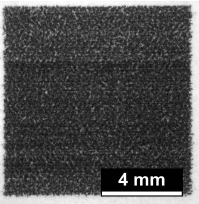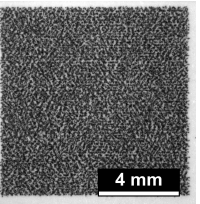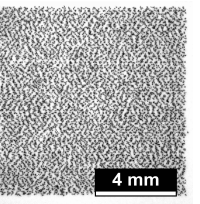### 4.3.3   Weber – Reynolds parameter space

The Weber and Reynolds numbers were calculated using Equations 2.7 and 2.8 with the fluid property data summarised in Table 4.7, nozzle diameter, d, of 21.8 µm and different ranges of velocities that were determined by boundary conditions for the jettable area in Weber–Reynolds parameter space, as defined by Derby [3, 4, 5, 6], explained in Section 2.3.2. The determined velocity ranges are given in Table 4.9. The resulting We–Re-plot for the AIP suspensions can be seen in Figure 4.17 **(a)**, and for the EWD suspensions in **(b)**.

Table 4.9: Velocity ranges for which the AIP and EWD suspensions fit withing the jettability area of the Weber–Reynolds parameter space, defined by Derby [3, 4, 5, 6]

Sample	Velocity range
AIP series	[m/s]
AIP1	2.28–25.59
AIP2	2.22–22.49
AIP3	2.12–20.32
AIP4	2.07–19.01
AIP5	2.06–17.91
EWD series	
EWD1	2.62–25.00
EWD2	2.72–23.99
EWD3	2.77–22.80
EWD4	2.87–22.04
EWD5	2.91–21.11
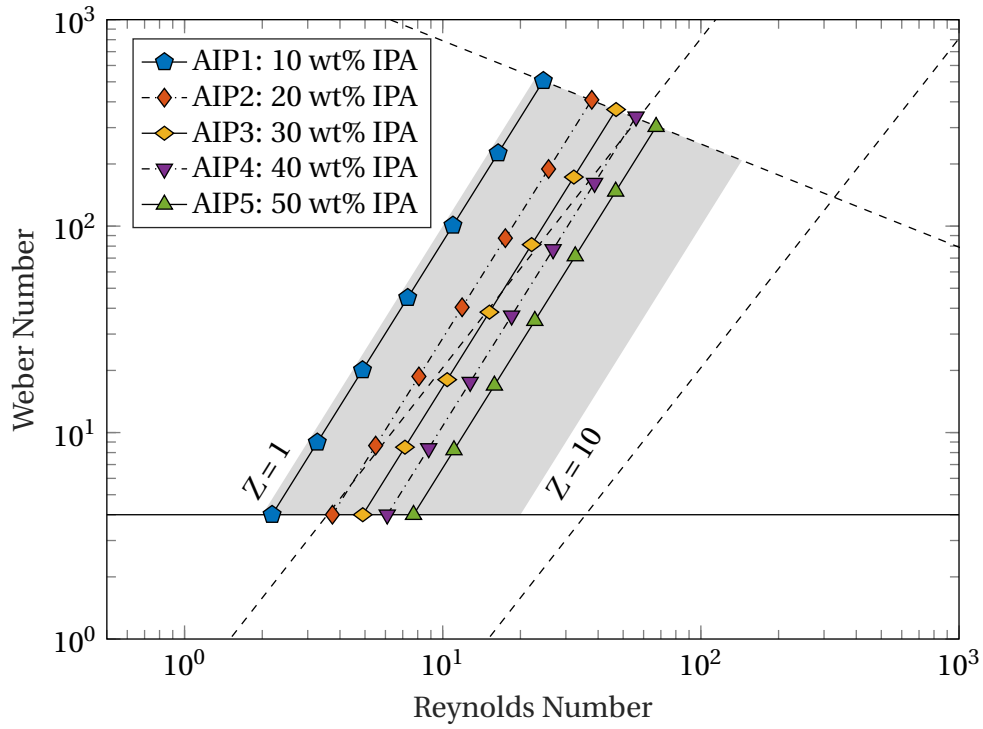
(a) AIP series
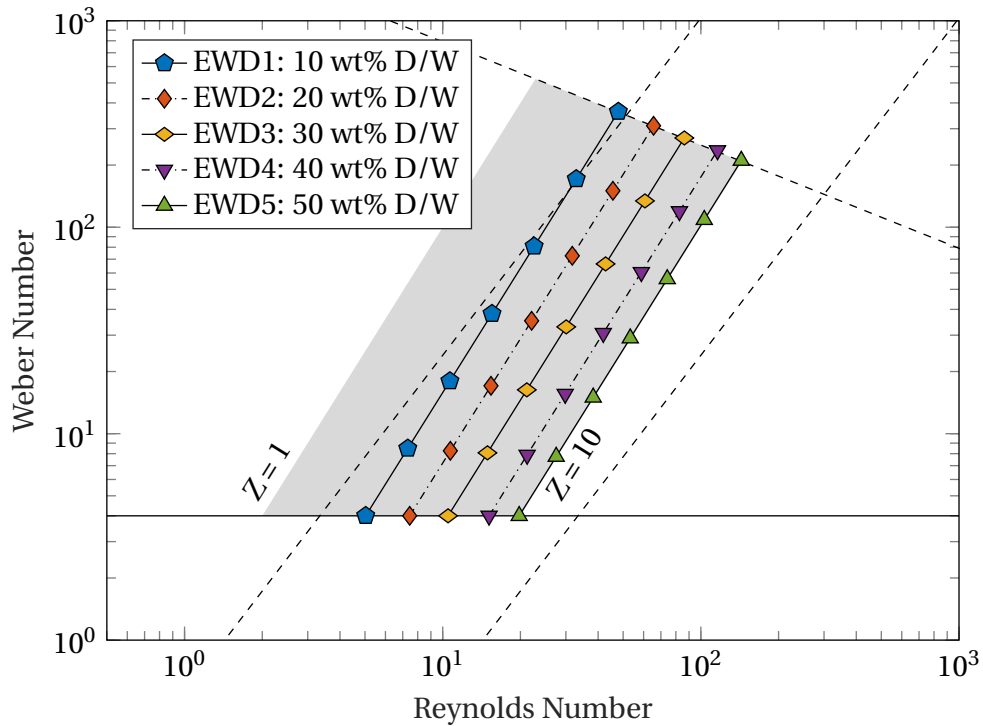
(b) EWD series

Figure 4.17: AIP **(a)** and EWD **(b)** suspensions plotted inside the jettability window of the Weber – Reynolds parameter space, as defined by Derby [3, 4, 5, 6]. Calculated using Equations 2.7 and 2.8 with the fluid property data summarised in Table 4.7, nozzle diameter, d=21.8 μm and the velocity ranges given in Table 4.9.
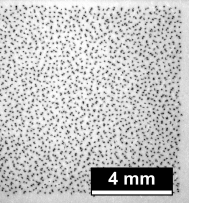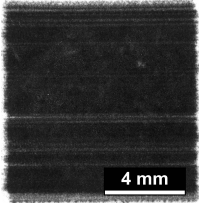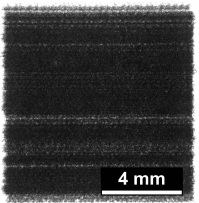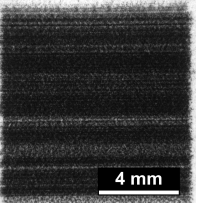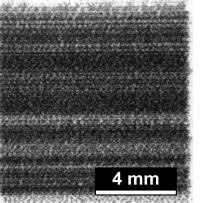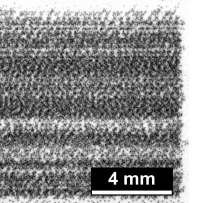
4.4 Evaluation of the suspension printouts
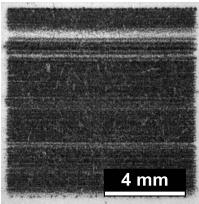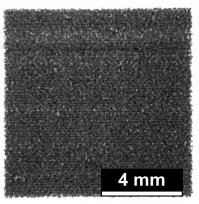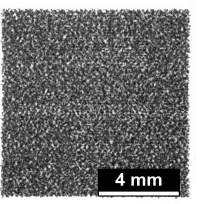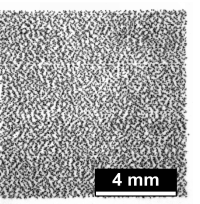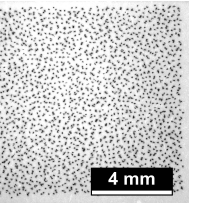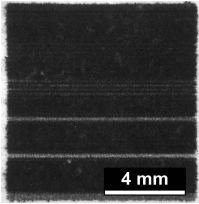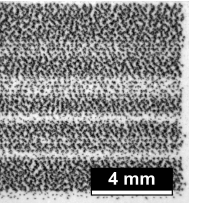
4.4.1 Initial characterisation

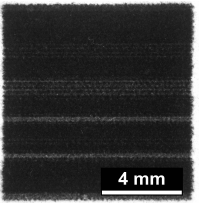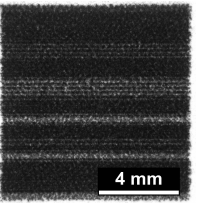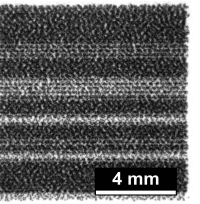Tables 4.10, 4.11, 4.12, 4.13 and 4.14 presents bright field optical microscopy images of the one- and ten-layered printed squares of suspensions AIP3, AIP4, AIP5, EWD1 and EWD4 at a magnification of 8x.
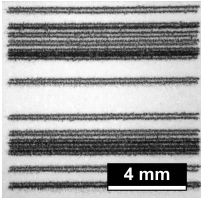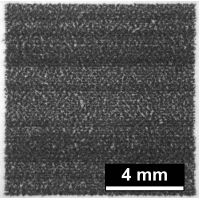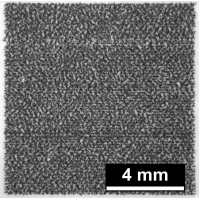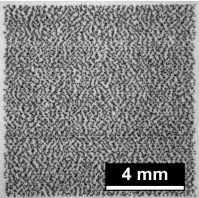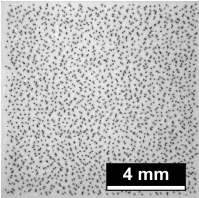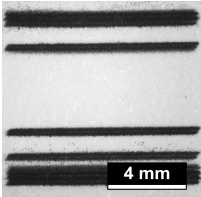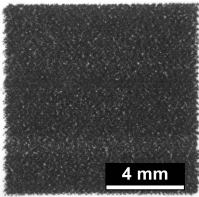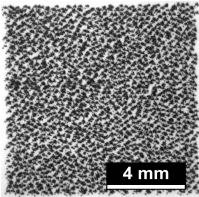
Table 4.10: Bright field optical microscopy images of the AIP3 suspension printed in one and ten layers with transparency values (T) ranging from 0-80 % at 8x magnification
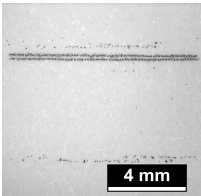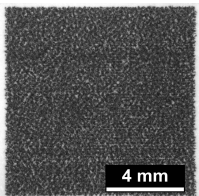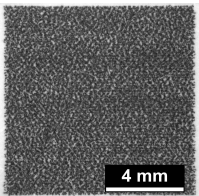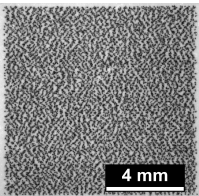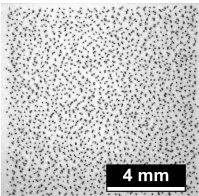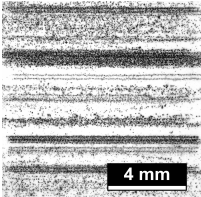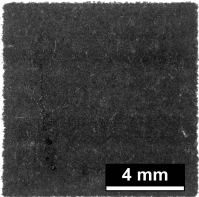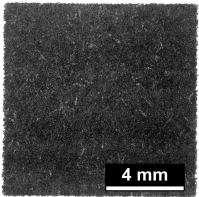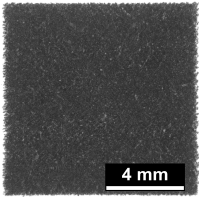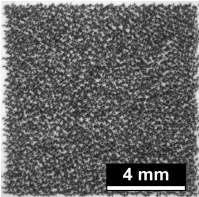
Table 4.11: Bright field optical microscopy images of the AIP4 suspension printed in one and ten layers with transparency values (T) ranging from 0-80 % at 8x magnification
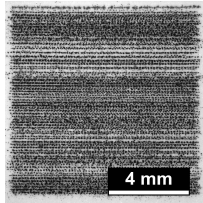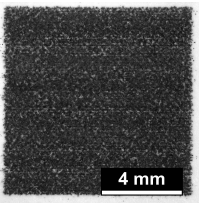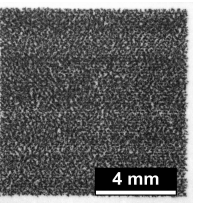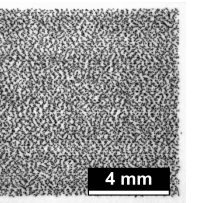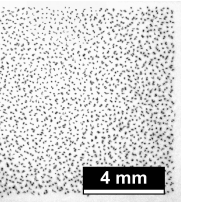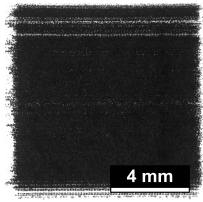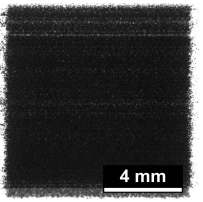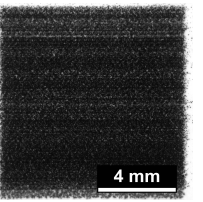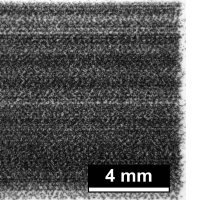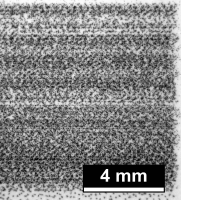
Table 4.12: Bright field optical microscopy images of the AIP5 suspension printed in one and ten layers with transparency values (T) ranging from 0-80 % at 8x magnification. N.B. The ten-layered series was printed after the one- to five-layered were printed for this particular suspension, hence the deviation seen in T-0 1 layer vs T-0 10 layers.

Table 4.13: Bright field optical microscopy images of the EWD1 suspension printed in one and ten layers with transparency values (T) ranging from 0-80 % at 8x magnification
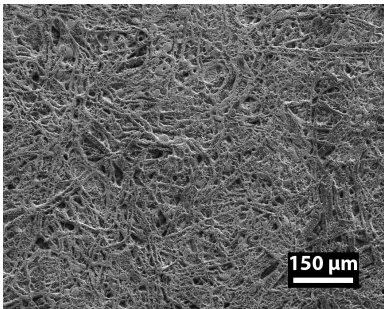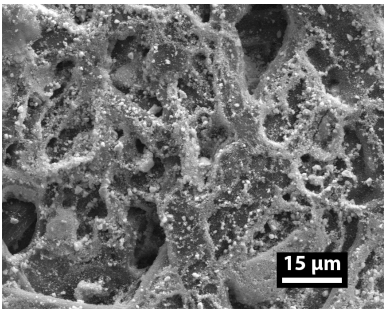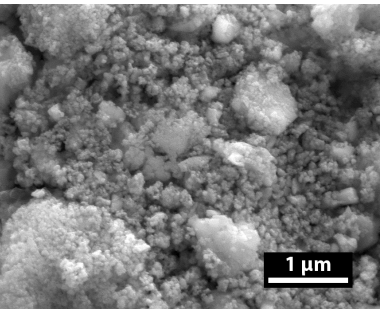
Table 4.14: Bright field optical microscopy images of the EWD4 suspension printed in one and ten layers with transparency values (T) ranging from 0-80 % at 8x magnification

4.4.2 Surface coverage and particle sizes

SEM micrographs of the ten-layered 20 % transparency (T-20) squares of the AIP3, AIP4, EWD1 and EWD4 suspensions, as well as the ten-layered T-0, T-20, and T-40 of the AIP5 suspension are presented in Tables 4.15, 4.16, 4.18, 4.19 and 4.17, respectively. Three micrographs are shown for a 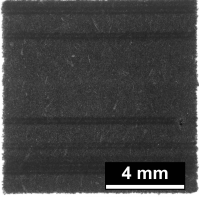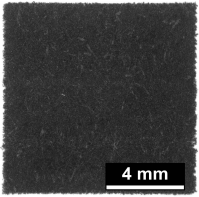given transparency level, with magnifications from left to right of 100x, 1000x, and 20000x. Expanded tables with larger images are given in Appendix F.

Table 4.15: SEM micrographs of the printed AIP3 ten-layered squares with a transparency level of 20 % (T-20) at 100x, 1000x and 20000x magnification from left to right. Centered on the same spot.

Table 4.16: SEM micrographs of the printed AIP4 ten-layered squares with a transparency level of 20 % (T-20) at 100x, 1000x and 20000x magnification from left to right. Centered on the same spot.
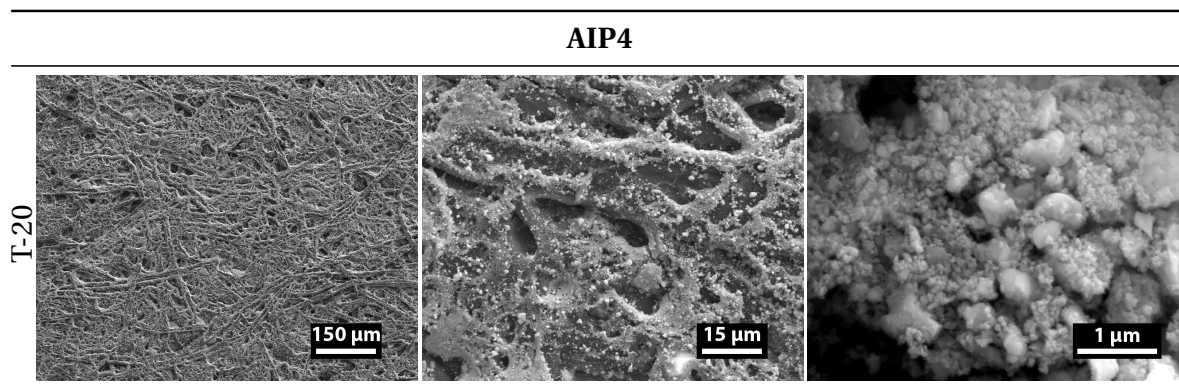
Table 4.17: SEM micrographs of the printed AIP5 ten-layered squares of 0, 20 and 40 % transparency (T-0, T-20 and T-40) at 100x, 1000x and 20000x magnification from left to right. Centered on the same spot.
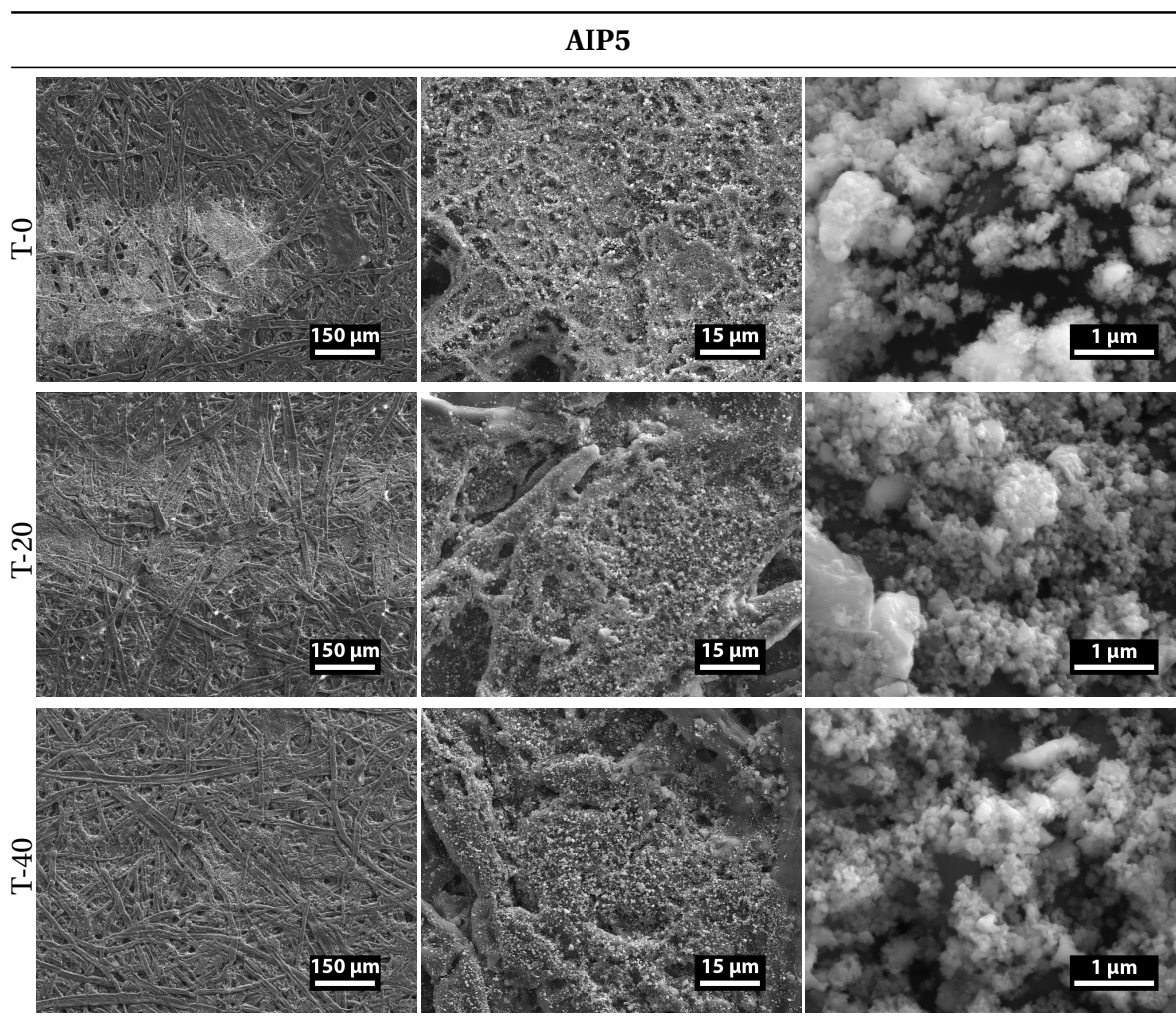
Table 4.18: SEM micrographs of the printed EWD1 ten-layered squares with a transparency level of 20 % (T-20) at 100x, 1000x and 20000x magnification from left to right. Centered on the same spot.
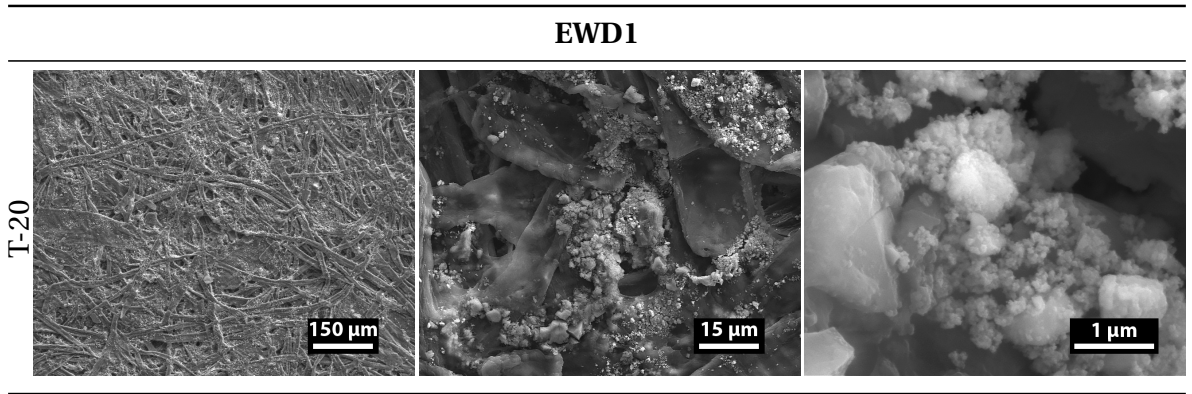
Table 4.19: SEM micrographs of the printed EWD4 ten-layered squares with a transparency level of 20 % (T-20) at 100x, 1000x and 20000x magnification from left to right. Centered on the same spot.
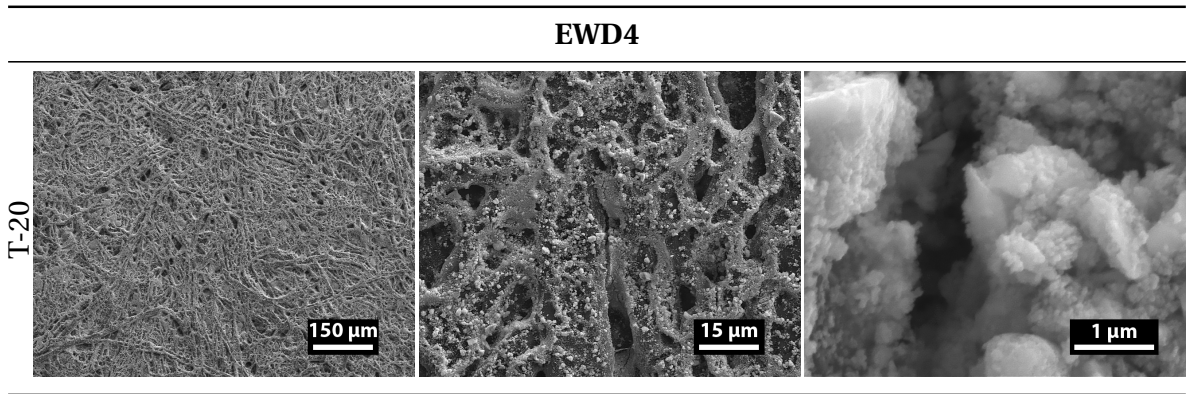
Chapter 5

Discussion

5.1 Evaluation of the suspension-making procedure

Ball milling

It is of interest to investigate the positive and negative aspects of using ball milling as a way to mix the constituents of a suspension, as opposed to rod and ultrasound based mixing. The ball milling step necessitates an extra transfer from the milling bottle to the final container, whilst rod and ultrasound mixing allows the use of only one container from the very weighing of the constituents and to the final mixed suspension is produced. The retrieval rate of each suspension from the ball milling step was therefore of interest, and it was calculated as the percentage of suspension retrieved per weight of all the initially weighed constituents, as shown in Table 4.1. Most suspensions had a retrieval rate of around 95 %, and neither the AIP nor the EWD series show any particular trend. The AIP5 suspension had a rate of retrieval much lower than all the other suspensions. This is possibly due to measurement error or operator hastiness. Indeed persistence is important in the retrieval step, at least to some extent. The amount of suspension adhering to the milling media and bottle walls limits the maximum amount that can be retrieved without the use of additional liquids, but this can not be used without changing the final composition of the suspensions and was therefore avoided. Consistent loss <5 % is deemed possible using this method of ball milling and syringe removal.

The main reason for choosing ball milling over the simpler rod and ultrasound mixing

is because ball milling can break both soft and hard agglomerates and crush the powder particles to smaller sizes than is possible with only rod and ultrasound. A very good mixing is also ensured when milling for a longer period of time. However, the extra cost in both time and loss of suspension from using the milling procedure can be avoided if a powder of satisfactory particle size is used in the first place. This would limit the usefulness of the milling process and rod and ultrasound mixing would in many cases be preferable.

Syringe filtering

The suspensions were filtered through a syringe filter after the milling step to ensure that no single particles with a diameter larger than 2 μm would end up in the final suspension. It is important to keep large particles, especially hard agglomerates, out of the suspensions to prevent blocking of the printer head nozzles during printing. This will be discussed later. SEM analysis done by Rogstad [1] had showed that the powder, as received, had some particles with linear dimensions >5 μm, as can be seen in Figure A.2 **(b)**, substantiating the necessity of filtering. It should be said that since the suspensions were not analysed for the particle sizes between the milling and filtering step, so the effect of each individual step is not known. It is possible that the milling procedure in itself would have been enough to keep all particles sub 2 μm, but even with several kinds of particle size analyses this can not be guaranteed. Using a filter is thus an easy assurance. The mesh size of 2 μm was chosen as a compromise to avoid large losses of solids, whilst removing all particles in the higher size tail of the particle size distribution. In ink-jet printing, no particle diameter should be larger than 1/50'th of the nozzle diameter, preferably below 1/100'th to ensure no clogging [28, 37, 54]. For the printer used in this work, with a nozzle orifice diameter of ~21.8 μm, that means that the particles should be below ~0.44 μm and ideally below ~0.22 μm. It was attempted to filter the suspensions through a 0.2 μm filter, but close to none of the particles made it through the filter, hence a larger one was chosen.

   To investigate just how much of the solids that were removed from each suspension through the milling and filtering steps, a burn-off test was performed, revealing that the solid content in the final suspensions were as listed in Table 4.2. The suspension with the lowest remaining solid loading was the AIP1 suspension, which retained 93.1 % of the ini-

tially added powder through the milling and filtering steps. The average for all ten suspensions were >95 %, indicating that there was not too many particles above 2 µm in diameter in the suspensions to begin with.

5.2 Suspension characteristics

5.2.1 Particle size distribution and stability

Laser diffraction analysis was used to study the particle size distribution in the suspensions. The goal was to obtain the initial particle size distribution and examine how it changed after two days of the suspension standing still. This section will first go through the results from the analyses of the suspensions in the AIP series and then the EWD series.

AIP suspensions

Figures 4.1–4.5 show the raw data from all the number based measurements done on the AIP suspensions. Three lines of one type should be close to overlapping each other for the measurements to be consistent. This is the case for AIP1, AIP4 and AIP5 while AIP2 and AIP3 did not produce fully consistent results, and there is no apparent trend with time for the inconsistent distributions. All measurements show unimodal left-skewed distributions, but the initial measurements of all but the AIP1 sample also show a bulge in the middle of the right side tail. To better analyse the distributions and the evolution over time, the characteristic values $D_{n,10}$, $D_{n,50}$ and $D_{n,90}$ were extracted from the measurement with the median $D_{n,50}$ value, in each of the four cases (Initial: Pre/post US, After two days: Pre/post US) and for each suspension. The median values were chosen over mean values due to the robustness against outliers. Table 4.3 presents all the extracted values. The values are plotted against isopropanol content for all the four measurement cases in Figure 5.1.

Initial measurements

Plot **(a)** and **(b)** show the initial measurements conducted before and after in-situ ultrasonication. In both cases all suspensions have similar distributions with the main body skewed towards the smaller sizes. In-situ ultrasonication did not produce significant changes in

the suspensions **(b)**, indicating that the rod transducer ultrasonication prior to the measurements had broken down the soft agglomerates and that the particles stayed stable until the measurements were conducted. A small decline in overall particle sizes can be seen for the 10 wt% isopropanol sample (AIP1), but the change is so small that it can be due to uncertainty in the measurements and not an actual reduction of the particle sizes.

Measurements after two days

Plot **(c)** shows the resulting distributions after two days of rest, before any ultrasonication was conducted, and **(d)** after in-situ ultrasonication. An analysis of the agglomeration and sedimentation in the different suspensions after these two days will now be conducted. It is important to understand what can and what cannot be read from the graphs in Figure 5.1. By comparing the $D_{n,10}$- and $D_{n,50}$-values for a suspension from the initial measurements after ultrasonication **(b)** to the measurements for that suspension after two days, the extent of agglomeration can be be assessed. The $D_{n,90}$-value is to a greater degree affected by sedimentation processes in the suspension and it is not possible to get the size of the maximally agglomerated particle from these data. The bottom part of the suspension would have to be analysed for that value, while these measurements are from samples taken at the very top of the suspensions. There will be a gradient in sizes between these two extremes. The data presented here can describe the approximate size of the largest stable particle after two days, but since it is not known to which extent larger agglomerates are formed, the quantity of particles that stay stable in the suspension can not be fully described.

To get some knowledge of the extent of sedimentation, the number of drops needed to reach 60-70 % transmittance for the lasers through the dispersed particles in the instrument was noted. It was observed to increase from the initial measurements to the measurements after two days, indicating a lower population of particles in the second case, and thus that sedimentation had occurred. The amount of liquid removed in the measurements are for the record assumed to be so small (a few drops << 0.5 ml) compared to the total volume of the suspension (>20 ml for all but AIP5 (>17.3 ml)) that changes in the composition of the suspension due to the removal are negligible.

No other sedimentation tests were conducted on the suspensions, but Rogstad found in

his previous work that suspensions of 10 wt% LSC suspended in α-Terpineol and PVP, and in isopropanol and PVP, were stable in the sense that a light could not be shined through the upper part of the suspensions even after 44 days [1]. Since the AIP suspensions in this work are mixtures of α-Terpineol and isopropanol with PVP as a stabiliser they are believed to have similar stability, although the higher solid loading probably leads to a higher amount of sedimented particles overall.

By looking at the trend in the $\mathbf{D}_{n,10}$-, $\mathbf{D}_{n,50}$- and $\mathbf{D}_{n,90}$-values of the different suspensions, it is possible to determine how the stability, both when it comes to agglomeration and sedimentation, varies with increasing isopropanol content. The shape of the curve of the data points may give clues as to what fluid property (density, viscosity, surface tension) is the major contributor to stability.

Validity of the results

Before delving into the final analysis, a comment will be given about the validity of the measurements. The $\mathbf{D}_n$-values from the initial measurements (**a** and **b**) are consistent and fairly equal between suspensions, which is expected as all the suspensions were made using the same powder and the same procedure of manufacture. The precision of the presented $\mathbf{D}_n$-values is therefore high. The accuracy of the measurement is harder to determine, but the values seem reasonable given the manufacturing procedure and the observed particle sizes in the SEM images of the printed suspensions (see Section 4.4.2). When it comes to the measurements after two days, the precision of the values is poorer, as is evident from Figures 4.1–4.5. Comparing plot **(c)** to plot **(d)** raises questions about the accuracy of some of the measurements in **(c)**. An increase in particle sizes is observed after the in-situ ultrasonication, contrary to what is expected. The increase seen especially in the 20 and 30 wt% isopropanol suspensions (AIP2, AIP3) is much larger than what is reasonable within the uncertainty of the measurements. The poorer precision of the measurements as compared to especially the AIP4 and AIP5 suspensions and the odd shape of the graph in **(c)** compared to **(d)** also indicate that these measurements do not represent the actual particle size distribution. The results shown in **(d)** are considered the more realistic representations of the real particle size distributions in the suspensions after two days.

Analysis

The overall trends are clear:

There is agglomeration in all suspensions but the extent is reduced with an increase in isopropanol content, as evident by the larger increase in $\mathbf{D}_{n,10}$- and $\mathbf{D}_{n,50}$-values for the samples of lower isopropanol content, and the centering of the $\mathbf{D}_{n,50}$-values between the $\mathbf{D}_{n,10}$ and $\mathbf{D}_{n,90}$ (also due to sedimentation). These results are clearer in Figures 4.1–4.5. This may be due to the higher stability of larger particles in the lower wt% isopropanol suspensions. This leads to an increased chance of Brownian motion moving the smaller particles close enough to larger particles (because of low or slow sedimentation rates) for the van der Waals forces to dominate over the repulsive forces and cause the particles to aggregate, see Section 2.3 on processes affecting stability.

As mentioned, the stability of larger particles decrease with an increasing amount of isopropanol. This can be seen from the reduction of all $\mathbf{D}_n$-values with an increase of isopropanol. The effect of isopropanol content on the extent of agglomeration seems to be smaller than the effect on sedimentation, causing a narrowing of the span of the distribution from the lowest to the highest isopropanol containing suspension (AIP1→AIP5).

The shape of the curves resemble the decrease seen in the viscosity of the suspensions with increased amounts of isopropanol. It is reasonable to assume that the viscosity is the major contributing factor to the change in stability seen when comparing the suspensions in the AIP series to one another.

Initial

(a) Pre US

(b) Post US

After two days

(c) Pre US

(d) Post US
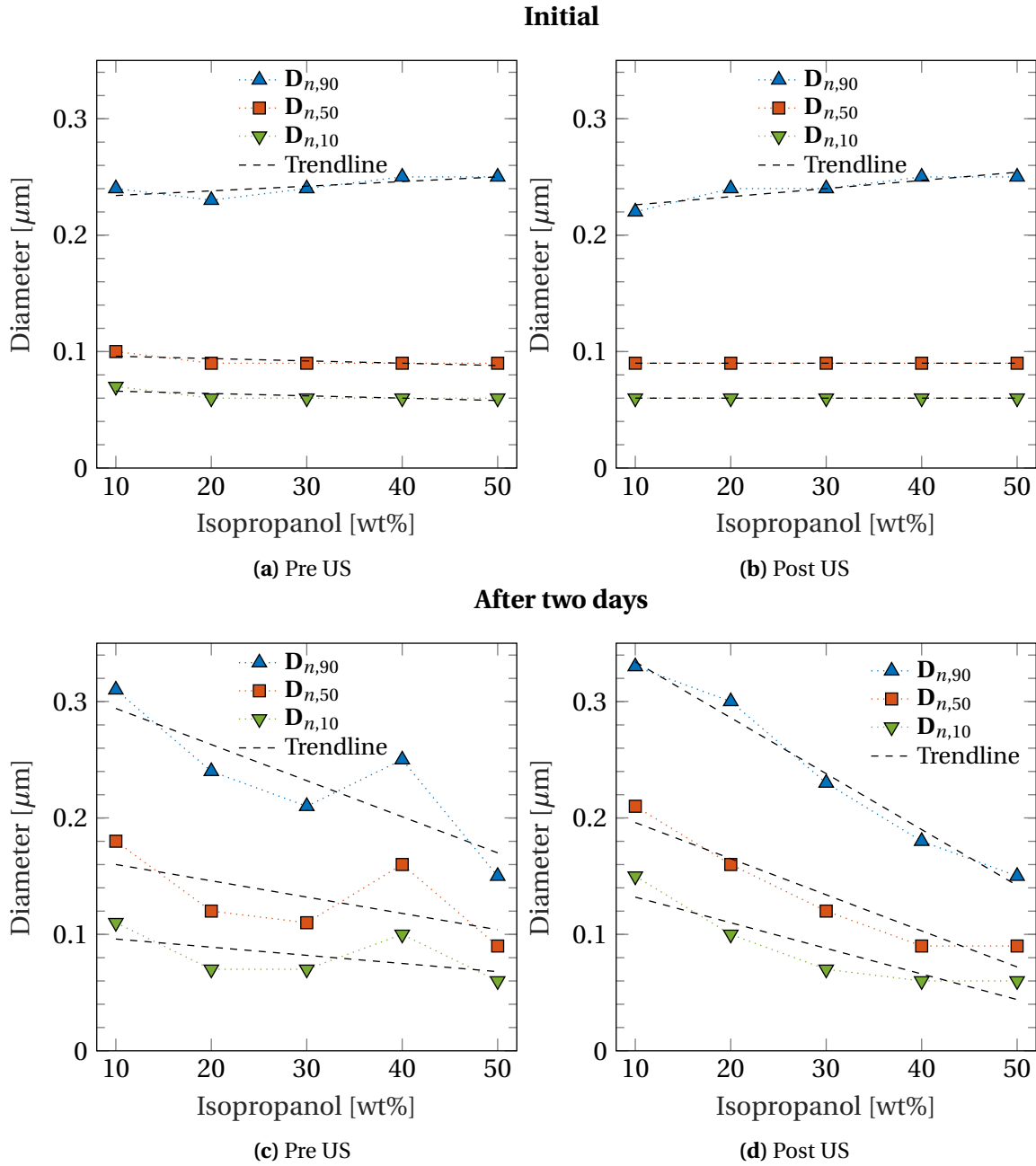
Figure 5.1: PSD data plotted against amount of isopropanol in the AIP suspensions. **(a)** and **(b)**: Initial measurement before and after in-situ ultrasonication. **(c)** and **(d)**: Measurements after two days, before and after in-situ ultrasonication. $D_{n,50}$ is the median particle size, while $D_{n,10}$ and $D_{n,90}$ describe the size which 10 % and 90 % of the sampled particles lies below, respectively. D_n means that the distribution is number based, see Section 3.2.3. Values from Table 4.3. AIP1: 10 wt% isopropanol, AIP2: 20 wt% isopropanol, AIP3: 30 wt% isopropanol, AIP4: 40 wt% isopropanol, AIP5: 50 wt% isopropanol.

EWD suspensions

The ethylene glycol and distilled water based suspensions had almost completely sedimented after the two days of rest and no measurements were done after the initial ones, thus no thorough analysis of these suspensions will be given.

The particle size distributions from the initial measurements are plotted in Figures 4.6-4.10. As can be seen, the precision of the measurements done before in-situ ultrasonication is quite good, while it is very bad for the ones performed after ultrasonication. There is a trend in the shift of the distributions measured after ultrasonication: The first measurement is the one furthest to the left (smaller sizes) for all suspensions and the subsequent measurements, following the steps given in Section 3.2.3, shift towards the right (larger sizes). This means that in less than five minutes after ultrasonication the particles have agglomerated back to the initial size distribution. Since these measurements were performed with isopropanol as the medium in the instrument, it was thought that the Dolapix CE 64 and/or the ethylene glycol adsorbed to the particles was repulsed by isopropanol. New measurements were done in distilled water for the EWD1 suspension to test this hypothesis, but the same trends were seen in those measurements as well.

Because of the heavy and quick agglomeration, no representative median values for the $D_{n,10}$, $D_{n,50}$ and $D_{n,90}$ could be determined, therefore only the values from the measurements before ultrasonication are listed in Table 4.4 and plotted in Figure 5.2.

The rapid agglomeration means that in the few minutes between the rod transducer ultrasonication and the initial measurement before in-situ ultrasonication, the particles had agglomerated back to the thermodynamic equilibrium state of large agglomerates. This is evident when comparing the EWD suspensions in Figure 5.2 to the AIP suspensions in Figure 5.1 **(a)**, where the distributions are both shifted to much smaller particle sizes and are consistent across the ink systems. In that respect, Figure 5.2 is more closely related to Figure 5.1 **(c)**, but without the effects of sedimentation on the larger particles.

The trends that can be seen are: An overall increase in $D_{n,10}$-, $D_{n,50}$- and $D_{n,90}$-values and the distribution span with increasing amounts of distilled water. There does however also seem to be a small reduction in D_n-values and span from the 10 to the 20 wt% distilled water suspensions before the values increase again, and the span increases again after the

30 wt% distilled water suspension. More water means less resistance against agglomeration, but no conclusions can be drawn about the sedimentation from these data. The observations from the two-day rest however indicate a higher sedimentation rate with higher amounts of water.
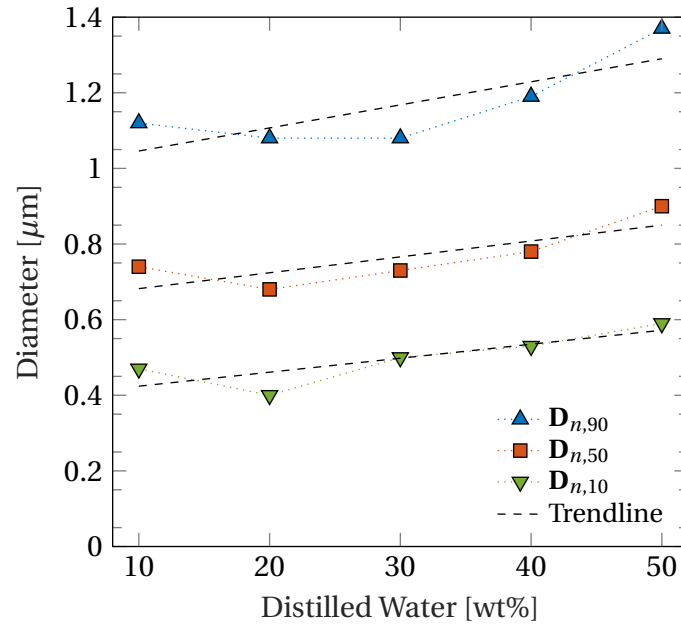
Figure 5.2: PSD data plotted against amount of distilled water in the EWD suspensions. Initial measurement before ultrasonication. $\mathbf{D}_{n,50}$ is the median particle size, while $\mathbf{D}_{n,10}$ and $\mathbf{D}_{n,90}$ describe the size which 10 % and 90 % of the sampled particles lies below, respectively. $\mathbf{D}_n$ means that the distribution is number based, see Section 3.2.3. Values from Table 4.4. EWD1: 10 wt% distilled water, EWD2: 20 wt% distilled water, EWD3: 30 wt% distilled water, EWD4: 40 wt% distilled water, EWD5: 50 wt% distilled water.

Final notes on stability

Some final elaboration on the stability of the AIP suspensions and the instability of the EWD suspensions should be given.

The AIP suspensions display superior stability compared to the EWD suspensions, both when it comes to resisting agglomeration and sedimentation. This implies that PVP is better at stabilising the LSC-particles than the Dolapix CE 64 under the conditions in this work. The stabilising effect occurs when the repulsive forces between two particles are stronger than the attractive forces, as described in Section 2.3.1.

Polyvinylpyrrolidone (PVP) is a neutral polymer that can induce steric stabilisation (see

Figure 2.8) of the solid particles in a suspension by adsorbing onto the surface and masking the van der Waals attraction. However, if the concentration is too small, the polymers may not cover the entire surface and in fact adsorb to multiple particles at the same time, causing bridging between particles, an effect that binds them together like agglomerates. A too high concentration can cause flocculation and deviation from Newtonian fluid behaviour. The amount of PVP used in this work (2 wt% of solid weight) seems to stabilise the particles fairly well, and Newtonian fluid behaviour is maintained, but varying the amount to try to determine the optimal amount should be considered. PVP has been used by several researchers in stabilisation of oxide powder suspensions and as a pore former in ceramic film deposition [55, 56, 57, 58].

Dolapix CE 64 is an anionic polyelectrolyte based on a carboxylic acid with a pH of 9, one that has proven successful in stabilising aqueous suspensions of high solid loading in work by Özkol et al. and Sarraf & Havrda [27, 43]. Özkol et al. stabilised an aqueous suspension with 65 wt% 3Y-TZP and 10 wt% ethylene glycol with the polyelectrolyte. The Dolapix CE 64 is capable of electrosterically stabilising the particles in a suspension, but a successful stabilisation was not accomplished in this work. This may be due to an unfavourable ionic concentration in the suspensions and should be investigated by measuring the zeta-potential of the particles at different pH-values by adding different amounts of the stabiliser and by adjusting the pH with for example HNO_3 and NH_3. A high absolute value for the zeta potential indicates good stability and the pH-value resulting in the highest should be determined [28].

The variation in stability within the AIP series, that has equal amounts of PVP per solid weight, is explained mainly by the difference in viscosity, as a higher viscosity fluid slows the movement of particles more than do a low viscosity fluid.

5.2.2   Fluid properties

Density

The density was calculated from measured mass divided by measured volume rather than calculated based on weighted component densities because it gives a better impression of the real density of the final suspension. Some changes in composition from the initially weighed components will inevitably occur during the production and storage of the suspensions. Several measurements were done for each suspension to reduce the chances of systematic error, and an average density was calculated based on these measurements, the resulting densities are shown in Table 4.7. A large volume of 5.00 ml was used to minimise the uncertainty of the measurements. The Finnpipette F2 that was used has a specified volume inaccuracy of ±0.8% at 5.00 ml [44], resulting in a propagated error of the same size in the calculated density. This is larger than the uncertainty related to the precision of the sampled data points (the sample standard deviation), resulting in a larger overall uncertainty in the density than what the standard deviation suggests. The accuracy of the measurements is considered to be good, as the test on distilled water prior to the measurements proved that the pipette was correctly calibrated (see Section B.1.3 in the Appendix). Accurate density values are important because the density affects the Weber, Reynolds and Ohnesorge numbers directly as well as the Capillary, Weber and Ohnesorge numbers indirectly through the surface tension, which is calculated using the measured density values. This will be briefly discussed where it is of importance.

Viscosity

The precision of the viscosity measurements from the rheometer are completely governed by the rheometer itself, and as shown in Table 4.7 the related sample standard deviations are extremely small. The accuracy of the measurements can to some extent be evaluated by the difference between the measured viscosity and the literature values found for the pure liquids, as presented in Table 4.5. As earlier mentioned, the measured values are a little higher than the literature values, but there are several reasons why these values may deviate from each other. The measurement geometry used in the rheometer may be different or a different instrument may have been used altogether to obtain the literature values. Also,

the chemicals were most likely not produced by the same manufacturer and to the exact same specifications. Considering these uncertainties, the measured viscosity values are considered to be accurate for the fluids used in this work.

The shape of the graphs in Figures 4.13 **(a)** and **(b)** show non-linear decrease in viscosity with an increased amount of additive, with no deviations from the expected curve. No attempt was made at fitting a mathematical expression to the measured values in this work.

Surface tension

The measured surface tension values and the sample standard deviations are given in Table 4.7. The precision of the measurements is generally good, with standard deviations below 0.7 mN/m. The uncertainty of the measured values are as earlier mentioned also affected by the uncertainty of the measured densities, as can be seen from Equation 3.5. Because of the linear relation between density and surface tension, the largest uncertainty in the density values, due to the inherent volume inaccuracy of the pipette of 0.8 %, will lead to a propagated error in the surface tension values of 0.8 %. In the case of the highest measured surface tension of 57.20 mN/m, in suspension EWD5, this amounts to 0.46 mN/m. This is in the same magnitude as the standard deviation of the measurements (0.41 mN/m for EWD5), and is therefore acceptable.

The accuracy of the measurements can be evaluated by comparing the measured values for the pure liquids to literature values, listed in Table 4.6. Since the measurements were done at a slightly lower temperature than what the literature values are stated for, a slightly higher surface tension is expected for the measured values. This holds true for the isopropanol measurements but not for the others which show a lower value, but also a greater standard deviation. By the same arguments about the specification of chemicals used in relation to the viscosity measurements, the results are considered to be trustworthy. Considering the specified uncertainties and the comparison of measured values with literature values for the pure liquids, the accuracy of the measurements on the suspensions is deemed acceptable.

5.3 Evaluation of jettability criteria and ink performance

5.3.1 Jettability criteria

Z **parameter**

The Z parameters and the propagated errors due to the standard deviation have been displayed for both series of suspensions for a nozzle diameter of 21.8 μm in Figure 4.15. All lie within the range of $1 \leq Z \leq 10$ that is widely regarded as a good indicator of jettability (see Section 2.3.2). The uncertainties in the Z parameters are probably somewhat higher than what the propagated standard deviation suggests. This is both because of the volume related error in the density measurements and surface tension, and also because of the slight differences in temperature at which the density, viscosity and surface tension was measured (23 °C for the density and surface tension and 25 °C for viscosity), as these are all temperature dependent properties. The uncertainties are however not considered to stretch beyond the jettable range as the range of jettability is not considered a definitive one. Different studies have found jettable inks with both higher and lower Z parameters than 1 and 10 (see Table 2.5). All the manufactured suspensions in this work is thus considered with certainty to be within the range of Z parameters that *indicate* jettability for the nozzle diameter of the printer used.

The Z parameter can be used to investigate for which sizes of nozzle diameter the suspensions would be indicated jettable. Figure 5.3 shows plots of the Z parameter against typical sizes for nozzle diameters. All the AIP suspensions **(a)** remain within the range of jettablility for nozzle sizes of 10 to 100 μm except AIP1 which falls below for nozzles smaller than 20 μm. The EWD suspensions are more heavily influenced by the change in nozzle diameter and only EWD1 and EWD2 manage to stay within the bounds for the whole range.

(a) AIP series

(b) EWD series
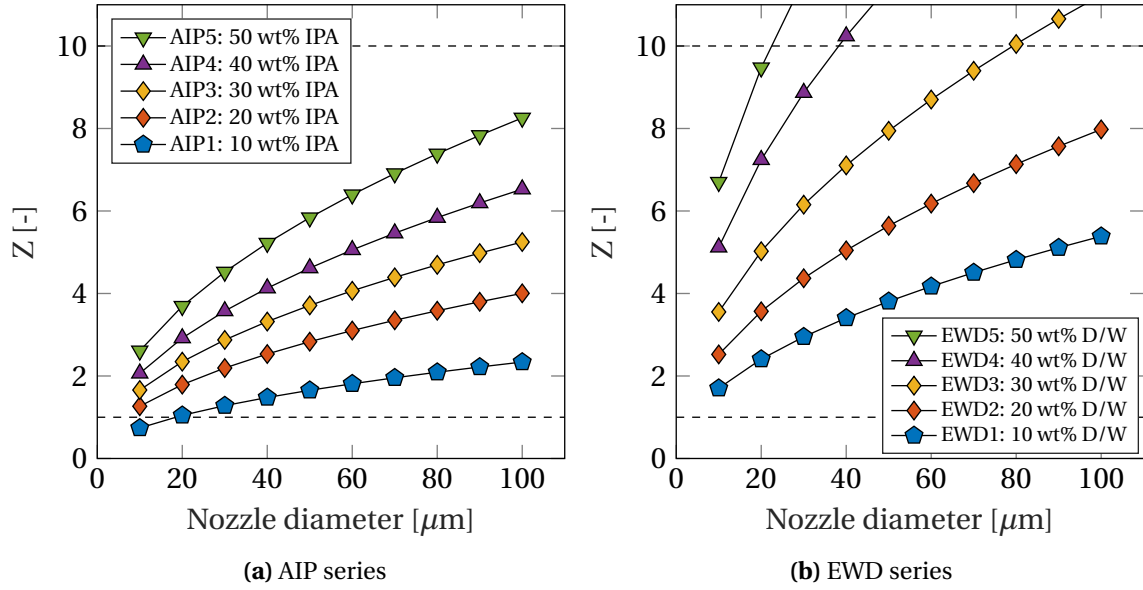
Figure 5.3: The Z parameter (reciprocal of the Ohnesorge number) plotted as a function of nozzle diameter for typical nozzle sizes. **(a)** AIP suspensions and the **(b)** EWD suspensions. Dashed lines mark the upper and lower boundary of the Z parameter values that are considered indicative of jettability.

Capillary–Weber parameter space

The Ca–We parameter space defined by Nallan et al. [2] includes the familiar Z parameter, but also allows evaluation of which printer settings that will work best for a given suspension and nozzle size to achieve single drop formation (jettability). This is due to the velocity of the ink out of the nozzle being a factor in the Capillary and Weber numbers, as seen in Equations 2.6 and 2.7, while the Z parameter is independent of velocity. The velocity out of the nozzle is directly related to the amplitude and pulse duration of the voltage applied to the piezoelectric film in the nozzle chamber [59], and thus a target velocity can help determine which actuation pulse that will work with a given ink.

A small comment should be given on the range of Z parameter values encompassed by the jettable area in the Ca–We parameter space. The jettable area spans Z values from a little above 1 and all the way up to around 60. This is more in accord with what was found by Tai et al. [34] than the small range of 1-10 that many researchers use as a rule of thumb (see Section 2.3.2). There should according to the Ca–We jettability criterion thus be a larger chance of successful drop ejection for suspensions with a Z value larger than 10 than for

the those under 1. Translated to the suspensions in this work, EWD5 should have a greater chance of being jettable than AIP1, which is not evident when looking at the $1 \leq Z \leq 10$ range as marked in Figures 4.15 and 5.3.

An attempt was made to fit the suspensions made in this work inside the jettable area as seen in Figure 4.16 **(a)** and **(b)**. Only suspension AIP1 did not fit within the area. One perk of the Ca–We parameter space is that if a suspension is situated above or below the defined jettable area, it will stay outside for all velocities. The individual suspensions lie along parallel lines, operating at different velocities along the line and with more viscous systems higher up on the Ca number axis.

The velocity ranges that were found to fit the other nine suspensions within the area are listed in Table 4.8. The stated velocities are the ones that made the suspensions fit neatly to the edge of the shaded area, but it should be remembered that the area is not exact but merely an area fitted around data from experiments on pure liquids and binary mixtures, as seen in Figure 2.12. As such, the closer to the edge of the area a suspension is situated, the higher the uncertainty for its jettability, and the more care must be taken when drawing conclusions.

Weber–Reynolds parameter space

The We–Re parameter space defined by Derby [3, 4, 5, 6] also incorporates the Z parameter while giving information about the velocity ranges the suspensions should be jettable for. Derby defined this jettability criterion long before Nallan et al. defined theirs, and the We–Re parameter space has naturally been used by more researchers as a jettability-criterion than has the Ca–We, amongst others by Esposito et al. [55] who modified the right and left boundary to encompass Z-values of 4-14 instead of the original 1-10.

In the We–Re parameter space, the area is not defined by fitting it around experimental data, but by defining a jettable regime in Z, a minimum We value for drop ejection, and a maximum speed where the ejected droplet does not splash on impact with the substrate, following the relation in Equation 2.10. The We–Re parameter space does not normalise the effect of the surface tension, as the Ca–We parameter space does, meaning that the surface tension has a greater impact on the jettability according to this criterion.

The suspensions in this work were fitted according to the limits defined by Derby and plotted in Figure 4.17 with the velocity values in Table 4.9. Even though the limits to the We–Re jettable area are more strictly defined than for the Ca–We area, these limits are still defined by experiments done on certain types of suspensions and are not necessarily applicable to the suspensions and printing conditions in this work. The same caution should therefore be taken in using values near the boundaries to draw conclusions as in the Ca–We parameter space.

When comparing the velocity ranges for supposedly jettable printing conditions from the Ca–We and We–Re parameter spaces, large differences can be seen. While the Ca–We area suggests velocities from approximately 0.3 to below 8 m/s for the AIP suspensions and EWD suspensions, the We–Re parameter space suggests values from approximately 2-25 m/s. The ranges overlap somewhat, but the We–Re parameter space suggests far greater velocities are allowed while maintaining stable drop formation and avoiding splashing. The reason for this is the definition of the top boundary in the We–Re parameter space, which Derby references to work done by Bhola and Chandra [41]. Investigation of this source shows that their research was conducted on molten wax droplets with impact velocities of 0.5-2.7 m/s on heated substrates, which is a scenario far from what is conducted in this work. This sows doubt about the accuracy of the top boundary and hence the velocity ranges determined from the We–Re parameter space. Typical velocities in ink-jet printing are however in the range of 1 to 30 m/s, according to Esposito [55], while other research uses velocities below 10 m/s [59]. It is hard to draw a conclusion as to which velocity range is more realistic, but the Ca–We space seems more trustworthy in this case.

5.3.2 Performance of the printed suspensions

Initial considerations

Due to equipment failure, attempts were not made to print all of the ten suspensions that were made. The suspensions that were printed are: AIP3, AIP4, AIP5, EWD1 and EWD4 (see Table 3.3 for compositions). The suspensions span a fairly large range in Z parameter values and areas in the Ca–We and We–Re parameter spaces while remaining inside the boundaries of jettability in all cases, and spanning two chemically very different ink

systems. The printed suspensions from both the AIP and the EWD series are re-plotted together in the Ca–We and We–Re parameter spaces in Figures 5.4 and 5.5 for easier comparison.

As can be seen by the overlap in both Ca–We and We–Re parameter space, the 30 wt% isopropanol, α-Terpineol based suspension (AIP3) and the 10 wt% distilled water, ethylene glycol based suspension (EWD1) have almost identical fluid properties, but the EWD1 should be jettable for higher velocities than the AIP3 suspension. The rest of the suspensions follow at higher Z-values due mostly to lower viscosities.

According to the jettability criteria, all the suspensions were expected to be jettable within realistic velocities. The printer used in this research did however not offer direct control over the printing parameters and consequently the velocity. No optical instruments were available to analyse the jetting from the nozzle either, and therefore no thorough analysis of jet breakup phenomena could be accomplished.
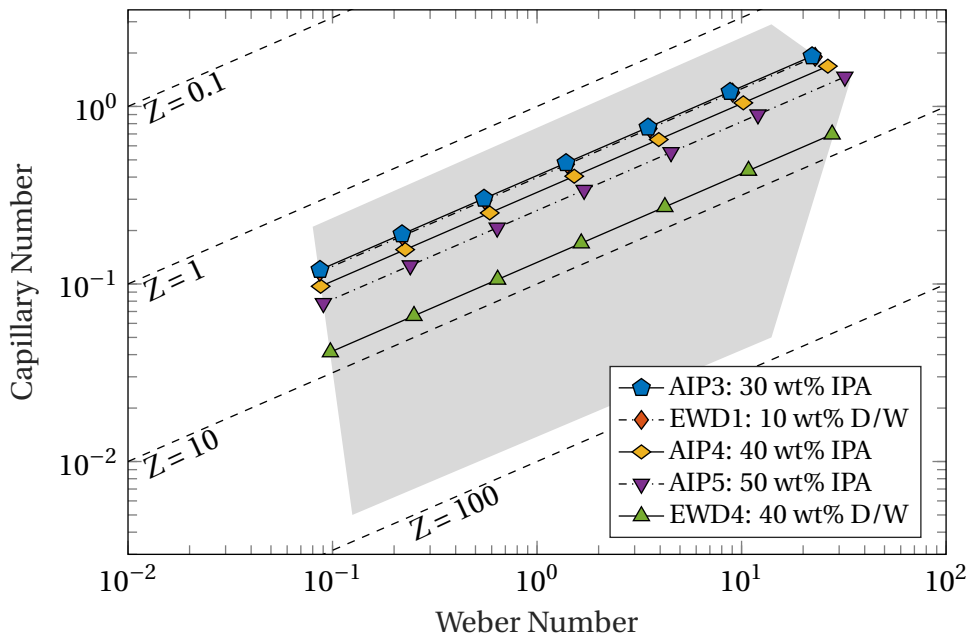
Figure 5.4: The Capillary and Weber numbers for the printed suspensions plotted inside the jettability window of the Capillary – Weber parameter space, as defined by Nallan et al. [2], see Section 2.3.2. AIP3 and EWD1 nearly overlap. The velocity ranges for which the suspensions fit inside the jettable area were: AIP3 ≈ 0.32-4.79 m/s, EWD1 ≈ 0.39-6.28 m/s, AIP4 ≈ 0.31-5.31 m/s, AIP5 ≈ 0.31-5.82 m/s, EWD4 ≈ 0.45-7.56 m/s.
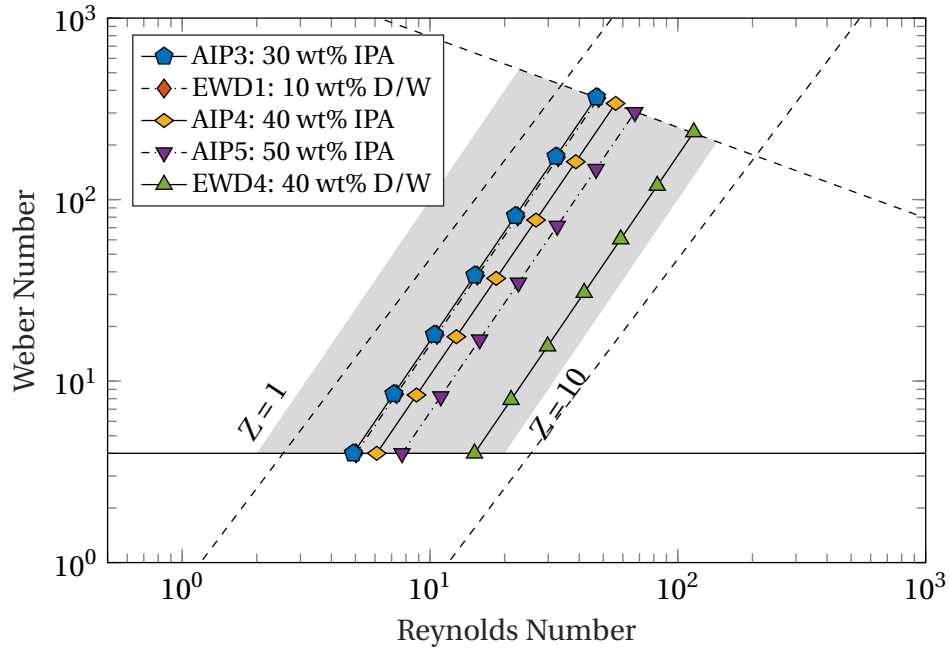
Figure 5.5: The printed suspensions plotted inside the jettability window of the Weber –
Reynolds parameter space, as defined by Derby [3, 4, 5, 6], see Section 2.3.2. AIP3 and
EWD1 nearly overlap. The velocity ranges for which the suspensions fit inside the jettable
area were: AIP3 ≈ 2.12-20.32 m/s, EWD1 ≈ 2.62-25.00 m/s, AIP4 ≈ 2.07-19.01 m/s, AIP5 ≈
2.06-17.91 m/s, EWD4 ≈ 2.87-22.04 m/s.

The printing procedure

To try to indirectly control the printing parameters, a template consisting of squares of dif-
ferent grey scales were created by making black squares and varying the transparency level.
The hypothesis was that this would translate into different amplitude and pulse durations
of the voltage applied to the piezoelectric film, some of which would hopefully fit with the
conditions needed for drop ejection.

　　Printing in several layers was done in an effort to be able to determine how much ce-
ramic powder that was deposited with each layer and how many layers that was needed to
make a coherent green film.

　　The printing was done on premium office paper because of availability and compati-
bility with the printer. Ideally a flatter surface should be used, but the time frame of this
project did not allow further investigation into how this could be achieved in a satisfactory
manner. The use of a dedicated research printer would allow printing on any substrate and
is recommended for further work. A dedicated printer would also allow full control of the

printing parameters and instruments to observe the jetting process.

Empty ink cartridges bought online were used to deliver ink to the printhead. The ink cartridges were reused for the printing of each suspension but was thoroughly cleaned using ultrasonic bath and ethanol between the printing tests. The printhead was flushed with ethanol until all traces of the previously printed suspension was gone, and the printhead was allowed to dry for an hour before the next suspension was printed. To ensure that all the ethanol was removed from the nozzle before the next set of squares were printed, test sheets of large black areas were printed several times to let the new suspension flow through and wash away any remains. The procedure is not foolproof, and some contamination of the suspensions that were printed after the first one is unlikely to have happened. The compositions of the inks are however very similar, and the contaminations are considered to be small, so the effect of them is considered negligible. It could not be guaranteed that any blocked nozzles were completely relieved of the blocking particles through the cleaning procedure that was used.

Analysis of the printed squares

As an initial means of analysing the printed templates, scanning of the full A4 papers were done, and the scans can be found in Appendix E. This did not produce images of high enough quality to distinguish between the different printouts and optical microscopy was therefore applied. The one-layered and ten-layered squares of each suspension were chosen as these were the extreme cases and because of the fact that if the ten-layered squares were not coherent, none of the printouts with fewer layers would be coherent either. The resulting images from the initial analysis are shown in Tables 4.10, 4.11, 4.12, 4.13 and 4.14.

The trends from left to right are easy to distinguish in the printouts for all the suspensions, with higher transparency levels, a lower amount of ink is deposited and hence a lower amount of ceramic particles. Comparison of the one-layered and ten-layered printouts shows, as expected, that more particles are deposited after ten subsequent prints than after one. The observed increase in deposited LSC is however not as large as it was expected to be. There is a possibility that the printhead did not deposit equal amounts or in fact deposit at all in some of the nine printing cycles that were performed after the first one.

It is clear from the images that none of the one-layered squares or squares of 60 % transparency (T-60) or higher were close to forming a coherent film, and focus was thus shifted towards the ten-layered T-0, T-20 and T-40 squares, and especially the T-20. The ten-layered T-20 square was the overall most successful print across all suspensions, as determined from these optical images, indicating that the printing parameters for this setting were the ones fitting the inks and the nozzle size the best. It is unfortunately not possible to find out what the parameters are.

An interesting discontinuity in the trends can be seen when comparing the T-0 prints of the AIP3, AIP4 and AIP5 suspensions. From the AIP3 to the AIP4 suspension the trend seems to be that more powder is deposited, which is in agreement with what is observed when looking at the position of the two suspensions in the Ca–We and We–Re parameter spaces in relation to each other. The AIP4 suspension has a higher Z-parameter than the AIP3 suspension, mostly due to the lower viscosity. Following this logic, the T-0 of the AIP5 suspension should have even more powder deposited, but this is not the case. Only a few lines were deposited where there should be a full square. In the case of the AIP5 suspensions it is important to note that the ten-layered squares were printed from scratch after all the five first layers were printed. This explains why some lines can be seen in the one-layered deposit that are not present in the ten-layered deposit. One possible explanation for the discontinuity seen from the AIP3 and AIP4 to the AIP5 suspension is temporary blocking of the nozzle by air bubbles, which is known to play an important role in jetting stability [38]. Partial blocking of the nozzle by powder particles can also play a role, effectively reducing the nozzle diameter. All the other squares of different transparency levels were printed almost without artefacts, so there can not have been a permanent blocking of the nozzles. Another possibility is that the frequency at which the printer tried to print the T-0 square was too high and hence the voltage pulse too short to allow jetting. A combination may also be the case.

For the EWD1 and EWD4 suspensions the same trend downwards can be seen as for the AIP3 and AIP4 suspensions, more suspension and powder is deposited for the suspension that is lower in the Ca–We parameter space and more to the right in the We–Re parameter space.

Since the AIP3 and the EWD1 suspensions nearly overlap in the Ca–We and We–Re

parameter spaces, the suspensions are expected to behave similarly during printing. A large difference can be seen in the print quality of the T-0 squares, where the EWD1 has deposited a lot less than the AIP3. Looking at the velocity requirements, a lower applied voltage is needed to jet the AIP3 compared to the EWD1, but the difference is small. The EWD1 suspension is both more viscous and has a higher surface tension than the AIP3 suspension. It is the surface tension force that needs to be overcome for droplet ejection to take place [5], and this may be the reason why poorer prints are shown for EWD1.

The overall higher surface tension of the EWD suspensions as compared to the AIP suspensions also result in a more smudged print, as is especially visible in the prints of the EWD4 where the edges are not as straight as they should be and the «white»spaces are more grey-ish. This is in accordance with the theory for liquid jet breakdown. The higher surface tension can cause both spheroidisation (satellite drop formation) of the jetted liquid thread and a spraying effect at the nozzle opening due to wetting of the face of the outlet [60]. These are characteristics of the jetting breakdown mechanisms explained in Section 2.3.2 and shown as region III and IV in Figure 2.11. The EWD4 suspension is situated closer to region III in the Ca–We parameter space and the spraying breakdown mechanism is therefore most likely the dominant reason for the poor accuracy of the print.
Scanning electron microscopy was performed on gold coated ten-layered T-20 squares from each of the five printed suspensions. In addition, the T-0 and the T-40 of the AIP5 suspension was analysed to better see the effect of different transparency within the prints for one suspension. The resulting micrographs are presented at three different magnifications of the same area in Tables 4.15-4.19. Larger versions are available in Appendix F at four different magnifications.

The SEM micrographs immediately give away the roughness of the surface of the paper. The topographic irregularity caused by the paper fibres are several times larger in magnitude than the amount of deposited powder can fill in even after ten printed layers. Capillary forces in the hollow voids between the fibres will influence a deposited drop and cause the powder to be distributed very differently than what it would be if deposited on a flat surface where only evaporative effects would play a role. It is therefore very hard to determine how thick and uniform a film would be if deposited onto a SOFC electrolyte.

Some trends can however be seen both between the different suspensions and within

the AIP5 prints of different transparency: In general, the observed particle sizes are small, much smaller than 1 µm, in accordance with the results from the particle size distribution measurements. The particles in the EWD suspension also look larger than the AIP ones, as if they were more heavily agglomerated. This is also as suspected from the PSD measurements. The particles in the AIP suspensions seem to be covered by a fluffy material. It is suspected that this is the polyvinylpyrrolidone that has come out of solution during the drying of the deposited drops. The PVP may be the reason why the AIP suspensions seem to cover more of the surface than the EWD suspension do. Among the AIP suspensions, the suspension that seem to have got the most coherent coverage in the most populated areas is the AIP5. Among the two EWD suspensions the EWD4 has a far superior coverage. Among the AIP5 prints, the T-20 had the best coverage overall, while the T-0 had a very good coverage in the particular area that is presented in the micrographs. EDS analysis of the squares would probably help in showing the real LSC coverage better, but this was not conducted in this work.

Chapter 6

Conclusion and further work

6.1   Conclusion

The possibility of making a stable suspension of $(La_{0,8}Sr_{0,2})_{0,995}CoO_3$ (LSC)-powder with appropriate properties for use as an ink in ink-jet printing of thin film SOFC-cathodes has been investigated.

Ten suspensions were made by ball milling all constituents of a given suspension and filtering the resulting fluid through a 2 μm syringe filter. The loss of suspension through the manufacturing process was less than 5 % and the solid content of the suspensions remained high at around 19 wt%, out of the original 20 wt%.

The suspensions were divided into two series of five with distinctly different compositions of liquid carrier media, additives and stabilisers. The α-Terpineol, isopropanol and polyvinylpyrrolidone suspensions proved to have superior stability compared to the ethylene glycol, distilled water and Dolapix CE 64 suspensions. Characterisation of the particle size distribution revealed heavy agglomeration in the EWD suspensions with a $\mathbf{D}_{n,90}$ of 1.08-1.37 μm compared to ~0.25 μm in the AIP suspensions. After a two day sedimentation test, all EWD suspensions had sedimented while the AIP suspensions showed good stability that decreased with increasing isopropanol content, attributed to the decrease in viscosity.

Characterisation of the suspensions' density, viscosity and surface tension were performed to allow calculation of the Z-parameter (Ohnesorge number reciprocal) and the Capillary, Weber and Reynolds numbers. All suspensions had a Z-parameter value in the

range of 1–10 and all except for the α-Terpineol based suspension with 10 wt% isopropanol were fitted inside the jettability window of both the Capillary–Weber parameter space defined by Nallan et al. [2] and the Weber–Reynolds parameter space defined by Derby [3, 4, 5, 6]. This indicated that at least nine out of ten produced suspensions should be jettable for a printer nozzle head of $\approx 22\,\mu m$.

Five of the suspensions were printed onto paper using an Epson WorkForce® WF-2630 piezoelectric drop on demand printer and the printouts were examined using optical and scanning electron microscopy. None of the suspensions formed a completely coherent layer of LSC-powder on the paper surface, but the α-Terpineol based suspensions showed superior coverage compared to the ethylene glycol based ones with local coherency and higher printing accuracy due to lower satellite drop formation. The roughness and moisture absorbing properties of the paper surface removes to a large extent the ability to determine the morphology of a thin film and how it would look and vary from one suspension to the next.

6.2   Further work

Method of manufacture

To better compare the ball milling manufacturing method to rod stirring and ultrasonication, equal suspensions should be made using both methods and the resulting inks should be characterised and compared both when it comes to particle size distribution, stability, fluid properties and printing performance. The losses in each step of both methods of manufacture should be calculated and taken into account when comparing them.

Suspension stability

The α-Terpineol and isopropanol based suspensions should be made with various amounts of PVP to determine the optimal amount for maximum stability. The stability, both with respect to agglomeration and sedimentation, should be evaluated by more thorough particle size analysis of the suspensions both from the top and bottom of the suspension over a longer period of time. The amount of isopropanol to α-Terpineol should mainly be used to

adjust the viscosity to fit the suspension within the bounds of the jettability criteria.

The ethylene glycol and distilled water based suspensions should be subjected to electrophoretic mobility measurements at different pH values to be able to calculate the maximum zeta-potential for different amounts of added Dolapix CE 64. A high zeta-potential is a measure of good stability. If finding a configuration with a high zeta potential fails and no stable suspension can be made, a new composition for an aqueous suspension should be considered altogether.

Fluid properties

An investigation into how the solid loading, the amount of stabiliser and temperature affects the viscosity and surface tension of a suspension could lead to new insights as to how to best design a ceramic ink.

As inks are tested on other substrates than paper and the effect of capillary draining on the distribution of deposited particles is reduced, effects like the coffee staining effect (explained by Deegan et al. [61]) will play a larger role in how powder is distributed on a surface. Investigation into how the fluid properties of the liquid components in the suspension affects the drying of the drop, and hence the deposition of particles, should be conducted.

Printing and Fuel Cell production

A materials printer that is specifically designed for R&D and feasibility testing should be acquired for any further ink-jet related research. It is necessary to have full control over the printing parameters; drive voltage, waveform and frequency, as well as nozzle size to be able to determine the real potential of the ink under investigation. Several such printers exist on the market (Dimatix Materials Printer DMP-2850, Notion N.Jet and Super Inkjet Printer SIJ-S030 to name a few), or can be custom built using available parts, as done by several researchers [2, 62]. Most of these systems also include tools for optical inspection of the jetted fluid for more detailed analysis of the jet breakup mechanisms of inks under different conditions. A dedicated printer would also allow printing of green ceramics on any substrate and further enable the production of a small scale Solid Oxide Fuel Cell that

can be tested for performance.

Bibliography

[1] D. T. Rogstad, "Preparation of (La0,8Sr0,2)0,995CoO3-based inks for ink-jet printing of thin films in Solid Oxide Fuel Cells (SOFCs)," tech. rep., Norwegian University of Science and Technology, 2016.

[2] H. C. Nallan, J. A. Sadie, R. Kitsomboonloha, S. K. Volkman, and V. Subramanian, "Systematic design of jettable nanoparticle-based inkjet inks: Rheology, acoustics, and jettability," *Langmuir*, vol. 30, pp. 13470–13477, 11 2014.

[3] B. Derby and N. Reis, "Inkjet Printing of Highly Loaded Particulate Suspensions," *MRS Bulletin*, vol. 28, pp. 815–818, 11 2003.

[4] B. Derby, "Inkjet Printing of Functional and Structural Materials: Fluid Property Requirements, Feature Stability, and Resolution," *Annual Review of Materials Research*, vol. 40, no. 1, pp. 395–414, 2010.

[5] B. Derby, "Inkjet printing ceramics: From drops to solid," *Journal of the European Ceramic Society*, vol. 31, no. 14, pp. 2543–2550, 2011.

[6] B. Derby, "Additive Manufacture of Ceramics Components by Inkjet Printing," *Engineering*, vol. 1, no. 1, pp. 113–123, 2015.

[7] T. Somekawa, K. Nakamura, T. Kushi, T. Kume, K. Fujita, and H. Yakabe, "Examination of a high-efficiency solid oxide fuel cell system that reuses exhaust gas," *Applied Thermal Engineering*, 2016.

[8] E. D. Wachsman and K. T. Lee, "Lowering the Temperature of Solid Oxide Fuel Cells," *Science*, vol. 334, no. 6058, pp. 935–939, 2011.

[9] N. Q. Minh, "Ceramic Fuel Cells," *Journal of the American Ceramic Society*, vol. 76, pp. 563–588, 3 1993.

[10] B. C. Steele and A. Heinzel, "Materials for fuel-cell technologies.," *Nature*, vol. 414, no. 6861, November, pp. 345–352, 2001.

[11] S. Singhal, "Advances in solid oxide fuel cell technology," *Solid State Ionics*, vol. 135, no. 1, pp. 305–313, 2000.

[12] D. Brett, A. Atkinson, N. Brandon, and S. Skinner, "Intermediate temperature solid oxide fuel cells," *Chemical Society Reviews*, vol. 37, no. 8, pp. 1568–1578, 2008.

[13] J. Larminie and A. Dicks, *Fuel Cell Systems Explained*, vol. 93. John Wiley & Sons Ltd, 2001.

[14] S. S. Høyem, "Optimisation of Spray Pyrolysed (La0.6Sr0.4)0.99CoO3 Cathodes for Solid Oxide Fuel Cells," Tech. Rep. July, NTNU, 2016.

[15] N. Mahato, A. Banerjee, A. Gupta, S. Omar, and K. Balani, "Progress in material selection for solid oxide fuel cell technology: A review," *Progress in Materials Science*, vol. 72, pp. 141–337, 2015.

[16] I. Garbayo, V. Esposito, S. Sanna, A. Morata, D. Pla, L. Fonseca, N. Sabaté, and A. Tarancón, "Porous La0.6Sr0.4CoO3-δ thin film cathodes for large area micro solid oxide fuel cell power generators," *Journal of Power Sources*, vol. 248, pp. 1042–1049, 2014.

[17] C. Benel, A. J. Darbandi, R. Djenadic, A. Evans, R. Tölke, M. Prestat, and H. Hahn, "Synthesis and characterization of nanoparticulate La0.6Sr 0.4CoO3-δ cathodes for thin-film solid oxide fuel cells," *Journal of Power Sources*, vol. 229, pp. 258–264, 2013.

[18] S. Y. Park, H. I. Ji, H. R. Kim, K. J. Yoon, J. W. Son, B. K. Kim, H. J. Je, H. W. Lee, and J. H. Lee, "Structural optimization of (La, Sr)CoO3-based multilayered composite cathode for solid-oxide fuel cells," *Journal of Power Sources*, vol. 228, pp. 97–103, 2013.

[19] J. Hayd, L. Dieterle, U. Guntow, D. Gerthsen, and E. Ivers-Tiffée, "Nanoscaled La0.6Sr0.4CoO3-δ as intermediate temperature solid oxide fuel cell cathode: Microstructure and electrochemical performance," *Journal of Power Sources*, vol. 196, no. 17, pp. 7263–7270, 2011.

[20] H. S. Noh, K. J. Yoon, B. K. Kim, H. J. Je, H. W. Lee, J. H. Lee, and J. W. Son, "The potential and challenges of thin-film electrolyte and nanostructured electrode for yttria-stabilized zirconia-base anode-supported solid oxide fuel cells," *Journal of Power Sources*, vol. 247, pp. 105–111, 2014.

[21] C. Williams, "Ink-jet printers go beyond paper," *Physics World*, vol. 19, pp. 24–29, 2006.

[22] R. I. Tomov, M. Krauz, J. Jewulski, S. C. Hopkins, J. R. Kluczowski, D. M. Glowacka, and B. A. Glowacki, "Direct ceramic inkjet printing of yttria-stabilized zirconia electrolyte layers for anode-supported solid oxide fuel cells," *Journal of Power Sources*, vol. 195, no. 21, pp. 7160–7167, 2010.

[23] C. Wang, S. C. Hopkins, R. I. Tomov, R. V. Kumar, and B. A. Glowacki, "Optimisation of CGO suspensions for inkjet-printed SOFC electrolytes," *Journal of the European Ceramic Society*, vol. 32, no. 10, pp. 2317–2324, 2012.

[24] G. D. Han, K. C. Neoh, K. Bae, H. J. Choi, S. W. Park, J. W. Son, and J. H. Shim, "Fabrication of lanthanum strontium cobalt ferrite (LSCF) cathodes for high performance solid oxide fuel cells using a low price commercial inkjet printer," *Journal of Power Sources*, vol. 306, pp. 503–509, 2016.

[25] N. Yashiro, T. Usui, and K. Kikuta, "Application of a thin intermediate cathode layer prepared by inkjet printing for SOFCs," *Journal of the European Ceramic Society*, vol. 30, no. 10, pp. 2093–2098, 2010.

[26] D. Young, A. M. Sukeshini, R. Cummins, H. Xiao, M. Rottmayer, and T. Reitz, "Ink-jet printing of electrolyte and anode functional layer for solid oxide fuel cells," *Journal of Power Sources*, vol. 184, no. 1, pp. 191–196, 2008.

[27] E. Özkol, J. Ebert, K. Uibel, A. M. Wätjen, and R. Telle, "Development of high solid content aqueous 3Y-TZP suspensions for direct inkjet printing using a thermal inkjet printer," *Journal of the European Ceramic Society*, vol. 29, pp. 403–409, 2 2009.

[28] T. Bakarič, B. Malič, and D. Kuscer, "Lead-zirconate-titanate-based thick-film structures prepared by piezoelectric inkjet printing of aqueous suspensions," *Journal of the European Ceramic Society*, vol. 36, no. 16, pp. 4031–4037, 2016.

[29] H. Kipphan, *Handbook of Print Media.* Springer-Verlag Berlin Heidelberg, 2001.

[30] P. Hiemenz and R. Rajagopalan, *Principles of colloid and surface chemistry.* CRC Press, third ed., 1997.

[31] V. A. Hackley and C. F. Ferraris, "The use of nomenclature in dispersion science and technology," *NIST Special Publication*, vol. 960, p. 76, 2001.

[32] N. J. Wagner and J. F. Brady, "Shear thickening in colloidal dispersions," *Physics Today*, no. Oktober, pp. 27–32, 2009.

[33] G. H. McKinley and M. Renardy, "Wolfgang von Ohnesorge," *Physics of Fluids*, vol. 23, no. 12, 2011.

[34] J. Tai, H. Y. Gan, Y. N. Liang, and B. K. Lok, "Control of droplet formation in inkjet printing using ohnesorge number category: Materials and processes," in *10th Electronics Packaging Technology Conference, EPTC 2008*, pp. 761–766, IEEE, 12 2008.

[35] M. Bienia, M. Lejeune, M. Chambon, V. Baco-Carles, C. Dossou-Yovo, R. Noguera, and F. Rossignol, "Inkjet printing of ceramic colloidal suspensions: Filament growth and breakup," *Chemical Engineering Science*, vol. 149, pp. 1–13, 2016.

[36] D. Jang, D. Kim, and J. Moon, "Influence of fluid physical properties on ink-jet printability," *Langmuir*, vol. 25, pp. 2629–2635, 3 2009.

[37] M. Lejeune, T. Chartier, C. Dossou-Yovo, and R. Noguera, "Ink-jet printing of ceramic micro-pillar arrays," *Journal of the European Ceramic Society*, vol. 29, no. 5, pp. 905–911, 2009.

[38] H. Wijshoff, "The dynamics of the piezo inkjet printhead operation," *Physics Reports*, vol. 491, no. 4-5, pp. 77–177, 2010.

[39] S. D. Hoath, W.-K. Hsiao, S. Jung, G. D. Martin, I. M. Hutchings, N. F. Morrison, and O. G. Harlen, "Drop Speeds from Drop-on-Demand Ink-Jet Print Heads," *Journal of Imaging Science and Technology*, vol. 57, pp. 1–11, 1 2013.

[40] C. D. Stow and M. G. Hadfield, "An Experimental Investigation of Fluid Flow Resulting from the Impact of a Water Drop with an Unyielding Dry Surface," *Proceedings of the Royal Society A: Mathematical, Physical and Engineering Sciences*, vol. 373, pp. 419–441, 1 1981.

[41] R. Bhola and S. Chandra, "Parameters controlling solidification of molten wax droplets falling on a solid surface," *Journal of Materials Science*, vol. 34, no. 19, pp. 4883–4894, 1999.

[42] S. Weber, "LSC powder preparation," *Personal communication*, 2016.

[43] H. Sarraf and J. Havrda, "Rheological Behavior of Concentrated Alumina Suspension : Effect of Electrosteric Stabilization," *Ceramics Silikaty*, vol. 51, pp. 147–152, 2007.

[44] ThermoFischer Scientific, "Finnpipette F2 Brochure." `https://tools.thermofisher.com/content/sfs/brochures/D13201~.pdf`, Last visited 25.05.2017.

[45] Horiba Instruments Inc., "A Guidebook to Particle Size Analysis." `https://www.horiba.com/fileadmin/uploads/Scientific/eMag/PSA/Guidebook/pdf/PSA_Guidebook.pdf`, Last visited 02.06.2016.

[46] I. B. Bekard, P. Asimakis, J. Bertolini, and D. E. Dunstan, "The effects of shear flow on protein structure and function," *Biopolymers*, vol. 95, no. 11, pp. 733–745, 2011.

[47] J. D. Berry, M. J. Neeson, R. R. Dagastine, D. Y. Chan, and R. F. Tabor, "Measurement of surface and interfacial tension using pendant drop tensiometry," *Journal of Colloid and Interface Science*, vol. 454, pp. 226–237, 9 2015.

[48] Krüss GmbH, "Pendant Drop." `https://www.kruss.de/services/education-theory/glossary/pendant-drop/`, Last visited 02.06.2017.

[49] Epson Inc., "Product Specifications - WorkForce® WF-2630." `https://files.support.epson.com/docid/cpd4/cpd41107.pdf`, Last visited 05.06.2017.

[50] W. M. Haynes, ed., *CRC Handbook of Chemistry and Physics*. Boca Raton, FL.: CRC Press/Taylor & Francis, 97th edition ed., 2017.

[51] F. S. Jerome, J. T. Tseng, and L. T. Fan, "Viscosities of aqueous glycol solutions," *Journal of Chemical & Engineering Data*, vol. 13, pp. 496–496, 10 1968.

[52] Huntsman Corporation, "Ethylene, Diethylene and Triethylene Glycols." `http://www.huntsman.com/performance_products/Media%20Library/a_MC348531CFA3EA9A2E040EBCD2B6B7B06/Products_MC348531D0B9FA9A2E040EBCD2B6B7B06/Glycols_MC348531D11A3A9A2E040EBCD2B6B7B06/files/eg_deg_teg_brochure_full.pdf`, Last visited 29.06.2017.

[53] J. Kestin, M. Sokolov, and W. A. Wakeham, "Viscosity of liquid water in the range 8 °C to 150 °C," *Journal of Physical and Chemical Reference Data*, vol. 7, pp. 941–948, 7 1978.

[54] Fujifilm Dimatix, Inc., "Jettable Fluid Formulation Guidelines." `https://www.fujifilmusa.com/shared/bin/Dimatix-Materials-Printer-Jettable-Fluid-Formulation-Guidelines.pdf`, Last visited 14.06.2017.

[55] V. Esposito, C. Gadea, J. Hjelm, D. Marani, Q. Hu, K. Agersted, S. Ramousse, and S. H. S. H. Jensen, "Fabrication of thin yttria-stabilized-zirconia dense electrolyte layers by inkjet printing for high performing solid oxide fuel cells," *Journal of Power Sources*, vol. 273, pp. 89–95, 1 2015.

[56] M. T. Zafarani-Moattar, H. Shekaari, R. Munes-Rast, and R. Majdan-Cegincara, "Stability and rheological properties of nanofluids containing ZnO nanoparticles, poly(propylene glycol) and poly(vinyl pyrrolidone)," *Fluid Phase Equilibria*, vol. 403, pp. 136–144, 2015.

[57] P. Hjalmarsson, M. Søgaard, A. Hagen, and M. Mogensen, "Structural properties and electrochemical performance of strontium- and nickel-substituted lanthanum cobaltite," *Solid State Ionics*, vol. 179, no. 17-18, pp. 636–646, 2008.

[58] C. Li, H. Chen, H. Shi, M. O. Tade, and Z. Shao, "Green fabrication of composite cathode with attractive performance for solid oxide fuel cells through facile inkjet printing," *Journal of Power Sources*, vol. 273, 2015.

[59] N. Reis, C. Ainsley, and B. Derby, "Ink-jet delivery of particle suspensions by piezoelectric droplet ejectors," *Journal of Applied Physics*, vol. 97, no. 9, 2005.

[60] N. Reis and B. Derby, "Ink jet deposition of ceramic suspensions: Modeling and experiments of droplet formation," *MRS proceedings*, vol. 625, no. January 2000, pp. 117–122, 2000.

[61] R. D. Deegan, O. Bakajin, T. F. Dupont, G. Huber, S. R. Nagel, and T. A. Witten, "Capillary flow as the cause of ring stains from dried liquid drops," *Nature*, vol. 389, no. 6653, pp. 827–829, 1997.

[62] M. Pack, H. Hu, D.-O. Kim, X. Yang, and Y. Sun, "Colloidal Drop Deposition on Porous Substrates: Competition among Particle Motion, Evaporation, and Infiltration," *Langmuir*, vol. 31, pp. 7953–7961, 7 2015.

Appendix A

Powder characterisation

The LSC-powder used in this work comes from the same batch as the one characterised in Rogstad [1]. A short summary of some of the results from the characterisation will be given here.

A.1 Phase purity

The LSC-powder was found to be phase pure by XRD after calcination at 900 °C for 6 hours. It matched the monoclinic I2/a perovskite phase of $La_{0,8}Sr_{0,2}CoO_3$ (PDF card 04-014-5178).
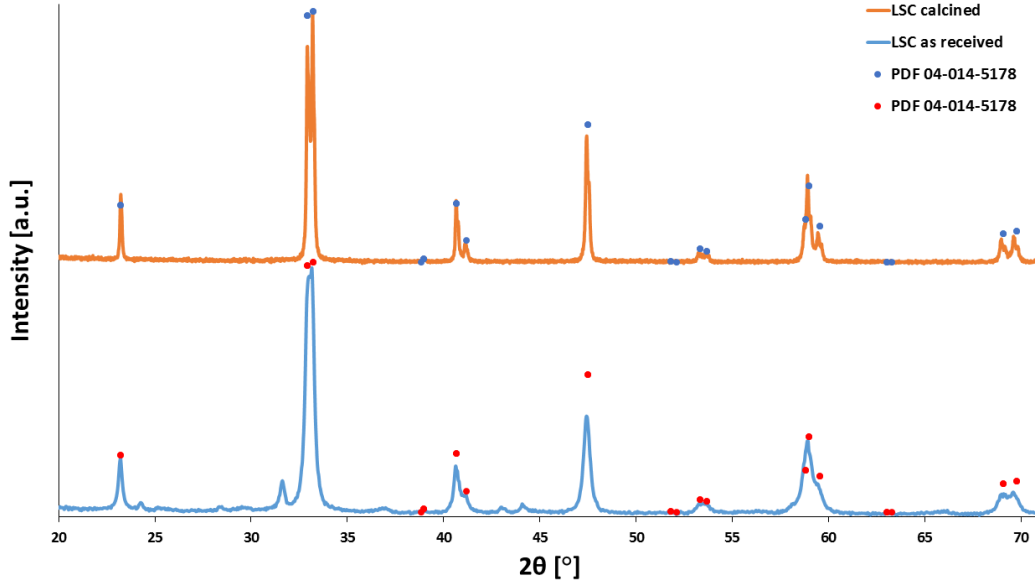
Figure A.1: XRD diffractograms for the LSC powder as received from CerPoTech (bottom) and after calcination at 900 °C for 6 hours (top). References for $La_{0,8}Sr_{0,2}CoO_3$ (PDF 04-014-5178) are marked as blue and red dots. Reprinted from Rogstad [1].

A.2   Particle size and morphology

The crystallite and particle sizes of the powder were calculated from XRD-, BET- and laser diffraction data. The results are given in Table A.1.

Table A.1: Average particle sizes from surface area (BET) and number based laser scattering measurements ($\bar{d}_s$, $\bar{d}_n$) and crystallite (d_{XRD}) size calculated for the as-received LSC-powder. Reprinted from Rogstad [1].

Sample	d_{XRD} [nm]	$\bar{d}_s$ [nm]	$\bar{d}_n$ [nm]
$(La_{0,8}Sr_{0,2})_{0,995}CoO_3$	25.1	70.8	291

Scanning Electron Microscopy was used to investigate the morphology of the powder and to give a more direct observation of the particle sizes. A spherical morphology was revealed and typical particle sizes as well as the largest observed particle are shown in Figure A.2 **(a)** and **(b)**, respectively.

(a) Typical particle sizes **(b)** Large particle
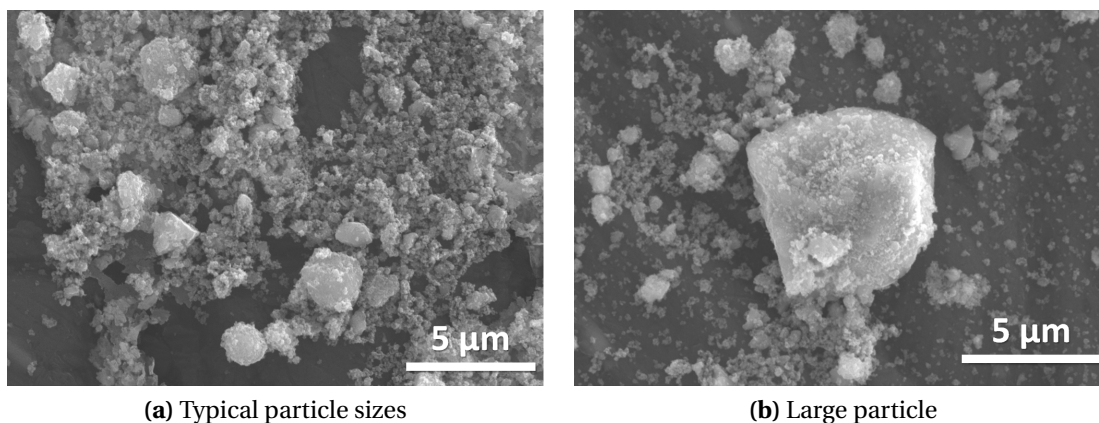
Figure A.2: SEM micrographs showing particle sizes and morphology of the LSC-powder. The powder was mixed with isopropanol and sonicated for one minute before analysis in the SEM. Reprinted from Rogstad [1].

Appendix B

Calculations

B.1   Suspension characterisation

B.1.1   Method of suspension manufacturing

Table B.1: The amount of suspension retrieved after the milling step, by weight (g) and as a percentage of the weight of the initially made suspension. The bottle in which the milling step was performed was weighed before and after removal of the suspension by syringe.

Sample	Bottle weight [g]		Suspension retrieved	
AIP suspensions	Before	After	[g]	[%]
AIP1	123.749	101.27	22.479	92.58
AIP2	121.252	98.839	22.413	95.24
AIP3	110.068	88.352	21.716	95.14
AIP4	118.678	97.685	20.993	94.79
AIP5	114.361	97.055	17.306	80.43
EWD suspensions				
EWD1	121.483	95.852	25.631	93.07
EWD2	125.187	99.473	25.714	94.73
EWD3	122.696	97.029	25.667	95.87
EWD4	127.149	101.953	25.196	95.40
EWD5	119.140	94.416	24.724	94.87

B.1.2 Solid loading

The solid loading of each suspension after filtering through a 2 μm borosilicate glass syringe filter was found by evaporating and burning off the volatile species in the suspension at 600 °C for two hours. The calculation of the solid loading can be seen in Table B.2.

Table B.2: Determination of solid content through evaporation of liquids and burnoff of volatile species

Sample	Weight before burnoff [g]		Weight after burnoff [g]	Solid content [%]
AIP suspensions	Crucible + kao wool	Suspension	Crucible + kao wool + solids	
AIP1	32.6091	0.5045	32.7030	**18.61**
AIP2	34.9691	0.5045	35.0646	**18.93**
AIP3	32.2918	0.5417	32.3950	**19.05**
AIP4	34.8440	0.5150	34.9440	**19.42**
AIP5	32.5416	0.5172	32.6414	**19.30**
EWD suspensions				
EWD1	32.4751	0.5159	32.5729	**18.96**
EWD2	32.4721	0.5040	32.5695	**19.33**
EWD3	34.9672	0.5170	35.0636	**18.65**
EWD4	34.9649	0.5478	35.0719	**19.53**
EWD5	32.4634	0.5850	32.5786	**19.69**

B.1.3 Density

The density measurements were carried out at approximately 23 °C. Initial measurements on distilled water were performed to check if the pipette was calibrated. The calculated density of the water can be seen in Table B.3 and compared to reference density values given in Table B.4.

Table B.3: Measured weights of 5000 µl of distilled water and the density calculated as the arithmetic mean weight divided by the volume. The indicated uncertainty is the sample standard deviation.

Measurement [#]	Distilled water [g]
1	4.9903
2	4.9891
3	4.9897
4	4.9894
5	4.9763
6	4.9869
Density [g/ml]	0.997 ± 0.001

Table B.4: Density of water at atmospheric pressure for temperatures ranging from 20-25 °C. Extracted from the table "Standard density of water" in CRC Handbook of Chemistry and Physics [50].

Temperature [°C]	Density [g/mL]
20	0.998207
21	0.997996
22	0.997774
23	0.997542
24	0.997300
25	0.997048

Appendix C

SEM micrographs for determining nozzle diameter

The printerhead of the Epson WF-2630 was removed from the printer after the suspensions had been printed. It was flushed and washed in ethanol in an ultrasonic bath for 30 minutes and then dried off in a drying cabinet for two days prior to examination in a Zeiss Ultra 55 LE. Twelve nozzles were examined. It appeared that the inner edge of each nozzle was damaged, but it is uncertain whether this was caused by the printing process or the washing procedure. For comparison, a nozzle from an older Epson printer is shown in Figure C.1. The inner diameter of each nozzle was nonetheless determined by fitting a circle inside the innermost edge of the nozzle, and a mean value of $21.8 \pm 0.7\,\mu m$ was calculated.

Table C.1: SEM micrographs of six of the twelve nozzles on the printhead of the Epson Workforce® WF2630 used to determine a mean nozzle diameter.
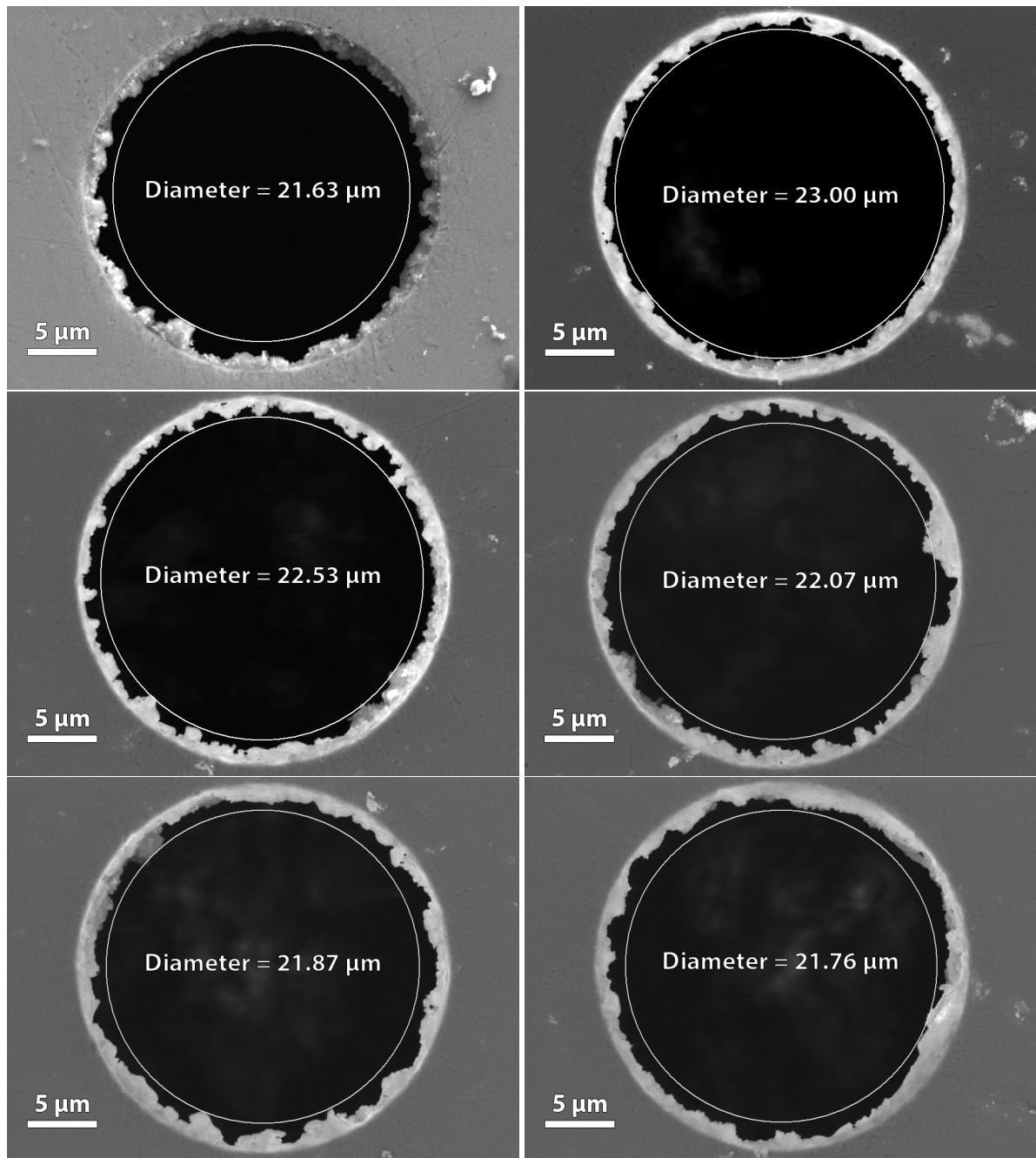
Table C.2: SEM micrographs of six of the twelve nozzles on the printhead of the Epson Workforce® WF2630 used to determine a mean nozzle diameter.
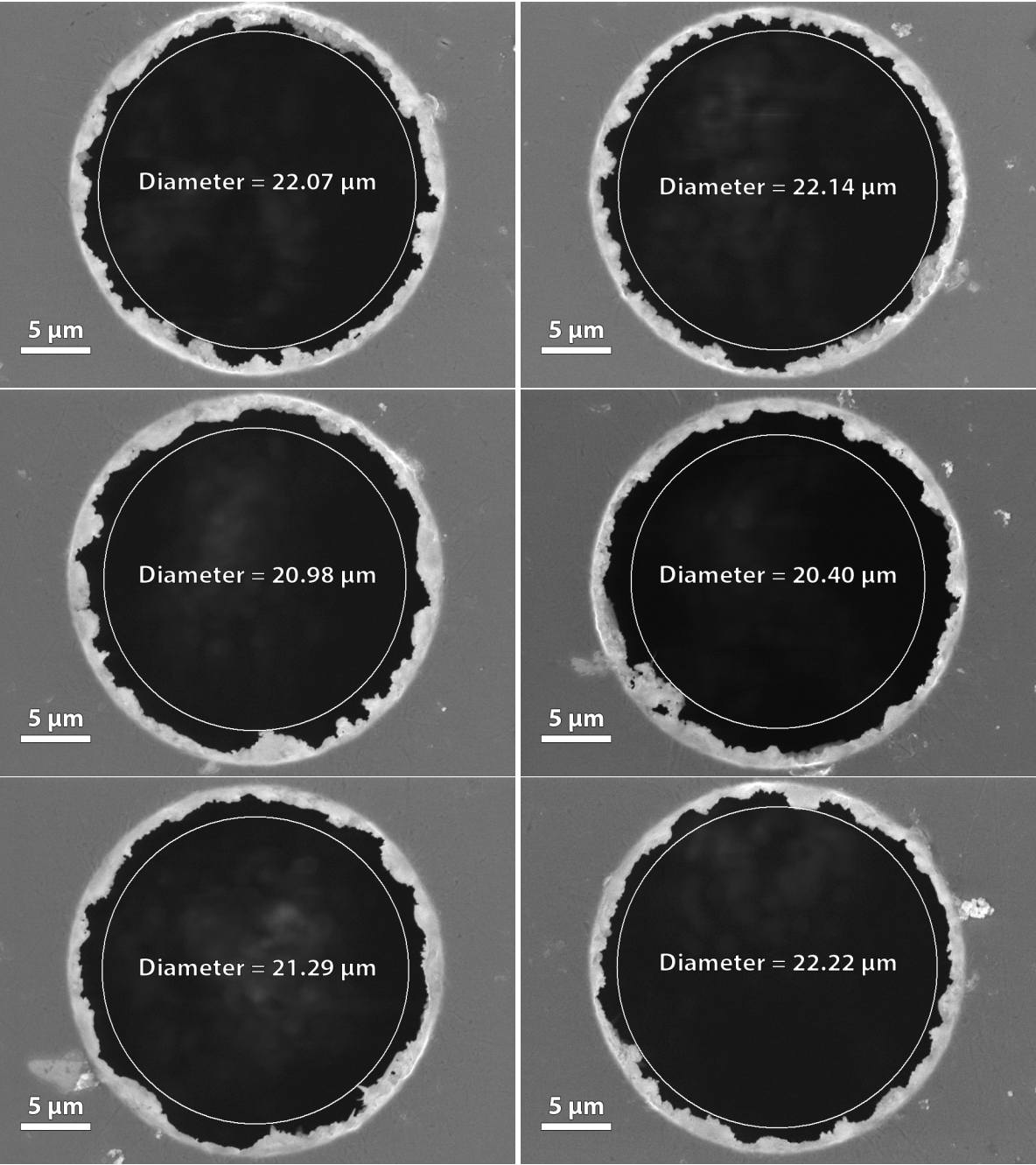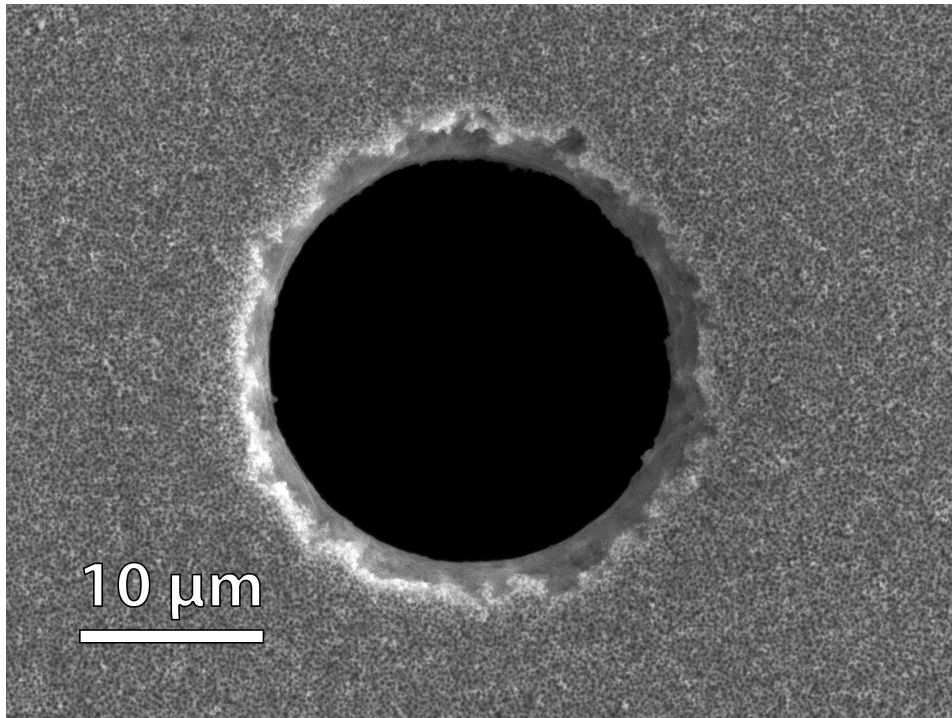
Figure C.1: SEM micrograph of one nozzle in the printhead of an Epson Stylus Photo R200.

Appendix D

Templates used in the printing of suspensions

The following pages shows the template for the first, second, third, fourth, fifth and tenth layer, respectively. The templates were printed onto the same sheet of paper in the presented order. To reach the tenth layer, the last template was printed five times after the fifth layer template. T-0, T-20, T-40, T-60 and T-80 describes the level of transparency of the black squares in percent.

1 Layer:

T-0	T-20	T-40	T-60	T-80

2 Layers:

T-0	T-20	T-40	T-60	T-80

3 Layers:

T-0	T-20	T-40	T-60	T-80

4 Layers:

T-0	T-20	T-40	T-60	T-80

5 Layers:

T-0	T-20	T-40	T-60	T-80

10 Layers:

T-0	T-20	T-40	T-60	T-80
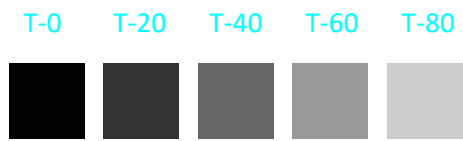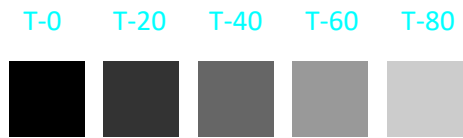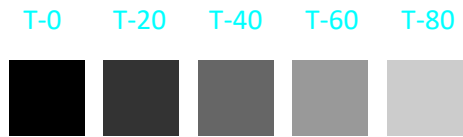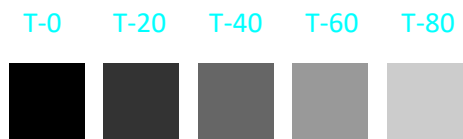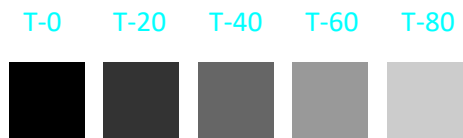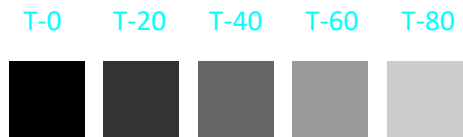
Appendix E

Full scans of printed suspensions

Five out of the ten manufactured suspensions were printed according to the templates shown in Appendix D. The sheets onto which the suspensions were printed were scanned and the resulting scans are given on the following pages.

1 Layer:

T-0	T-20	T-40	T-60	T-80

2 Layers:

T-0	T-20	T-40	T-60	T-80

3 Layers:

T-0	T-20	T-40	T-60	T-80

4 Layers:

T-0	T-20	T-40	T-60	T-80

5 Layers:

T-0	T-20	T-40	T-60	T-80

10 Layers:

T-0	T-20	T-40	T-60	T-80

1 Layer:

T-0	T-20	T-40	T-60	T-80

2 Layers:

T-0	T-20	T-40	T-60	T-80

3 Layers:

T-0	T-20	T-40	T-60	T-80

4 Layers:

T-0	T-20	T-40	T-60	T-80

5 Layers:

T-0	T-20	T-40	T-60	T-80

10 Layers:

T-0	T-20	T-40	T-60	T-80

1 Layer:

| T-0 | T-20 | T-40 | T-60 | T-80 |

2 Layers:

| T-0 | T-20 | T-40 | T-60 | T-80 |

3 Layers:

| T-0 | T-20 | T-40 | T-60 | T-80 |

4 Layers:

| T-0 | T-20 | T-40 | T-60 | T-80 |

5 Layers:

| T-0 | T-20 | T-40 | T-60 | T-80 |

10 Layers:

| T-0 | T-20 | T-40 | T-60 | T-80 |

1 Layer:

T-0	T-20	T-40	T-60	T-80

2 Layers:

T-0	T-20	T-40	T-60	T-80
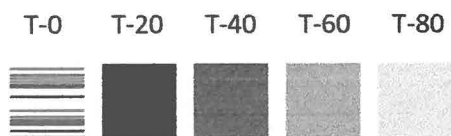
3 Layers:

T-0	T-20	T-40	T-60	T-80
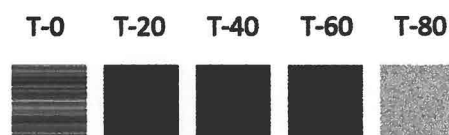
4 Layers:
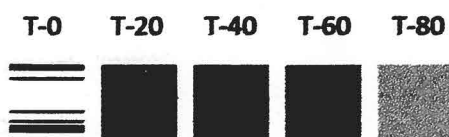
T-0	T-20	T-40	T-60	T-80
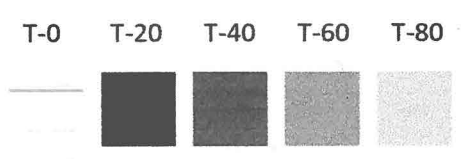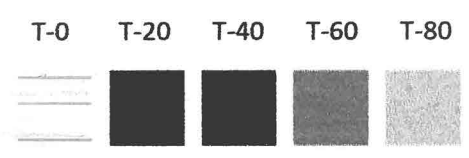
5 Layers:
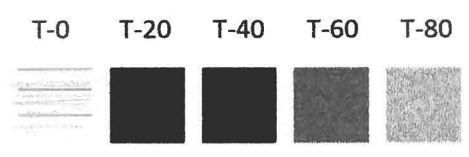
T-0	T-20	T-40	T-60	T-80

10 Layers:

T-0	T-20	T-40	T-60	T-80

1 Layer:

| T-0 | T-20 | T-40 | T-60 | T-80 |

2 Layers:

| T-0 | T-20 | T-40 | T-60 | T-80 |

3 Layers:

| T-0 | T-20 | T-40 | T-60 | T-80 |

4 Layers:

| T-0 | T-20 | T-40 | T-60 | T-80 |

5 Layers:

| T-0 | T-20 | T-40 | T-60 | T-80 |

10 Layers:

| T-0 | T-20 | T-40 | T-60 | T-80 |

Appendix F

Surface investigation of printed suspensions

Scanning electron microscopy was used to acquire information about the surface coverage and particle distribution of the ten-layered printed squares on the paper sheets. SEM micrographs at 100x, 1000x, 5000x and 20000x magnification are given for suspensions AIP3 (T-20), AIP4 (T-20), AIP5 (T-0, T-20 and T-40), EWD1 (T-20) and EWD4 (T-20) in Tables F.1, F.2, F.3, F.4, F.5, F.6 and F.7, respectively.

Table F.1: SEM micrographs of the printed AIP3 ten-layered squares with a transparency level of 20 % (T-20) at 100x, 1000x, 5000x and 20000x magnification from top to bottom. Centered on the same spot.
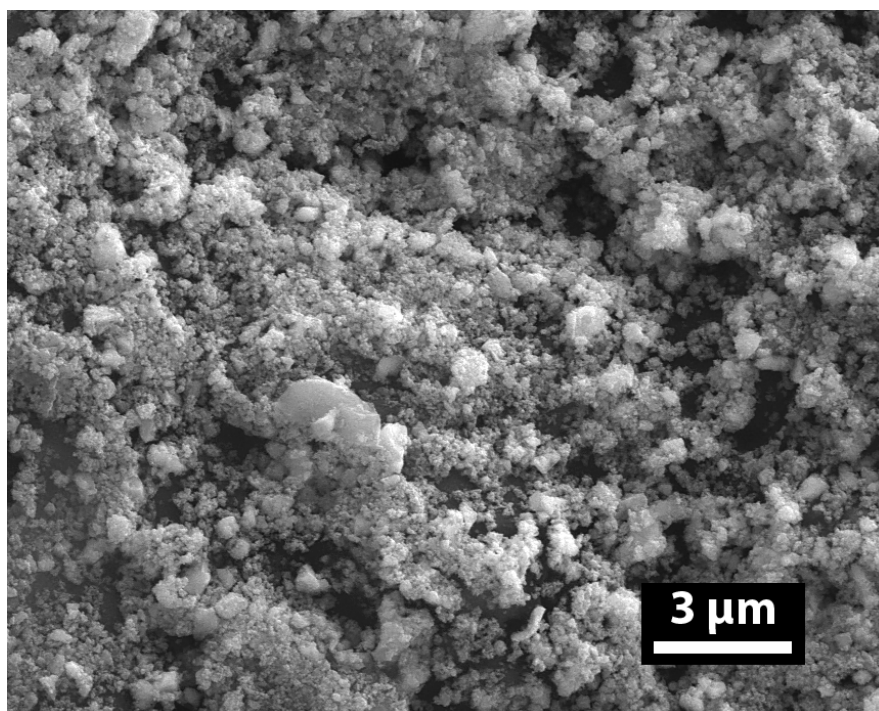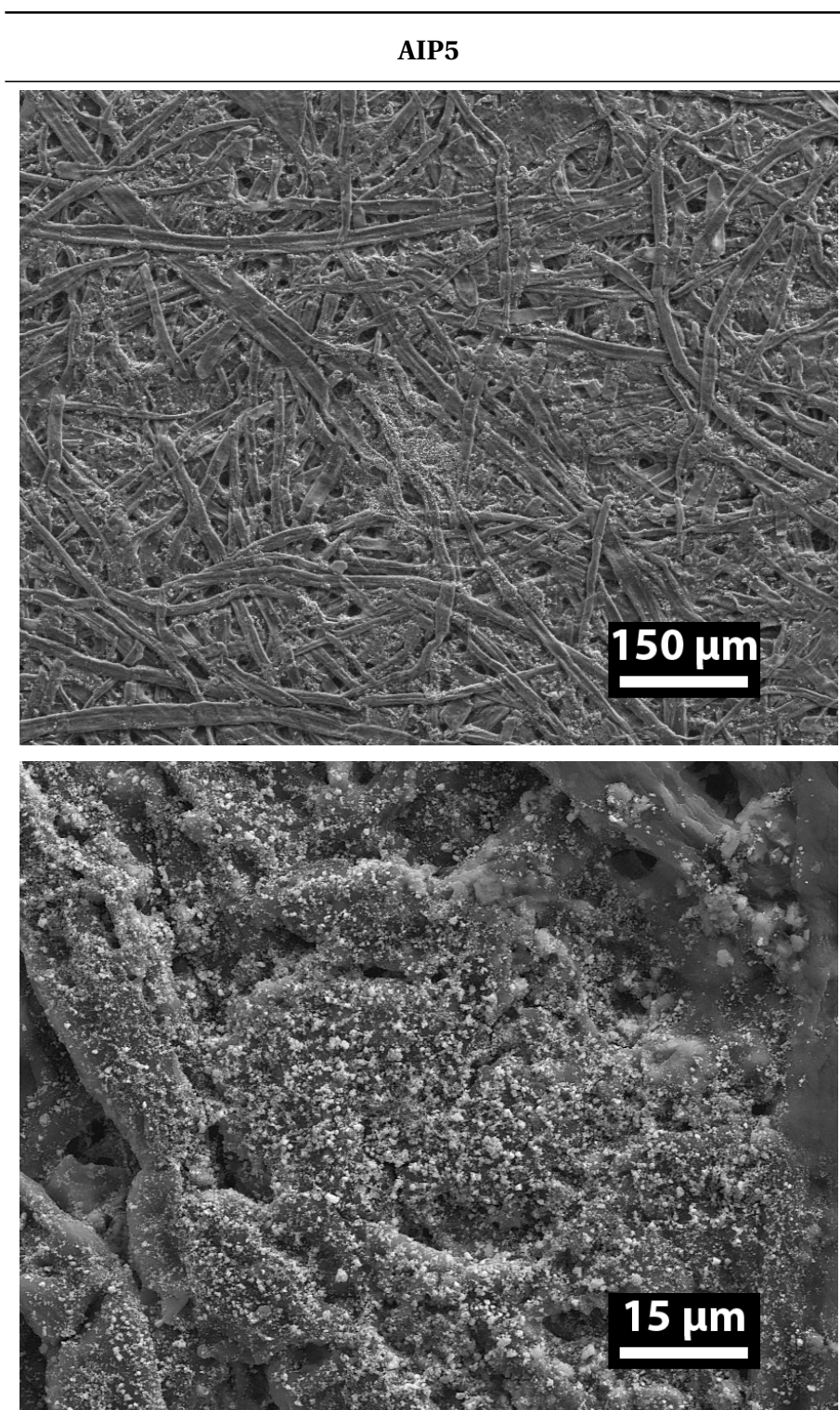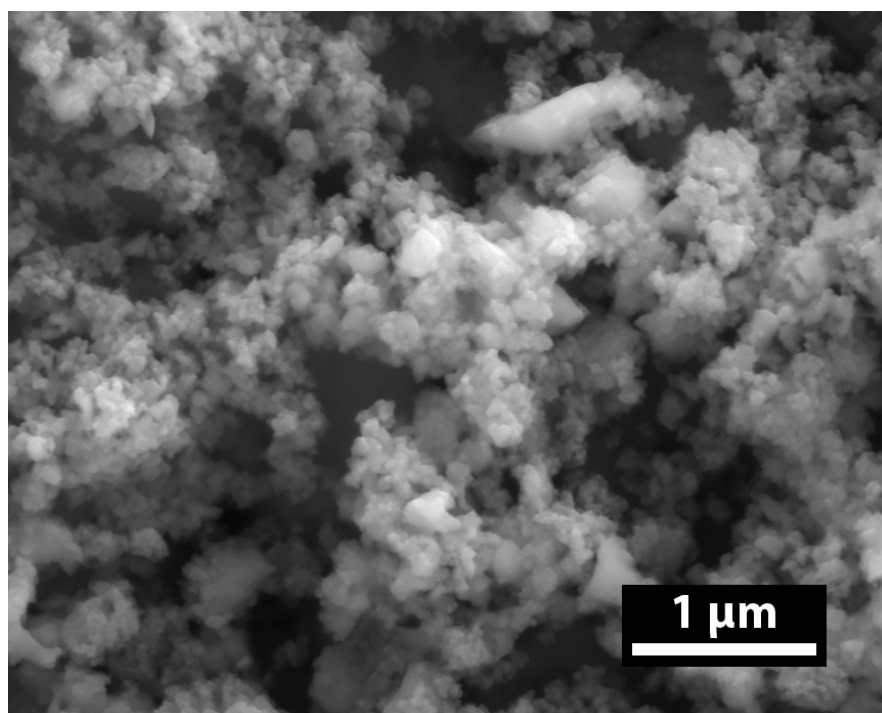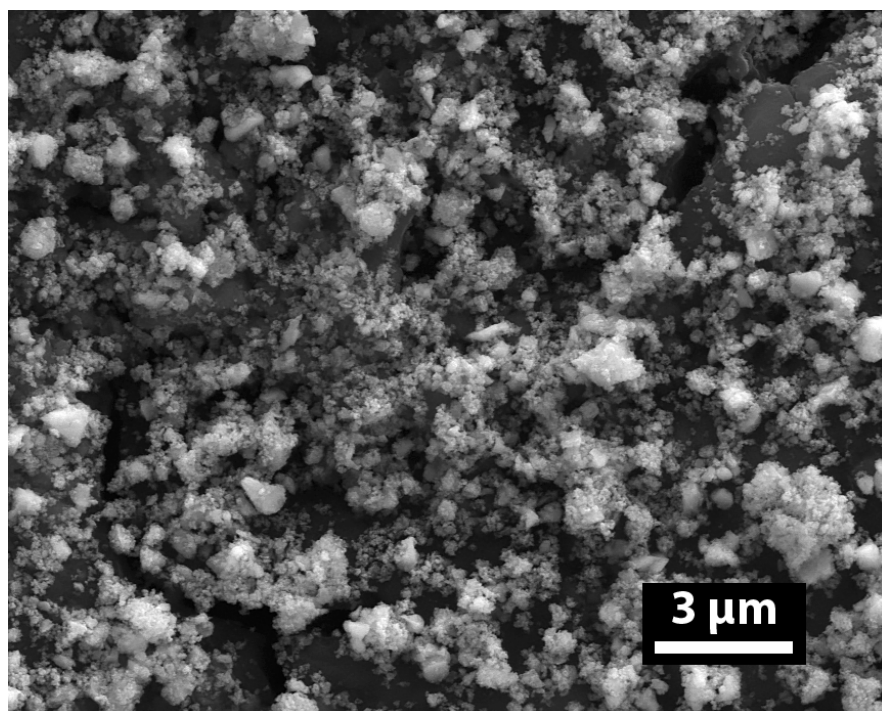
AIP3
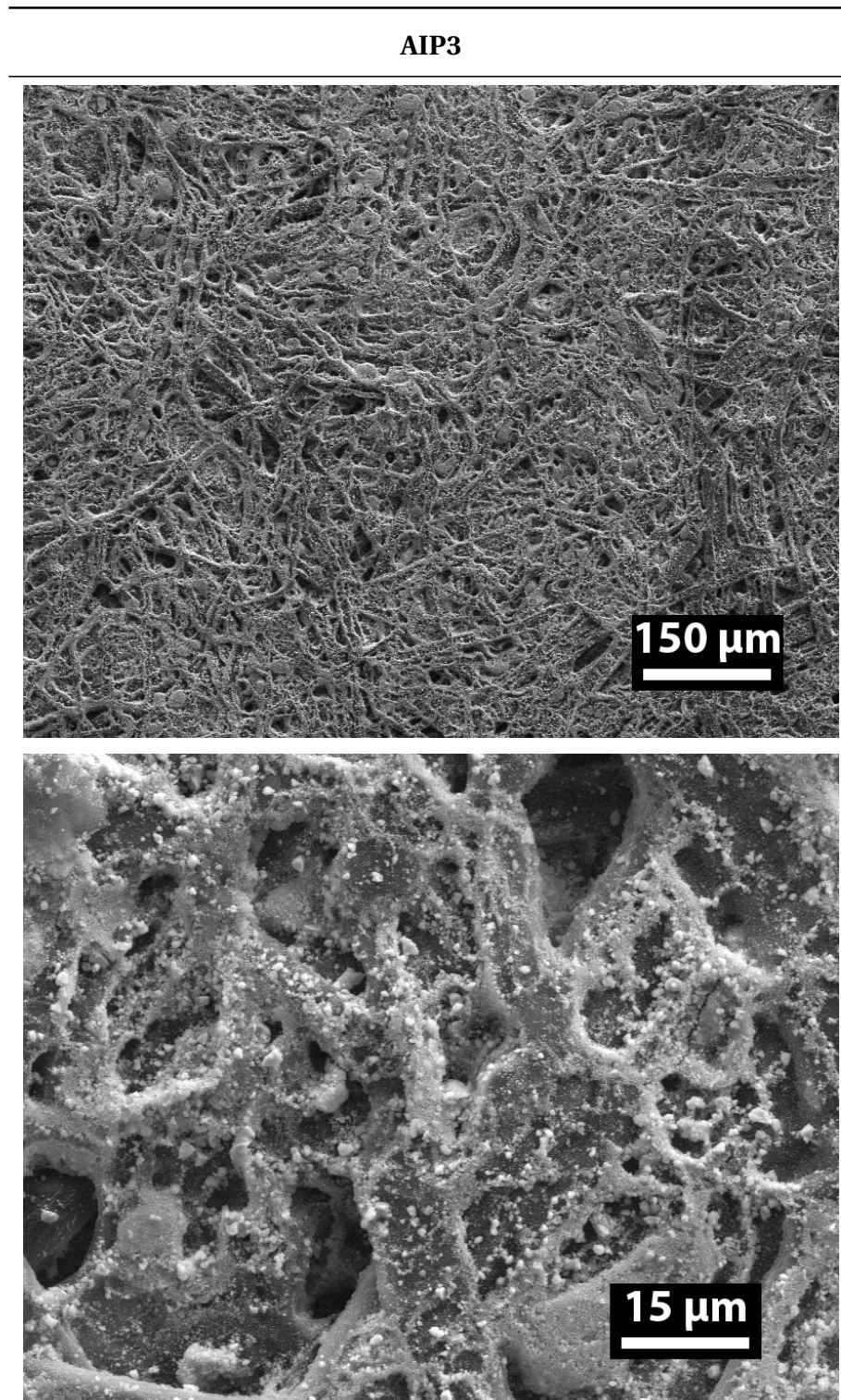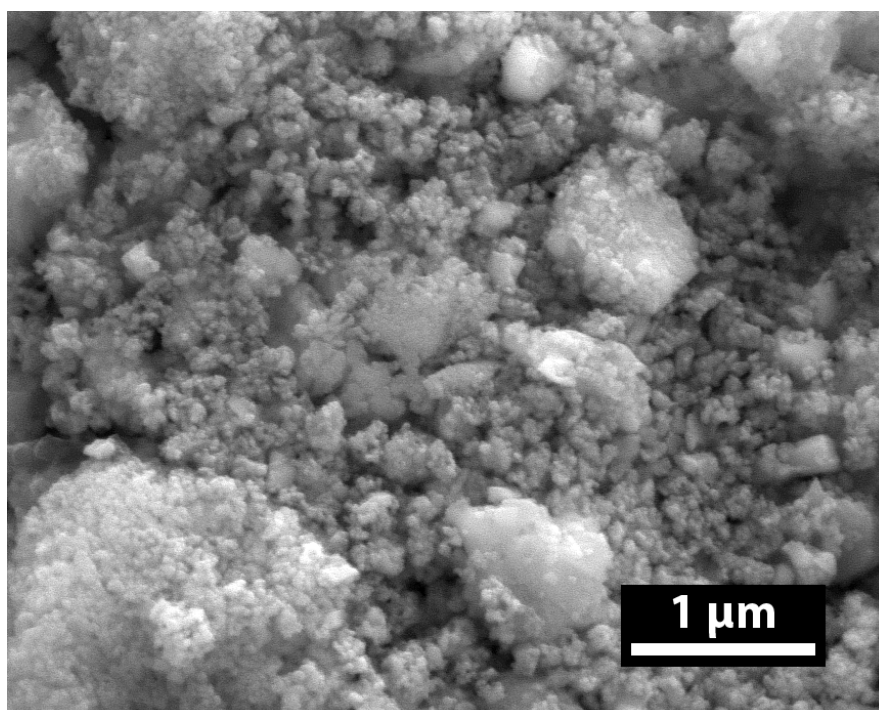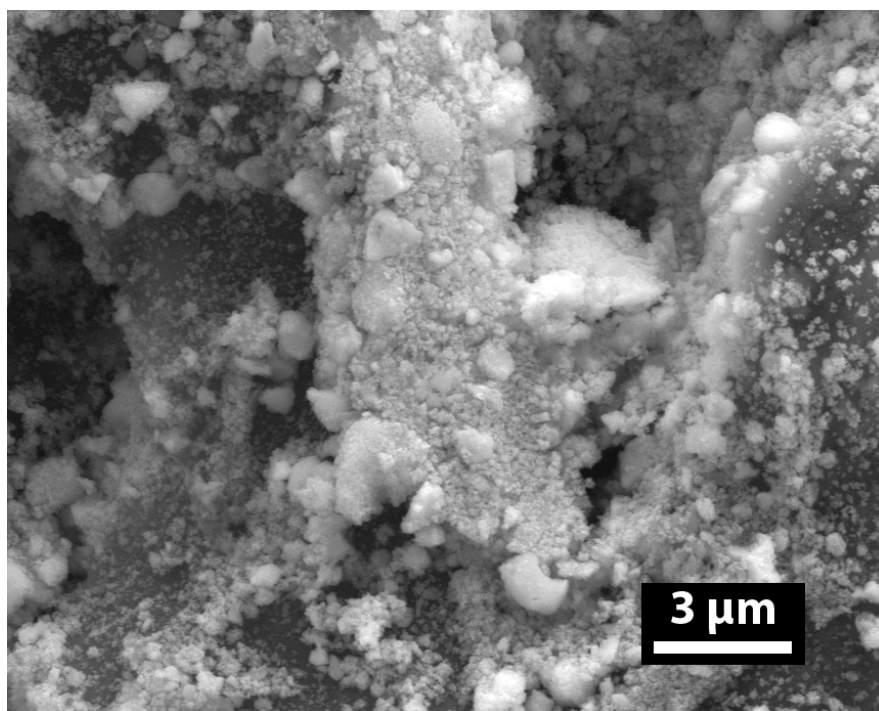
Table F.2: SEM micrographs of the printed AIP4 ten-layered squares with a transparency level of 20 % (T-20) at 100x, 1000x, 5000x and 20000x magnification from top to bottom. Centered on the same spot.

AIP4
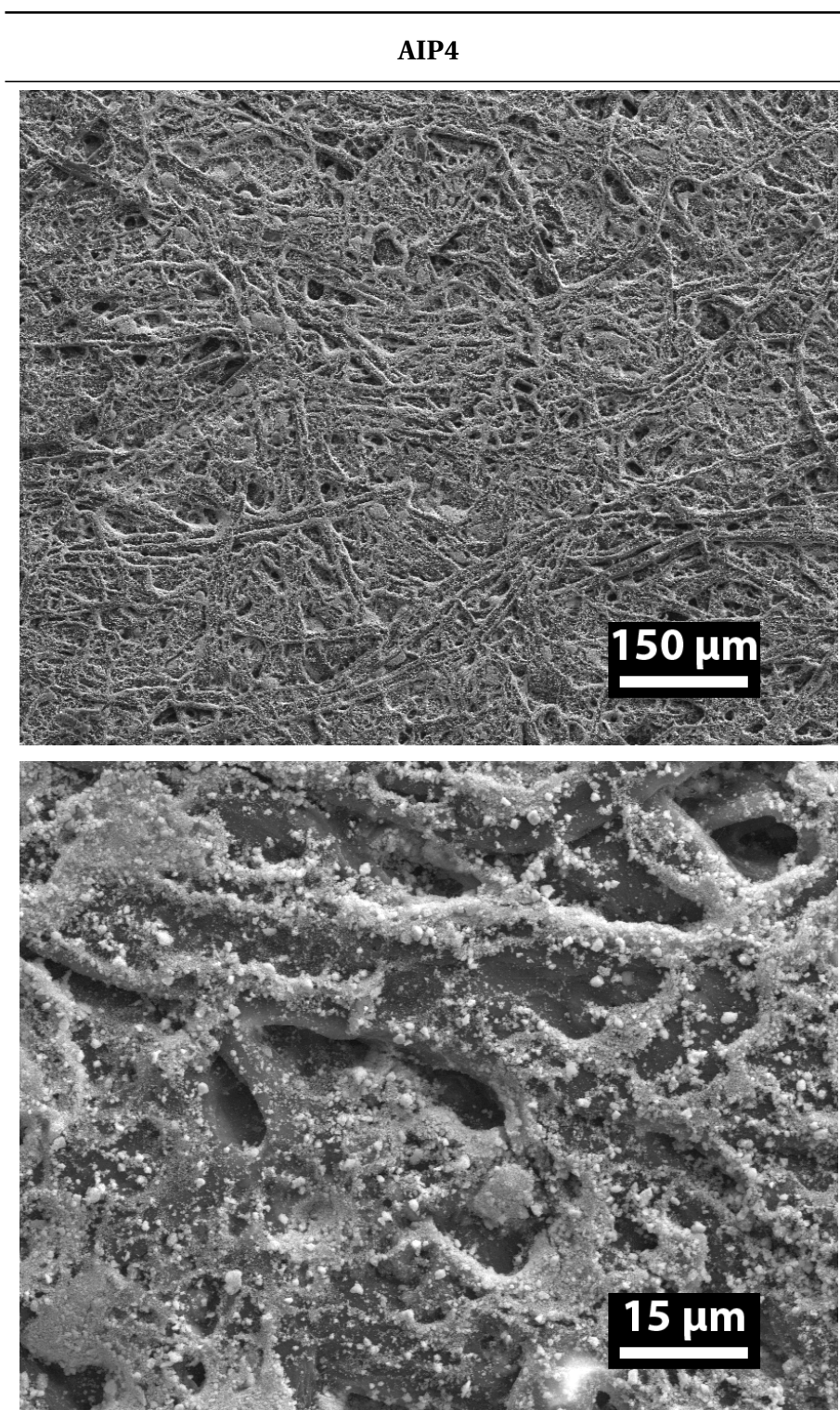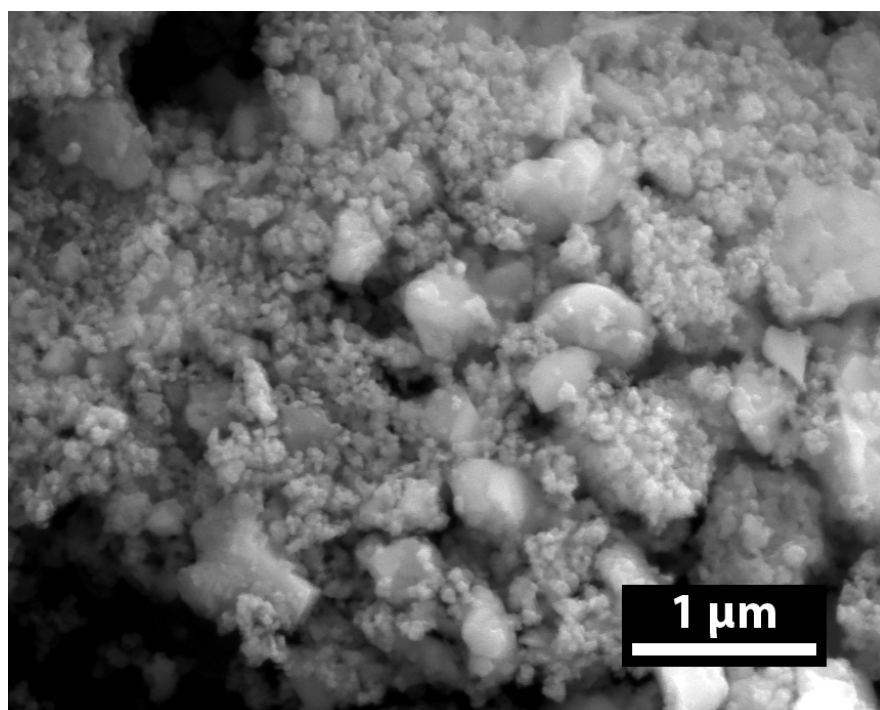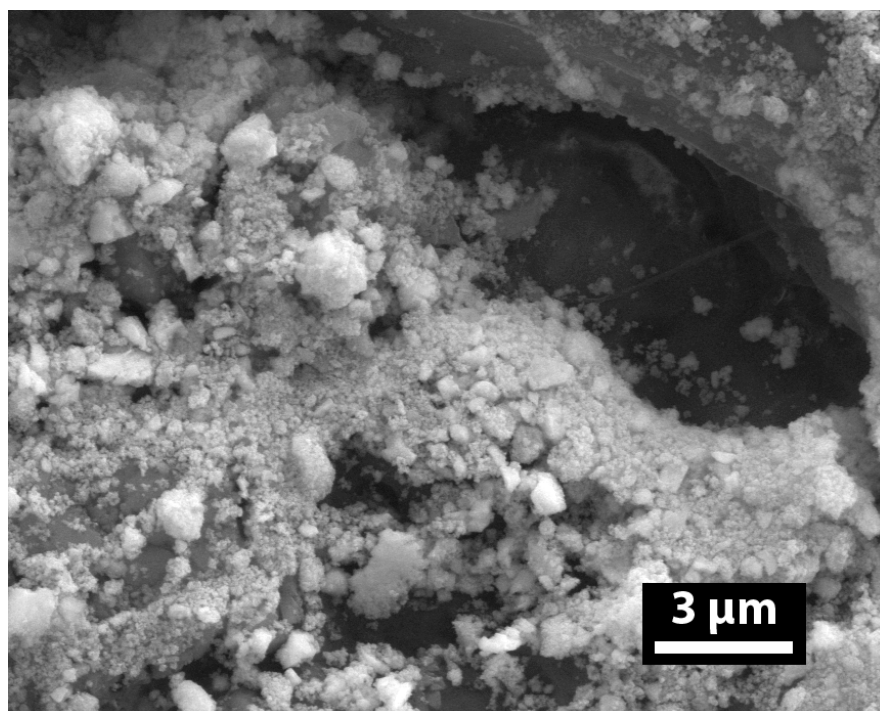
Table F.3: SEM micrographs of the printed AIP5 ten-layered squares with a transparency level of 0 % (T-0) at 100x, 1000x, 5000x and 20000x magnification from top to bottom. Centered on the same spot.
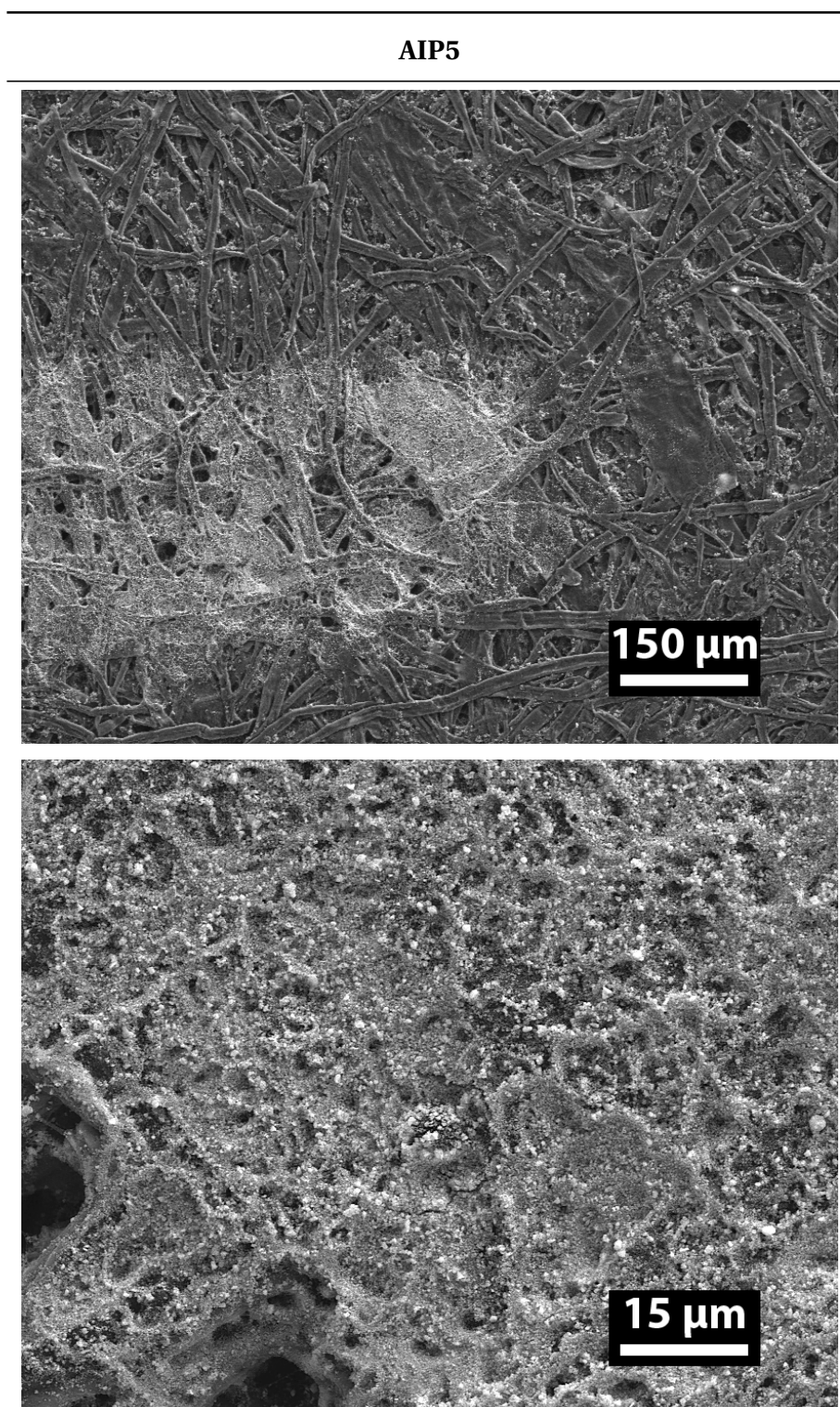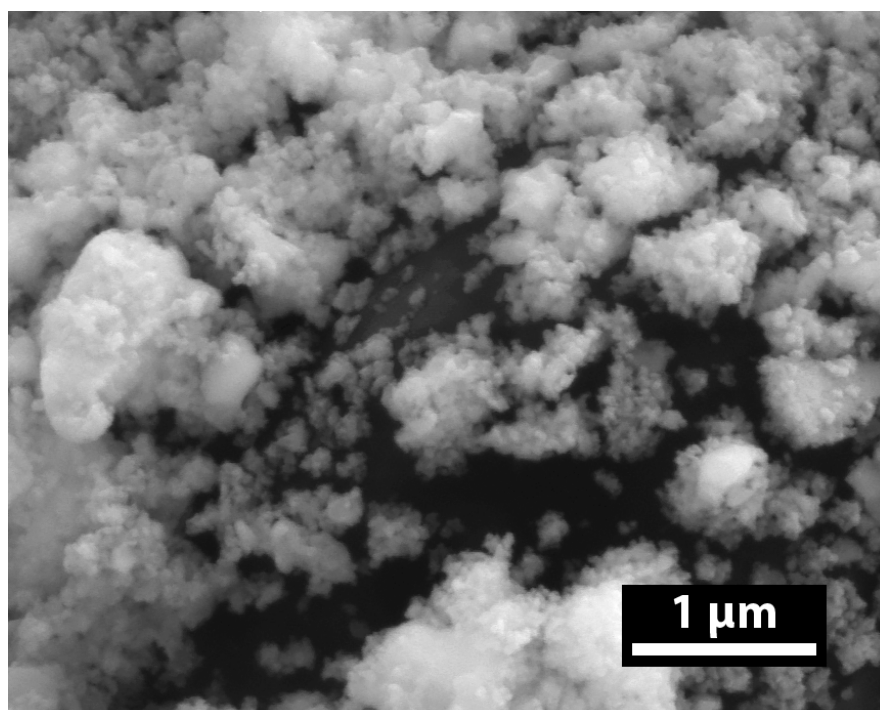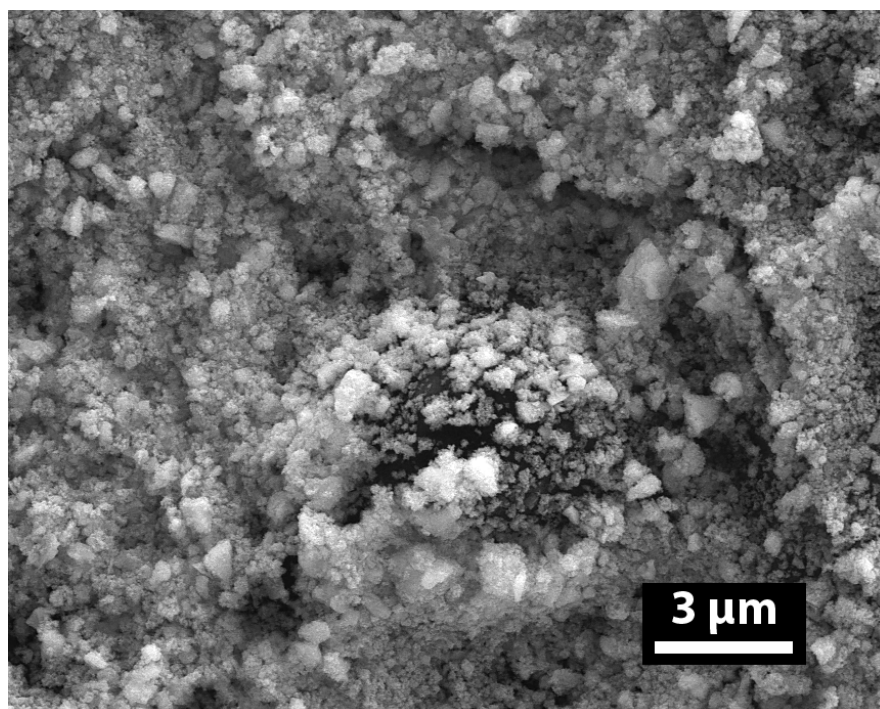
AIP5

Table F.4: SEM micrographs of the printed AIP5 ten-layered squares with a transparency level of 20 % (T-20) at 100x, 1000x, 5000x and 20000x magnification from top to bottom. Centered on the same spot.
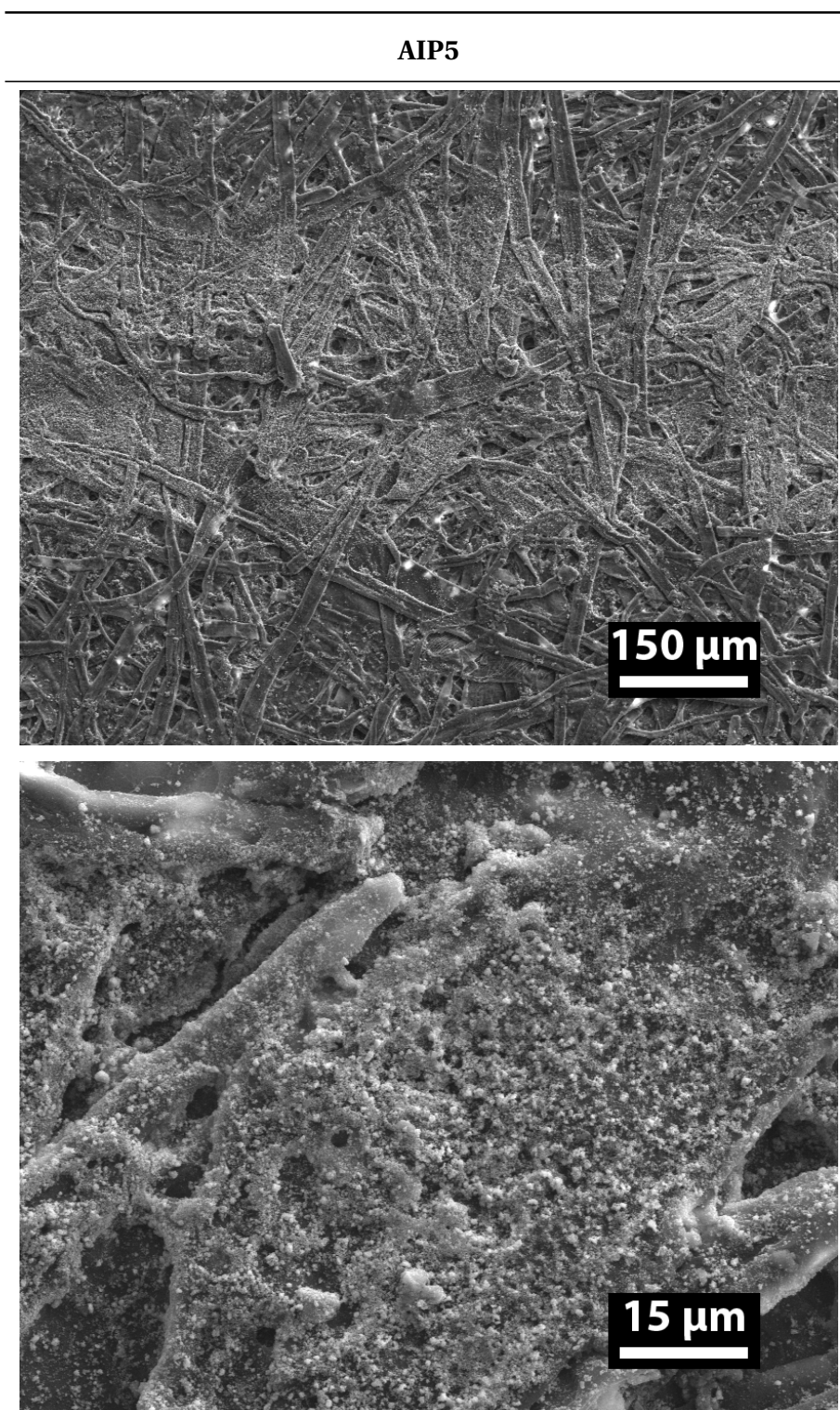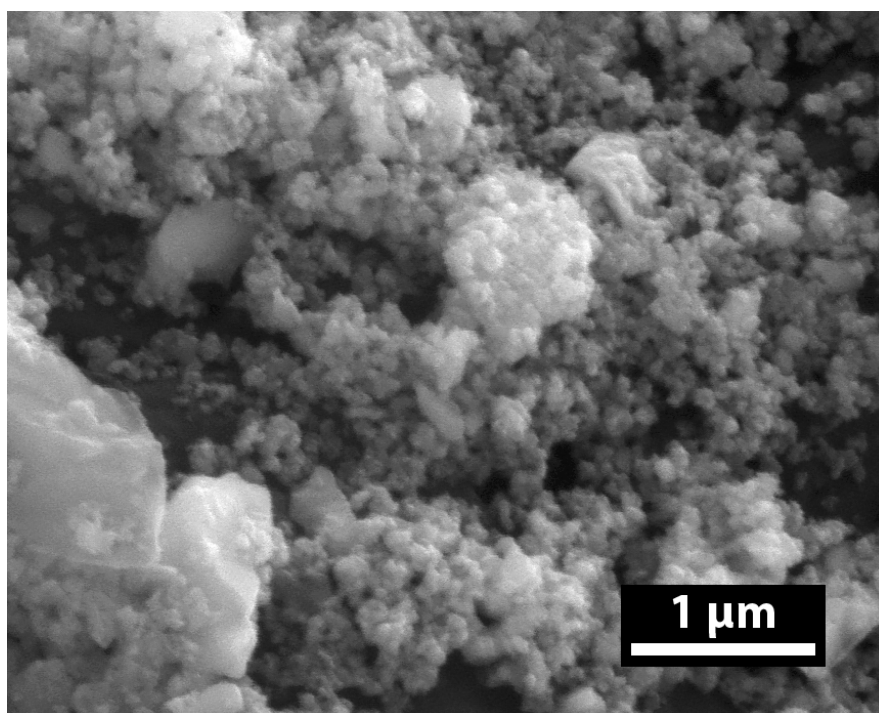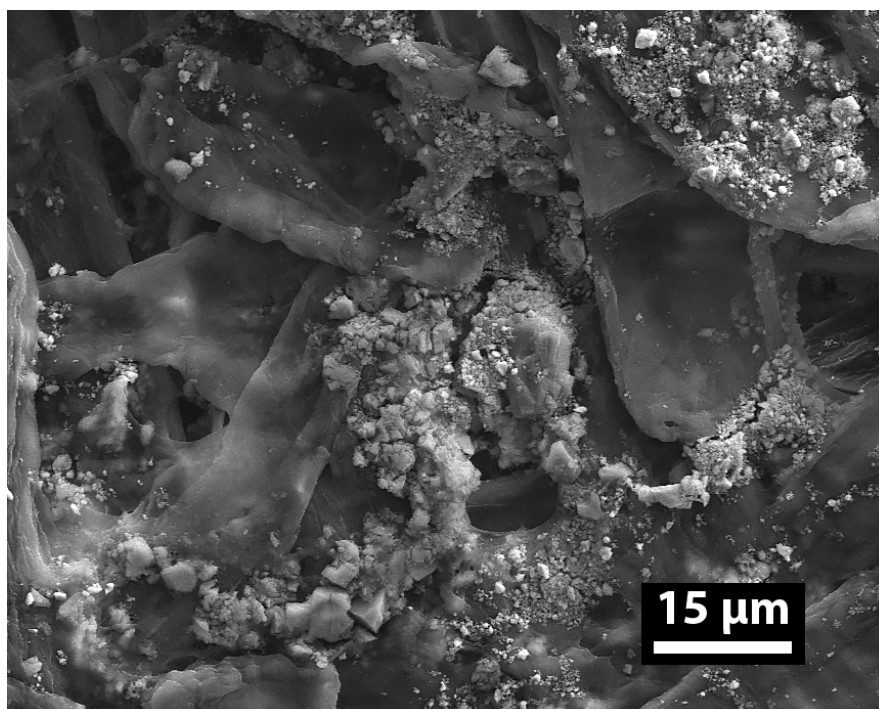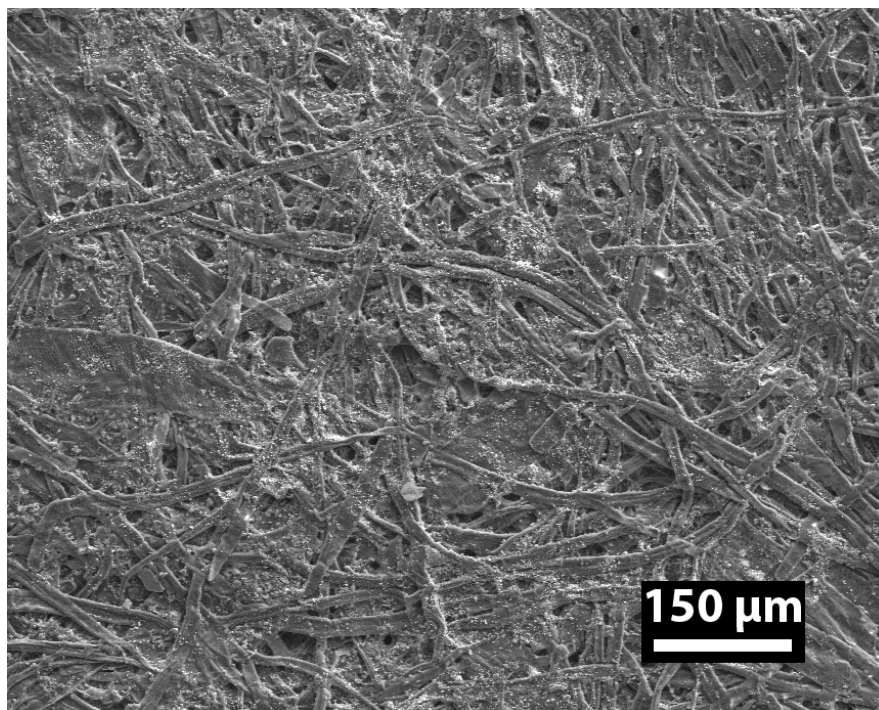
AIP5

Table F.5: SEM micrographs of the printed AIP5 ten-layered squares with a transparency level of 40 % (T-40) at 100x, 1000x, 5000x and 20000x magnification from top to bottom. Centered on the same spot.
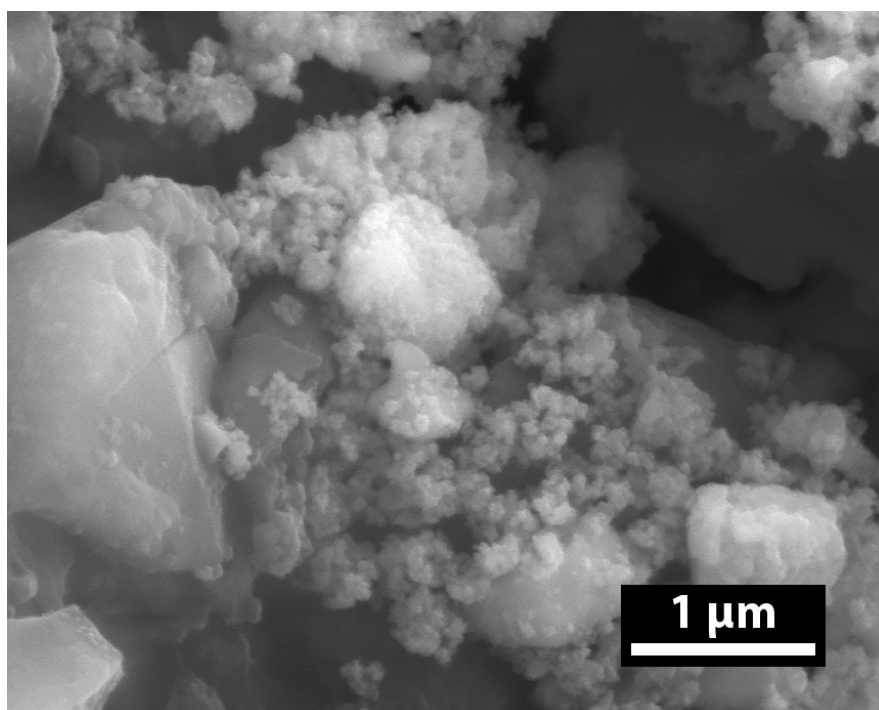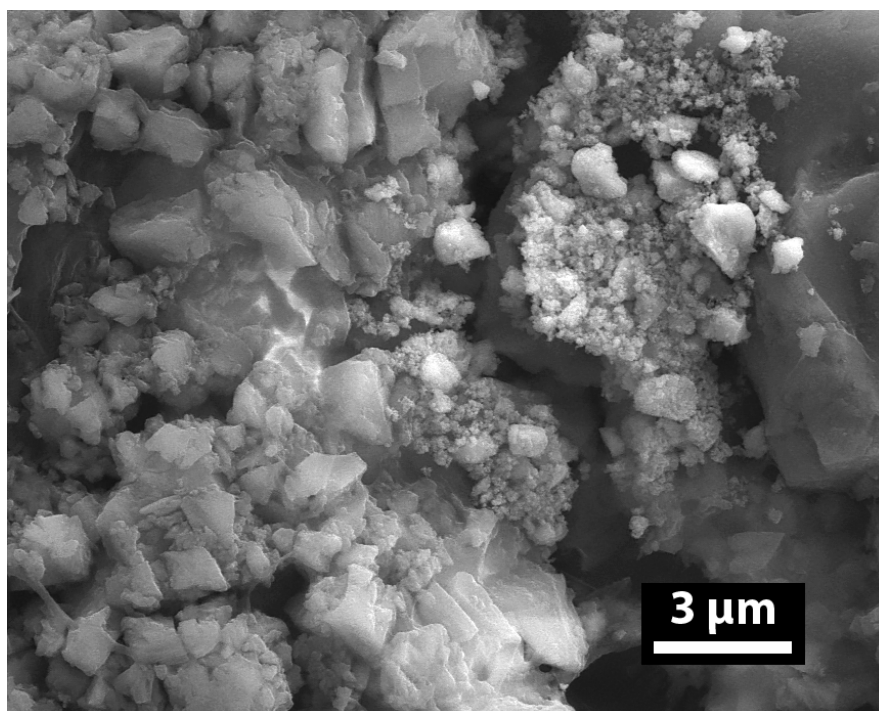
AIP5

Table F.6: SEM micrographs of the printed EWD1 ten-layered squares with a transparency level of 20 % (T-20) at 100x, 1000x, 5000x and 20000x magnification from top to bottom. Centered on the same spot.

EWD1

Table F.7: SEM micrographs of the printed EWD4 ten-layered squares with a transparency level of 20 % (T-20) at 100x, 1000x, 5000x and 20000x magnification from top to bottom. Centered on the same spot.

EWD4